List of Oral Presentations

Keynote Presentations

Regular Talks

Extended Abstracts (Keynote Presentations)

Fibres and fibrills in shear and extension: inertia vs diffusion

Fredrik Lundell

Wallenberg Wood Science Center & Linné FLOW Centre
KTH MechanicsRoyal Institute of Technology, S-100 44 Stockholm, Sweden

Keywords: fibers, fibrills, orientation

Abstract

Elongated particles in flows develop orientation distributions that are determined by, primarily, the rotation of the particles due to the velocity gradients and diffusive effects. Two experiments in which these effects are investigated will be described. The first is fibers in a turbulent wall bounded shear flow and the second is cellulose nanofibrils in a flow-focusing device. The experiments demonstrate that detailed knowledge of particle behaviour in flow, including effects of particle interactions, sedimentation, turbulence and wall interactions are necessary to understand and/or predict orientation distributions in different situations.

Introduction

The orientation of elongated particles in different flow situations is necessary to understand and predict in many engineering geophysical and biological systems. The orientation can control the rheology of the suspension, migration of particles or material properties in a final product.
The field of particle orientation in flows contains a large number of open questions and this extended abstract summarises two experiments that highlight a number of open questions.

Experimental Facilities

The first set of experimental data (Kvick 2014) is obtained at a turbulent water table flow (see figure 1). A turbulent flow of a dilute fiber suspension is created by letting the suspension flow down an inclined surface, driven by gravity. Fibers with aspect ratios 7, 14 and 28 (lengths 0.5, 1 and 2 mm) are used. The orientation distributions of the fibers in the plane of the inclined surface are obtained by image analysis of images taken from below.

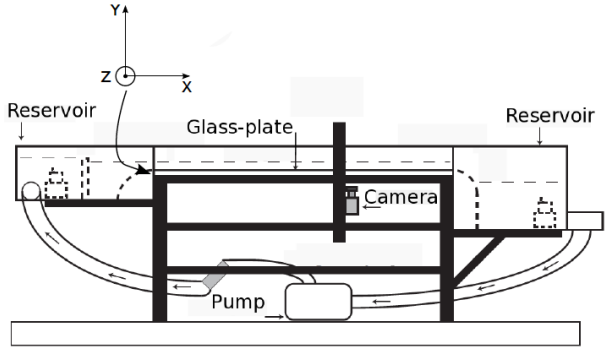

Figure 1: Sketch of the experimental setup used to study turbulent fibre suspension flow. The length of the test section is 1800 mm (Kvick 2014).

The second experiment (Håkansson et al. 2014) studies nanocellulose fibrills (width approx. 20 nm, length approx. 1 μm) in a flow focusing device (see figure 2). The orientation distribution of the fibrils at different streamwise positions is obtained by Small Angle X-ray Scattering (SAXS).

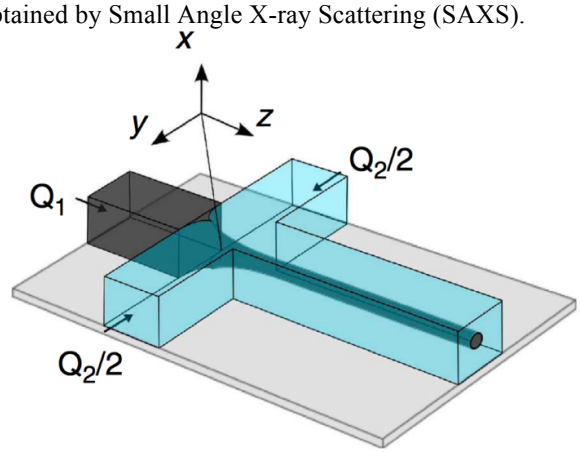

Figure 2: Sketch of the flow focusing configuration used to study nanofibril alignment. The channels are square width a width of 2mm (Håkansson et al. 2014).

Results and Discussion

Orientation distributions of the fibers in the turbulent flow for different aspect ratios and flow conditions are shown in figure 3. It is seen that the orientation distributions are distinctively different for the different aspect ratios 7, 14 and 28. Aspect ratio 7 is predominantly aligned normal to the flow direction and aspect ratio 28 is aligned in the flow direction. The effect of the turbulent length scale, on the other hand, is very small at constant aspect ratio.
The development of the order along the fibril alignment during flow focusing is shown in figure 4 by an order parameter: if the fibrils are aligned in the flow direction this parameter is 1, an isotropic orientation distribution gives the value 0 and a fibrils normal to the flow direction gives -0.5.

It is seen that the fibrils are first dealigned due to a deceleration occurring prior to the focusing. This decrease in order is followed by a strong increase thanks to the extensional flow during acceleration. After focusing, the order decreases slowly due to rotational diffusion.

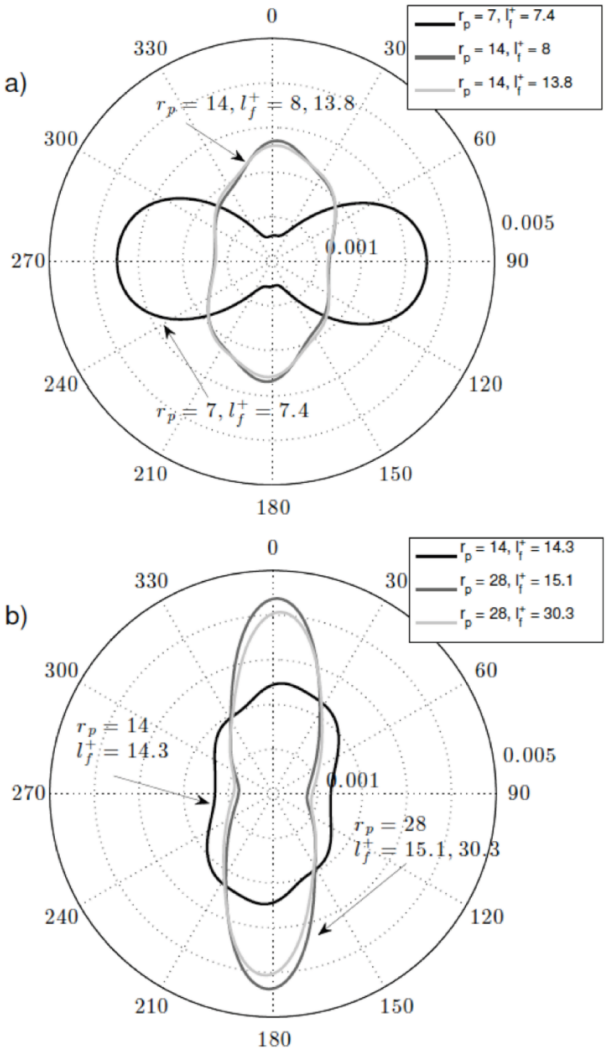

Figure 3: Polar orientation distributions for different aspect ratios and fibre lengths compared to the friction length scale. The fibers are in the streamwise direction at 0 and 180 (Kvick 2014).

Conclusions

In both experiments, it is clear that detailed knowledge of several aspects are necessary in order to understand the resulting orientation distributions. In the first, fluid and particle inertia affects the particle rotation in the shear (Rosén et al 2014a,b). Furthermore, the orientation distribution could also be affected by sedimentation and wall interactions. In order to understand the distinct behaviour: the shortest particles align normal to the flow direction and the longest particles in the flow direction, the competition between these effects must be understood.
In the second experiment, the development of the alignment is controlled by the rotational diffusion. It turns out that the rotational diffusion depends on the order: an aligned system

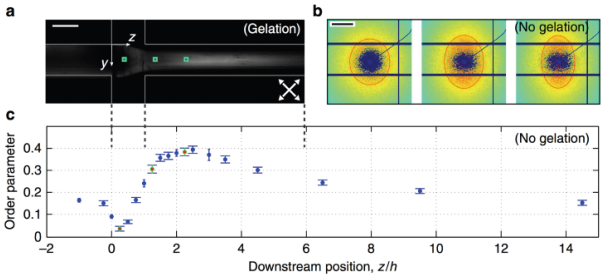

Figure 4: (a): Polarized light visualization where high intensity are more aligned fibrils. (b): SAXS-diffraction patterns. (c): Order parameter development along the flow focusing channel. From Håkansson et al. (2014).

relaxes faster towards isotropy than a less aligned system and thus, this dependence must be understood if the orientation distributions are to be predicted.

Acknowledgements

This work has been supported by Wallenberg Wood Science Center, the Swedish Research Council and the Swedish Energy Agency. I am very grateful to my previous and present PhD students Allan Carlsson, Karl Håkansson, Mathias Kvick, Afshin Abbasi-Hosseini and Tomas Rosén for everything I learnt through their work and by collaborating with them.

References

[1] Håkansson, K. M. O., Fall, A., Lundell, F., Yu, S., Krywka, C., Santoro, G., Roth, S. V., Kvick, M., Prahl-Wittberg, L., Wågberg, L., Söderberg, L. D. *Hydrodynamics alignment and assembly of nanofibrils resulting in strong cellulose filaments* Nature Comm. **5** 4018 (2014).

[2] Kvick, M. *Transitional and turbulent fibre suspension flows aimed at cellulose nanofibril processing* PhD Thesis, Royal Institute of Technology (2014).

[3] Rosén, T., Lundell, F., & Aidun, C. *Effect of fluid inertia on the dynamics and scaling of neutrally buoyant particles in shear flow* J. Fluid Mech. **738** (2014).

[4] Rosén, T., Do-Quang, M., Aidun, C. & Lundell, F *The dynamical states of a prolate spheroidal particle suspended in shear flow as a consequence of particle and fluid inertia* J. Fluid Mech. **771** (2014).

Measuring Rotation and Alignment of Anisotropic Particles in Isotropic Turbulence

Greg A. Voth

[1]*Department of Physics, Wesleyan University, Middletown, CT, USA*

Keywords: turbulence, anisotropic particles, particle laden flows, 3D printing, particle tracking

Abstract

The orientation distribution and rotations of anisotropic particles play a key role in many applications ranging from icy clouds to papermaking and drag reduction in pipe flow. Experimental access to time resolved orientations of anisotropic particles has not been easy to achieve. We have found that 3D printing technology can be used to fabricate a wide range of particle shapes with smallest dimension down to 300 μm. So far we have studied rods, crosses, jacks, tetrads, and helical shapes. We extract the particle orientations from stereoscopic video images using a method of least squares optimization in Euler angle space. We find that in turbulence the orientation and rotation rate of many particles can be understood using a simple picture of alignment of both the vorticity and a long axis of the particle with the Lagrangian stretching direction of the flow.

Introduction

Recently, we found that the 3D orientations of fibers moving through intense turbulence can be experimentally obtained using multiple high-speed cameras [1]. Extension of these methods to particles with more complex shapes represents a difficult challenge. We introduce a new way to measure the orientations and rotational dynamics of anisotropic particles that behave like ellipsoids. Many anisotropic particles rotate just like ellipsoids with an effective aspect ratio [2]. We find that particles made up of several thin rods can be designed so that they will match the rotation of any ellipsoid. These particles can be fabricated using 3D printing, and their 3D orientations can be directly measured from multiple video images [3]. Two perpendicular thin rods form a cross, while three perpendicular rods form a jack. Arguments in Bretherton [2] and resistive force theory calculations [3] show that a cross rotates like a disk, and a jack rotates like a sphere. Thus measurements of the rotations of jacks, crosses, and fibers allows access to rotations of ellipsoids across the full range of aspect ratios from disks to spheres to rods. The rotations of spheres are particularly interesting because they allow measurements of the full Lagrangian vorticity.

Nomenclature

p_i	Unit vector along the symmetry axis of a particle
$\dot{p}_i$	Tumbling rate (s^{-1})

Experimental Methods

Measurements are made in a 1m x 1m x 1.5m flow between oscillating grids that provides a reasonable approximation for homogeneous and isotropic turbulence. Four cameras image a volume of 3x3x3 cm^3 at the center of the flow that is illumined with a frequency doubled 50 W Nd-YAG laser. Particles are fabricated using a Connex 500 3D printer and are made florescent by dying them in a Rhodamine B solution. The minimum diameter of an arm that can reliably be printed is 300 microns. We chose arm lengths of 3 mm in order to have individual arms with aspect ratio of 10. In order for these particles to be small enough to resolve the small scales of the flow, we run the oscillating grid at 1 Hz which produces R_λ=91.

Results and Discussion

From the measured orientation of a particle as a function of time, we can extract the solid body rotation rate. Earlier work on rods has focused on the tumbling rate, $\dot{p}_i$, which is the part of the solid body rotation that can be measured for rods. Here, using crosses and jacks, we can measure the full solid body rotation rate, but we first extract the tumbling rate and compare with previous numerical simulations of isotropic turbulence.

The mean square tumbling rate, $\langle \dot{p}_i \dot{p}_i \rangle$ of disks and rods shows good agreement with the simulations. Both the experiments and simulations show large deviations between particle tumbling rates and the expected tumbling rates for randomly oriented particles [3]. To understand the preferential alignment of anisotropic particles in turbulence, we consider the extensional direction of the Cauchy-Green strain tensors, which gives the direction of maximal stretching of a fluid element. We find that both the long axis of particles and the fluid vorticity vector are preferentially aligned with the direction of maximal stretching [4].

Acknowledgements

This work was funded by NSF grant DMR-1208990. Guy Geyer Marcus, Shima Parsa, Stefan Kramel, Brendan Cole, Rui Ni, and Nick Ouellette contributed to the experiments.

References

[1] S. Parsa, E. Calzavarini, F. Toschi, & G.A. Voth "Rotation rate of rods in turbulent fluid flow" *Phys. Rev. Lett.*, 109, 134501 (2012).

[2] F.P. Bretherton "The motion of rigid particles in a shear flow at low Reynolds number". *J. Fluid Mech*. 14, 284–304 (1962).

[3] G.G. Marcus, S. Parsa, S. Kramel, R. Ni, and G.A. Voth, "Measurements of the solid-body rotation of anisotropic particles in 3D turbulence", *New J. Phys.*, 16, 102001 (2014).

[4] Rui Ni, Nicholas T. Ouellette and Greg A. Voth, "Alignment of vorticity and rods with Lagrangian fluid stretching in turbulence"; *J. Fluid Mech.*, 743, R3 (2014).

Dynamics and rheology of a dilute viscoelastic suspension of spheroids in an unbounded shear flow

Gaetano D'Avino[1], Francesco Greco[2], Pier Luca Maffettone[1]

[1]*Dipartimento di Ingegneria Chimica, dei Materiali e della Produzione Industriale, Universita` degli Studi di Napoli Federico II, P.le Tecchio 80, 80125 Napoli, Italy*
[2]*Istituto di Ricerche sulla Combustione, Consiglio Nazionale delle Ricerche, P.le Tecchio 80, 80125 Napoli, Italy*

Keywords: shear flow, viscoelastic suspension, spheroid dynamics

Abstract

The dynamics and rheology of a dilute viscoelastic suspension of nonBrownian spheroids in an inertialess unbounded shear flow is addressed through numerical simulations. The motion of an isolated ellipsoid shows a complex dynamics depending on the Deborah number De (De is the product of the viscoelastic liquid intrinsic time times the applied shear rate). Spiraling orbits toward a log-rolling motion around the vorticity are observed for low Deborah numbers, whereas the particle aligns with its major axis near to the flow direction at high Deborah numbers. At intermediate De-values periodic regimes are found with small amplitude oscillations around orientations progressively shifting from vorticity to flow direction by increasing De. A bistability region with periodic solutions coexisting with flow aligned regimes is also detected, confirming experimental evidence. The dynamics results are complemented with the rheological predictions in dilute conditions. Average stresses are computed as suggested by Batchelor. The presence of the ellipsoidal particles alters the rheology of the suspending liquid in a complex fashion that depends on the De-values.

Introduction

The motion of nonspherical particles suspended in fluids is of great relevance in industrial applications and biological systems. In this work we treat the inertialess problem and consider particles large enough to be considered nonBrownian objects.
For the case of unconfined shear flow, Jeffery (1922) predicted the dynamics of a single, rigid, non-Brownian ellipsoidal particle in a Newtonian fluid. The orbits described by the particle orientation vector (the so-called Jeffery's orbits) are closed periodic curves around the vorticity axis. Experimental results confirmed those predictions (e.g., Anczurowski and Mason, 1968).
In several industrial and biological applications such as fiber-reinforced polymer processing, spermatozoa swimming in viscoelastic cervical mucus, the particles are immersed in a nonNewtonian viscoelastic liquid. The rheological complexity of the suspending liquid strongly alters the particle dynamics with respect to that observed for a Newtonian fluid in analogous flow conditions. Experiments, indeed, have evidenced that an elongated particle in a sheared viscoelastic liquid at small shear rates drifts across the Jeffery's orbits, and its major axis eventually aligns along the vorticity direction, the so-called log-rolling motion (Iso et al. 1996). At large shear rates, instead, flow alignment is found (Johnson et al, 1990), with the ellipsoid major axis oriented along the velocity direction. A recent experimental work (Gunes et al, 2008) clearly showed the transition from vorticity to flow alignment for increasing shear rates. In a range of intermediate shear rates, however, bimodal orientational distributions were reported, although the achievement of a true steady state could not be confirmed. The two coexisting preferred orientations are either close to vorticity or close to flow direction.
From the theoretical point of view, an asymptotic theory (Leal, 1975) in the limiting case of an infinitely elongated particle immersed in a specific "second-order fluid" captures the spiraling motion toward the vorticity axis at small shear rates along with the alignment to the flow direction at higher shear rates.
In the limit of dilute suspensions, the rheological characterizarion of the suspension as a whole can be determined by computing the bulk stress as suggested by Batchelor (1970).
In this work, the dynamics of an ellipsoidal particle in a sheared, unconfined viscoelastic fluid and the corresponding rheological response of a dilute suspensions are addressed by numerical simulations. We calculate the stress tensor by considering the regime solutions of a single ellipsoid dynamics and using the corresponding velocity and pressure fields.

Mathematical model

A single spheroidal particle is located between two parallel plates moving at equal but opposite velocities (simple shear flow). We denote with a and b the semimajor and semiminor spheroid axes, and with AR = a/b the aspect ratio. The distance between the two plates is much larger than a so as to represent an unconfined system. We denote by **p** the orientation pseudovector that identifies the direction of the particle major axis.
Direct numerical simulations are performed by solving the mass and momentum balance equations together with a constitutive model taking into account the suspending fluid

viscoelasticity. The Giesekus constitutive equation is chosen to model the viscoelastic liquid. The particle motion is managed by using an ALE formulation (Arbitrary Lagrangian-Eulerian) (Hu et al., 2001), whereby at each time step the mesh grid is rigidly rotate following the particle orientation. Finally, the particle orientation is updated by using quaternions. More details about the equations and the numerical method can be found elsewhere (D'Avino et al., 2014).

Once the velocity, pressure and stress fields are computed, the bulk stress is calculated as the sum of a fluid and a particle contribution (Batchelor, 1970):

$$<\boldsymbol{\sigma}>=<\boldsymbol{\sigma}>_f+<\boldsymbol{\sigma}>_p=\frac{1}{V}\int_{V_f}\boldsymbol{\sigma}\,\mathrm{d}V+\frac{1}{V}\int_{S_p}(\boldsymbol{\sigma}\cdot\mathbf{n})\,\mathbf{r}\,\mathrm{d}S \quad (1)$$

where $\boldsymbol{\sigma}$ is the total stress tensor, $\mathbf{n}$ is the normal vector to the particle surface, $\mathbf{r}$ is the position vector of a point on the particle surface, V is the volume of the suspension, V_f is the volume occupied by the fluid and S_p is the particle surface. For a dilute suspension, the last term can be rewritten as (Housiadas & Tanner, 2009):

$$<\boldsymbol{\sigma}>_p=\phi\frac{1}{V_p}\int_{S_p}(\boldsymbol{\sigma}\cdot\mathbf{n})\,\mathbf{r}\,\mathrm{d}S=\phi\,\boldsymbol{\sigma}_p \quad (2)$$

where ϕ is the volume fraction.

Finally, we define the Deborah number as $\mathrm{De}=\lambda\,\dot{\gamma}$ where λ is the fluid relaxation time and $\dot{\gamma}$ is the applied shear rate.

Results and Discussion

Spheroid dynamics

We proceed by illustrating as an example the dynamics of an ellipsoid with aspect ratio AR = 4. For De = 1 the stable regime is the so-called log-rolling motion with the ellipsoid rotating around its axis of revolution that coincides with the vorticity direction. Such a regime is attained for whatever initial condition of the ellipsoid, out of the shearing plane. When the initial orientation lies within the shear plane, instead, the ellipsoid forever tumbles around the vorticity axis, with its major axis always in the shear plane, this situation is, however, unstable, as any perturbation driving the major axis out of the shearing plane determines its subsequent spiralling towards the vorticity axis. At high De-values (>2.7) the ellipsoid eventually attains a steady-state regime, with its major axis aligned within the shear plane, and very close to the flow direction. Such a final regime is found for any initial condition, including those with the initial orientation out of the shearing plane. These results correctly capture the experimentally observed transition from vorticity to flow alignment moving from low to high Deborah numbers.

At intermediate De range numbers, between 2 and 2.6, the asymptotic solution is a periodic oscillation with average orientation close to the vorticity direction. For 2.6<De<2.7 a bistability situation is predicted with the coexistence of a flow aligning steady state solution and a periodic solution with average orientation closer to the shearing plane.

A schematic of the solution diagram is reported in Fig. 1. The bistability region favourably compares with the experimental results of Gunes et al (2008).

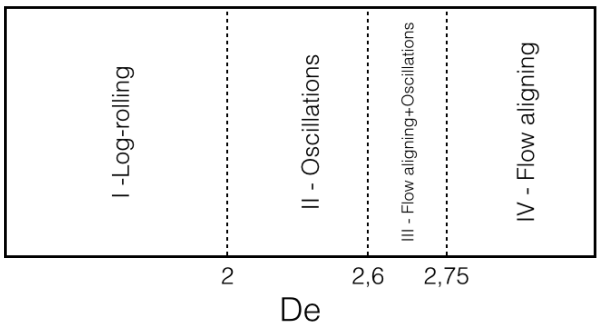

Fig. 1: The regime solutions at with De as a bifurcating parameter for ellipsoid with AR=4.

A similar scenario as that reported in Fig. 1 was also found for spheroids with larger aspect ratios.

Dilute suspension rheology

Let us now discuss the particle contribution to the bulk stress given in Eq. (2). Specifically, we show the contributions to the viscosity and to the first normal stress difference due to the presence of a spheroid, i.e.:

$$B_\eta=\frac{\sigma_{p,xy}}{\eta_0\dot{\gamma}} \quad (3)$$

$$B_{N1}=\frac{\sigma_{p,xx}-\sigma_{p,yy}}{N_{10}} \quad (4)$$

Notice that, Eq. (3) for a Newtonian suspending fluid (De = 0) corresponds to the coefficient B predicted by Jeffery (Jeffery, 1922; Mueller et al., 2010). This coefficient is equal to 2.5 for a spherical particle (AR = 1).

All the data reported in this section are taken after the spheroid has reached the final orientation, i.e. the transients due to the viscoelastic stress build-up (fast) as well as the transients due to the orientational changes of the particle (slow) are neglected. The data in region II (small-amplitude oscillatory orientation) are computed by averaging the (periodic) bulk stress trends over the period. Finally, concerning the data in region III (bistability), we assume an initial isotropic orientational distribution. We first detect the separatrix that divides the unit spherical surface in two areas corresponding to initial orientations that lead the spheroid towards the intermediate orientation and the alignment along the flow direction. Then, the particle viscosity contributions corresponding to the two regimes are weighted by these two areas.

Figure 2 shows the particle viscosity contribution B_η as a function of the Deborah number for a sphere (black symbols/lines) and a spheroid with AR = 4 (blue symbols/lines). At De = 0, the two data quantitatively agree with the Einstein/Jeffery predictions (the deviations from the theoretical values are lower than 1%). For increasing De-values, the particle viscosity contribution for a sphere monotonically decreases due to the shear-thinning of the suspending fluid. For any Deborah number, however, such a contribution is positive thus the suspension bulk viscosity is always higher than the viscosity of the suspending medium.

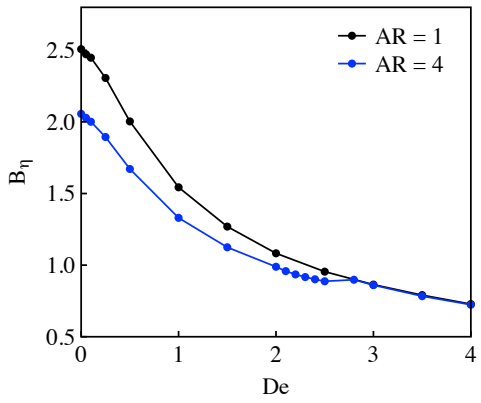

Figure 2: Particle viscosity contribution B_η for a sphere (black symbols/lines) and a spheroid with aspect ratio AR = 4 (blue symbols/lines) as a function of the Deborah number.

For a spheroid with AR = 4, B_η monotonically decreases similarly to the sphere case in the region I (vorticity alignment). Such a trend is also observed in region II when the particle gradually changes the orientation from the vorticity to the flow direction. On the other hand, a small increasing trend is observed in the bistability region (region III). By further increasing the Deborah number in region IV (flow alignment), the B_η-coefficient starts to decrease again. However, the jump due to the transition between region II and IV is quantitatively very small. Hence, we can conclude that the orientation of a spheroid with AR=4 has only a weak influence on the trend of the particle contribution to the bulk viscosity.

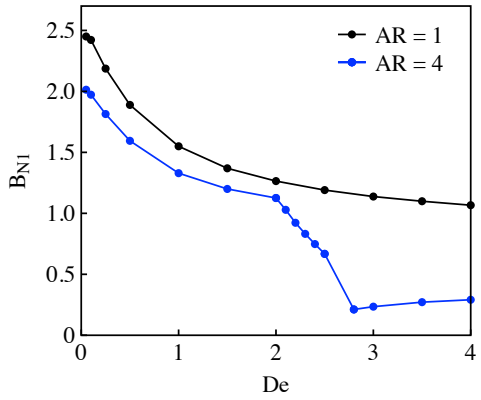

Figure 3: Particle first normal stress difference contribution B_{N1} for a sphere (black symbols/lines) and a spheroid with aspect ratio AR = 4 (blue symbols/lines) as a function of the Deborah number.

Figure 3 shows the contribution of the particle to the bulk first normal stress difference B_{N1} as a function of the Deborah number for a sphere (black symbols/lines) and a spheroid with AR = 4 (blue symbols/lines). Both curves start from a non-zero Deborah number since there is no contribution to N_1 in a Newtonian fluid (N_{10} = 0). A monotonically decreasing trend is observed for a sphere as the Deborah number increases. For a spheroid, the simulation data show that the trend of B_{N1} strongly depends on the particle orientation. Indeed, as the particle is oriented along the vorticity, the trend is similar to the spherical particle case. On the other hand, as soon as the spheroid starts to change orientation moving from the vorticity towards the flow direction, the slope of the trend increases and the blue data deviate from the black ones (see the data for De between 2 and 2.5). Finally, a significant reduction of the coefficient is observed when the particle aligns along the flow. In region IV, indeed, B_{N1} is 4-5 times lower than the corresponding value for a sphere. For increasing De-values in region IV, a monotonically increasing trend is observed.

As a final remark, we signal that a similar effect of the particle orientation shown in Figure 3 is also observed for the particle contribution to the second normal stress difference N_2.

Conclusions

The simulation results reveal a complex dynamics with different regimes as the Deborah number is increased. For low Deborah numbers a drift through the Jeffery's orbits is found with the ellipsoid major axis following a spiraling motion towards the vorticity. As the Deborah number is increased, the equilibrium orientation gradually moves from the vorticity to the flow direction, and, beyond a critical Deborah number, such a solution co-exists with alignment near the flow direction. The latter becomes the only stable solution for high Deborah number values. The present results favorably compare with experimental data available in the literature.

Following the Batchelor approach we also determined the rheology of a dilute suspensions of spheroids under shearing flows. The predicted features show a slight variation from dilute suspensions of rigid spheres at low De-values, with a substantial contribution to the viscosity and first normal stress difference due to the particles. On the contrary, in the flow aligning regime at high De-values, the particle contribution to the viscosity is less important and nearly equals that of spheres, while a steep decrease is predicted for the first normal stress difference far below that predicted for spheres.

Acknowledgements

The research leading to these results has been supported by the RoDyMan project, which has received funding from the European Research Council (FP7 IDEAS) under Advanced Grant agreement number 320992.

References

Anczurowski E. and Mason S. G., Trans. Soc. Rheol. 12, 209 (1968).

Batchelor, G.K. The stress system in a suspension of force-free-particles. J. Fluid Mech., Vol. 41, 545-570 (1970)

D'Avino, G., Hulsen, M.A., Greco, F. & Maffettone, P.L. Bistability and metabistability scenario in the dynamics of an ellipsoidal particle in a sheared viscoelastic fluid, Phys. Rev. E, Vol. 89, 043006 (2014)

Housiadas, K.D. & Tanner, R.I., On the rheology of a dilute suspension of rigid spheres in a weakly viscoelastic matrix fluid, J. non-Newtonian Fluid Mech., Vol. 162, 88-92 (2009)

Gunes D. Z., Scirocco R., Mewis J., and Vermant J., J. Non-Newtonian Fluid Mech. 155, 39 (2008).

Hu, H.H., Patankar, N.A. & Zhu, M.Y., Direct Numerical Simulations of fluid–solid systems using the Arbitrary Lagrangian–Eulerian technique. J. Comp. Phys. Vol. 169, 427-462 (2001)

Iso Y., Koch D. L., and Cohen C., J. Non-Newtonian Fluid Mech. 62, 115 (1996).

Jeffery, G.B. The motion of ellipsoidal particles immersed in a viscous fluid. Proc. R. Soc. Lond. A, Vol. 102, 161-179 (1922)

Johnson S. J., Salem A. J., and Fuller G. G., J. Non-Newtonian Fluid Mech. 34, 89 (1990).

Leal L. G., J. Fluid Mech. 69, 305 (1975).

Mueller, S., Llewellin E.W. & Mader, H.M. The rheology of suspensions of solid particles. Proc. Royal Soc. A, Vol. 466, 1201-1228 (2010)

Effect of particle and fluid inertia on Jeffery orbits

J. Einarsson[1], F. Candelier[2], F. Lundell[3], J. R. Angillela[4], B. Mehlig[1]

[1]*Department of Physics, Gothenburg University, Gothenburg, Sweden*
[2]*Univeristy of Aix-Marseille, Marseille, France*
[3]*KTH Royal Institute of Technology, Stockholm, Sweden*
[4]*Department of Mathematics and Mechanics, University of Caen, Caen, France*

Keywords: spheroidal particles, simple shear, Jeffery orbits, inertia, reciprocal theorem

Abstract

Tumbling of small axisymmetric particles in a steady shear flow is a problem of fundamental importance. When inertial effects are negligible the problem is degenerate. It exhibits infinitely many periodic solutions, the so-called `Jeffery orbits'. In Einarsson *et al.* (2015a) we perturbatively solved the coupled particle-flow equations and showed how the degeneracy is lifted by weak inertial effects. This extended abstract describes the method and the main results of this work. In the slender-body limit our results are consistent with those by Subramanian & Koch (2005). In Einarsson *et al.* (2015a) we derived an equation of motion valid for neutrally buoyant spheroidal particles with arbitrary aspect ratios at small shear Reynolds numbers. This equation shows that tumbling in the shear plane is stable for prolate spheroids for small shear Reynolds numbers. All other Jeffery orbits are unstable for prolate spheroids, also the `log-rolling' orbit. For oblate nearly spherical particles we find that the stabilities are reversed. Both unsteady and non-linear terms in the Navier-Stokes equation turn out to be important.

Introduction

The orientational dynamics of particles in fluids is of interest in a wide range of scientific problems. An example of great significance is the dynamics of a small neutrally buoyant axisymmetric particle in a steady shear flow. The particle tumbles periodically: it aligns with the flow direction for a long time and then rapidly changes orientation by 180 degrees. There are infinitely many marginally stable periodic orbits, the `Jeffery orbits' (Jeffery 1922). This means that small perturbations can have large effects, and it is therefore necessary to consider the consequence of perturbations that are not part of Jeffery's theory.

In Einarsson *et al.* (2015a) we computed the effect of weak particle and fluid inertia upon the tumbling of a neutrally buoyant spheroidal particle in a simple shear flow. Details of the calculation are given in (Einarsson *et al.* 2015b) and Candelier *et al.* (2015). In the following we briefly summarise the main result.

In these articles we derived an effective equation of motion for the orientation of the spheroidal particle when inertial effects are weak but nevertheless important (at small shear Reynolds numbers Re_s). Linear stability analysis of this equation at infinitesimal Re_s shows how the degeneracy of the Jeffery orbits is lifted by inertial effects. We find that tumbling in the shear plane is stable for prolate spheroids. Log-rolling is unstable for prolate spheroids. In the slender-body limit this result is consistent with those of

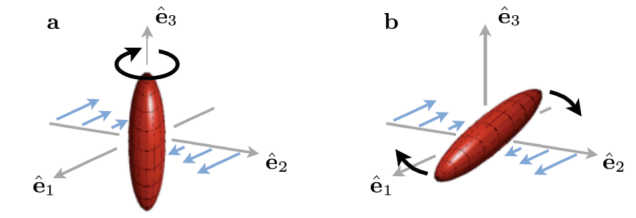

Figure 1: a Log-rolling of a prolate spheroid in a simple shear flow. Coordinate system: $\mathbf{e}_1$ is the flow direction, $\mathbf{e}_2$ is the shear direction, and $\mathbf{e}_3$ is the negative vorticity direction. The symmetry axis of the particle is aligned with vorticity. **b** Tumbling of a prolate spheroid in the shear plane. After Fig. 1 in Einarsson *et al.* (2015b).

Subramanian & Koch (2015) who find that log-rolling is unstable in this limit. An earlier approximate theory by Saffman (1956) predicts that log-rolling is stable for nearly-spherical neutrally buoyant spheroids, at variance with direct numerical simulations of the problem at small Reynolds numbers (Qi & Luo 2003; Mao & Alexeev 2014; Rosén, Lundell & Aidun 2014). These numerical simulations were performed at small but not infinitesimal Reynolds numbers and it has been speculated that the difference between Saffman's result and the numerical results may perhaps be explained by terms of higher order in Re_s. Our

results show that it is not necessary to appeal to higher-order effects because log-rolling is in fact unstable for nearly-spherical neutrally buoyant spheroids.

Method

We solved the coupled particle-flow problem using a reciprocal theorem (Subramanian & Koch, 2005; Lovalenti & Brady, 1993) to calculate the torque exerted on the particle by the fluid to linear order in Re_s. Inserting the resulting expression for the torque into the equation of motion for the orientation vector $\boldsymbol{n}$ (aligned with the symmetry axis of the particle) and expanding to linear order in the Stokes number, St, we obtained an effective equation of motion for $\boldsymbol{n}$. At small Re_s=St this equation admits two periodic orbits shown in Fig. 1, log rolling and tumbling in the shear plane. By means of linear stability analysis we determined how the stability of these two orbits depends on the aspect ratio λ describing the shape of the spheroidal particle. Details of the calculations are given in (Einarsson *et al.* 2015a; Einarsson *et al.* 2015b; Candelier *et al.* 2015).

Results

The results are summarised in Fig. 2. This figure shows the linear stability exponents γ_{LR} and γ_{T} of the log-rolling and tumbling orbits (Fig. 1) for Re_s=St. We see that the log-rolling orbit is unstable for prolate particles, also for nearly spherical prolate particles. In the slender-body limit this result is consistent with the results of Subramanian & Koch (2005) who also observed that log-rolling is unstable in this limit. Tumbling in the shear plane is stable for prolate particles. For oblate particles the stabilites are reversed, provided that the aspect ratio is not too small: Fig. 2 shows that very flat disks exhibit stable tumbling and log rolling.

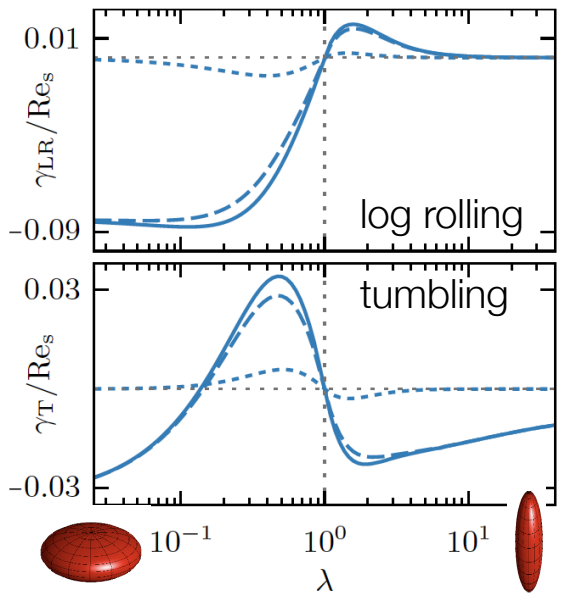

Figure 2: Stability exponents of log-rolling (top) and tumbling (bottom) orbits as a function of particle aspect ratio, solid lines. Separately shown are the contributions of particle inertia (dotted lines) and fluid inertia (dashed lines). After Fig. 2 in Einarsson *et al.* (2015a).

The contributions from fluid inertia and particle inertia are shown separately in Fig. 2. We see that fluid inertia has a much stronger effect than particle inertia. In (Einarsson *et al.* 2015b) we also computed separately the unsteady and convective fluid-inertia contributions and found that both affect the orientational dynamics. It would be wrong to neglect either of them.

References

F. Candelier, J. Einarsson, F. Lundell, B. Mehlig, J. R. Angilella (2015). *The role of inertia for the rotation of a nearly spherical particle in a general linear flow*, Phys. Rev. E, in press

J. Einarsson, F. Candelier, F. Lundell, J. R. Angilella & B. Mehlig (2015a). *Effect of weak fluid inertia upon Jeffery orbits*, Phys. Rev. E **91**, 041002

J. Einarsson, F. Candelier, F. Lundell, J. R. Angilella & B. Mehlig (2015b). *Rotation of a spheroid in a simple shear at small Reynolds number*, Physics of Fluids, in press

G. B. Jeffery (1922). *The Motion of Ellipsoidal Particles Immersed in a Viscous Fluid*. Proc. R. Soc. A**102**, 161

P. Lovalenti and J. Brady (1993). *The force on a bubble, drop or particle in arbitrary time-dependent motion at small Reynolds number*. J. Fluid Mech. **256**, 561

W. Mao and W. Alexeev (2014). *Motion of spheroid particles in shear flow with inertia*. J. Fluid Mech. **749**, 145

P. G. Saffman (1956). *On the motion of small spheroidal particles in a viscous liquid.* J. Fluid Mech. **1**, 540

G. Subramanian & D. L. Koch (2005). *Inertial effects on fibre motion in simple shear flow*. J. Fluid Mech. **535**, 383

T. Rosén, F. Lundell, and C. K. Aidun (2014). *Effect of fluid inertia on the dynamics and scaling of neutrally buoyant particles in shear flow*. J. Fluid Mech. **738**, 563

D. Qi and L. Luo (2003). *Rotational and orientational behaviour of three-dimensional spheroidal particles in Couette flows.* J. Fluid Mech. **477**, 201

Extended Abstracts (Regular Talks)

Detailed Simulations of Early Paper Forming

Gustav Kettil[1], Andreas Mark[1], Frida Svelander[1], Ron Lai[2],
Kenneth Wester[3], Mats Fredlund[4], Maria Rentzhog[4], Fredrik Edelvik[1]

[1]*Fraunhofer-Chalmers Centre, Gothenburg, Sweden*
[2]*Akzo Nobel Pulp and Performance Chemicals AB, Bohus, Sweden*
[3]*Albany International, Halmstad, Sweden*
[4]*Stora Enso, Karlstad, Sweden*

Keywords: fiber suspension simulations, fluid-structure interaction, immersed boundary methods

Abstract

Computer simulations are important to increase the knowledge of the processes involved in paper making. Because of the complexity of the paper processes the development of simulation tools requires models and numerical methods which capture as much as possible of the real physical phenomena. In this paper a framework for simulation of fiber suspension flow is presented. The framework is founded on a fluid solver for the Navier-Stokes equations and a fiber model based on finite strain beam theory including shearing. Moreover, the coupling between fibers and fluid is resolved with the immersed boundary method and the interaction between the fibers is calculated using a model based on DLVO-theory.

Introduction

Paper is, both in view of accessibility of resources and sustainable properties, an excellent material. Still there is much that is unknown about the fundaments of the processes of paper making. One relatively new approach for increasing the knowledge of these processes is by computer simulations. The complex structure of the fiber suspension and the advanced behaviour of the fluid entail profound requirements on the simulation software. The algorithms and numerical methods have to be very efficient.

Paper making involves several processes which potentially could be integrated in a simulation framework, such as the forming, pressing, and drying sections of the paper machine. The project which this publication originates from focuses on the forming section, more specifically the part where the fiber suspension leaves the headbox and impinges on the forming fabric. The aim of the project is to be able to, in a computer, simulate this process with varying input data, such as composition of the fiber suspension, fluid properties, and fabric properties.

In previous approaches for simulation of fiber suspensions, fibers have been modelled as built up of chains of spheres connected with springs (Yamamoto and Matsuoka 1994), chains of prolate spheroids (Ross and Klingenberg 1997), or chains of rigid rods (Lindström 2007). These works are however not based on beam theory which is the case for the framework used in this paper. Immersed boundary methods have previously been used to study the flow of fibers and particles in a fluid in (Stockie 2002, and Kang and Suh 2011).

In the simulation framework presented in this paper the fibers are modelled as multiple slender beams with elliptical cross sections and a finite element discretization is used (Svenning 2011) to model their motion and deformation. The fluid flow is computed using a Navier-Stokes solver and immersed boundary methods are utilized to resolve the flow around each fiber (Mark and van Wachem 2008). The interactions between fibers are modelled using DLVO-theory (Derjaguin and Landau 1941, and Vervey and Overbeek 1948).

Simulation Framework

The simulation framework described in this paper consists of several components where the fiber model, fluid model, their mutual coupling, and the fiber-fiber interaction are the most essential. In addition to these also a fiber generator is included and a rigid object representation of forming fabrics.

The fiber model is based on finite strain beam theory including shearing (Simo and Vu-Quoc 1988), which is important because of the difference in stiffness in the different directions of the fiber. A fiber is discretized with the finite element method, which together with an implicit Newmark-Wilson time stepping algorithm (Simo and Vu-Quoc 1988) results in a system of equations. In the discretization, each fiber is divided into a number of segments that are represented by a node at each end point, and two consecutive segments have one common node. These nodes have six degrees of freedom: three translations and three rotations. Each time step of a simulation, the rotation, translation, and deformation of each fiber are solved through a non-linear matrix equation. External forces can be applied to the fiber nodes explicitly. In Figure 1 three fibers are shown.

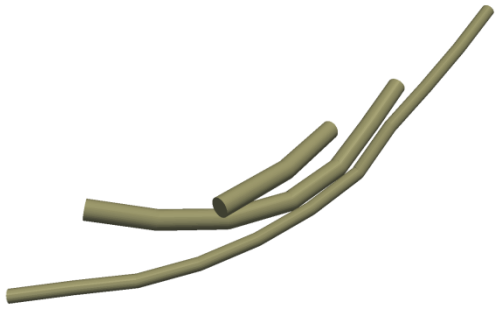

Figure 1: Three fibers in the simulation framework built-up of multiple cylindrical segments.

The fluid model is based on Navier-Stokes equation for an incompressible fluid:

$$\rho\frac{\partial u}{\partial t} + \rho u \cdot \nabla u - \mu\nabla^2 u = -\nabla p, \qquad (1)$$

which is discretized using the finite volume technique and solved in a segregated way using the SIMPLEC (Doormal and Raithby 1984) method to couple the pressure and velocity. The variables are stored in a co-located arrangement and the interpolation proposed by Rhie and Chow (1983) is used to avoid pressure oscillations.
To resolve the coupling between fibers and fluid the hybrid mirroring immersed boundary method (Mark et al. 2011) is utilized. The fluid force on the fibers is calculated by integration over the element surface numerically.
The fiber-fiber interactions are computed using a contact force model based on DLVO theory. The DLVO force is a sum of the van der Waals force and the electrostatic force. These forces are active on separation distances of only 1-5 nm. In Figure 2 an example of a DLVO force between two particles are shown.

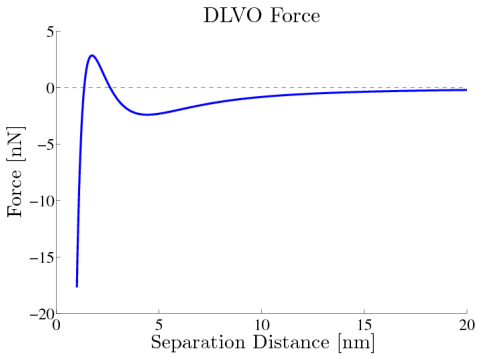

Figure 2: Representation of a typical DLVO force acting on a single particle in contact with another particle.

To circumvent the large scale differences between the action of the DLVO force and the size of the fibers a system of differential equations is solved during each time step. The system reads:

$$\frac{d^2 p_i}{dt^2} = a_{i,0} + \frac{1}{m_i}\left(\sum_{j\in J_i} F_{i,j,\mathrm{DLVO}} + F_{\mathrm{Drag}} + F_{\mathrm{g}}\right), \qquad (2)$$

where p_i are the positions of the contact points that are distributed along the fiber segments and used to calculate the DLVO force. The DLVO theory is restricted to separation distances larger than approximately 1 nm. Therefore the force formula has been extended to handle all surface separation distances, even negative. This is important since the time stepping of the fiber can result in overlaps. The contact model is developed for fibers with cylindrical cross section. Interaction between fibers and rigid objects such as forming fabrics are handled with the same contact model.
For generation of fibers in a simulation a fiber generator based on experimental fiber data is used. The experimental data is for length, width and shape of fibers. Values for individual fibers are randomly generated.

Simulation Setup

In the setup of a lay down simulation a fluid domain is used in which a small part (3x3 mm) of a forming fabric is positioned. In Figure 3 a snapshot of a lay down simulation is shown.

Figure 3: A snapshot of a lay down simulation.

Fibers are injected by the generator and the flow is driven by a pressure drop. The boundary conditions for the fluid domain are the pressure drop at the z-top and outlet at the z-bottom. On the x-z and y-z planes surrounding the domain, symmetry boundary conditions are used. To prevent fibers from leaving the simulation domain through the x-z and y-z boundaries rigid planes are used. Fibers exiting the outlet at the z-bottom are removed.
For coupling between the fluid and fibers two choices are available, either one-way coupling where only the fluid is affecting the fibers or two-way coupling, where also the fibers affect the fluid flow.
Fiber length and width are sampled from an experimental data set with sample mean L_m = 0.97 mm and standard deviation L_σ = 0.91 mm for the length, and w_m = 29.1 µm and w_σ = 14.4 µm for the width. This corresponds to a mean aspect ratio of 33.3.
After a lay down simulation is completed the permeability of the sheet can be simulated and properties such as thickness and grammage can be calculated.

Results and Discussion

The fiber beam model used has been validated by Mark and Svenning et al. (2011) and the behaviour of single fibers in fluid flow by Svenning and Mark et al. (2012). Further validation for lay down simulations of fiber suspensions still remains. A first approach has been to compare the simulation framework with experimental data for low-density sheets. In the experimental setup seven different lay downs including light pressing were performed with different injection masses. The air permeability and thickness of the sheets were measured. In the simulation setup five lay down simulations were performed and the air permeability of these sheets were simulated and the thickness calculated. Note that no pressing was included in the simulations. A comparison of the experimental and simulated data is shown in Figures 4 and 5.

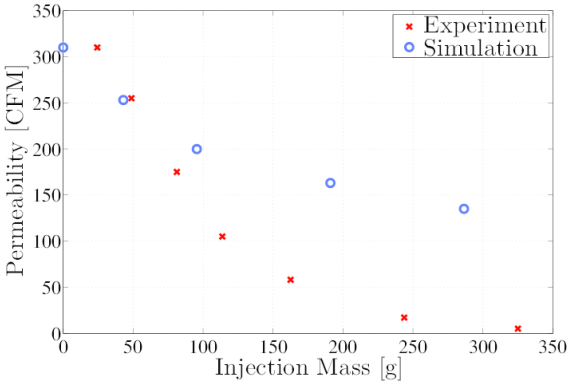

Figure 4: Comparison between simulated and experimental permeability data. The experimental data is shown with crosses and the simulated data with circles.

As can be seen in Fig. 4 the simulated permeability for the lowest densities corresponds well to the experimental sheets but when the density increase the simulated permeability is too high. Comparing the thickness in Figure 5 it can also be seen that the simulated sheets have about ten time's higher thickness than the experimental sheets. Two explanations for this are firstly that no pressing is included in the simulation and secondly that cylindrical cross sections are used for the fibers instead of rectangular-like cross sections which is the case in reality.

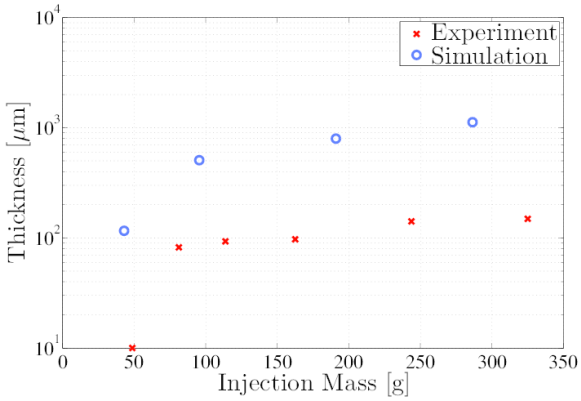

Figure 5: Comparison between simulated and experimental thickness data. The experimental data is shown with crosses and the simulated data with circles.

Cylindrical cross sections are used because the current contact model requires it.

Conclusions and Current Development

The framework for simulation of paper forming presented in this has been validated regarding the fiber model and single fibers in fluid flow. For larger scale validation comparison between permeability for experimental and simulated sheets shows that the values agree well for the lowest densities but are too high for higher densities.
To improve the framework two topics have to be addressed. One is to extend the contact model to rectangular cross sections, another is to add pressing to the framework.
A first implementation of pressing, where a rigid plane with fixed velocity is pressing the fibers is currently being tested. The same contact model as between fiber-fiber interactions is used. Preliminary results can be seen in Figure 6 where the same simulated sheet before and after pressing is shown. The simulated air permeabilities before and after pressing were 156 CFM and 86 CFM, respectively.

Also the extension of the contact model to rectangular cross sections is currently under development. Preliminary simulations are shown in Figure 7 where the same number of fibers (5000) has been simulated with cylindrical and rectangular cross section, respectively. The result shows that the thickness of the sheet is much lower in the latter case.

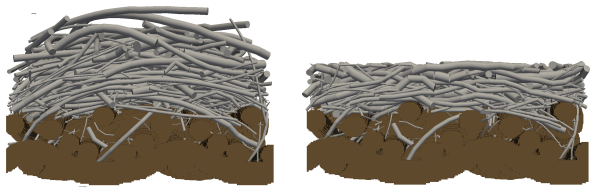

Figure 6: The same simulated sheet before (to the left) and after (to the right) pressing. The simulated air permeabilities are 156 (left) and 86 (right) CFM.

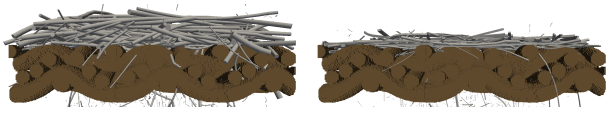

Figure 7: Lay down simulation of 5000 fibers with cylindrical cross sections (left) and rectangular cross sections (right). Given an experimental width w, the diameter of the cylinder is set to w and for the rectangular case the width is $0.7w$ and height $0.3w$.

Combining these two improvements, pressing and rectangular cross sections, will presumably decrease the permeability and thickness to the levels measured in the experiments.

Acknowledgements

This work is a part of the ISOP (Innovative Simulation of Paper) project which is performed by a consortium consisting of Akzo Nobel Pulp and Performance Chemicals, Albany International, Stora Enso and Fraunhofer-Chalmers

Centre. The work was partly founded by ÅForsk (Ångpanneföreningen's Foundation for Research and Development) research grant 12-155: "Innovative Tools for Multi-Scale Simulation of Fiber Suspensions".

References

Derjaguin, B.V., Landau, L.D., Theory of the Stability of Strongly Charged Lyophobic Sols and of the Adhesion of Strongly Charged Particles in Solution of Electrolytes, *Acta Physicochimica URSS*, Vol. 14, pp. 633-662, 1941.

Van Doormaal, J.P and Raithby, G.D., *Numer. Heat Transfer* 7: 147 (1984).

Kang, A. and Suh, Y. An immersed-boundary finite volume method for direct simulation of flows with suspended paramagnetic particles, *Int. J. Numer. Meth. Fluids* 67 (1), 58-73 (2011).

Kettil, G., Svelander, F. "Contact Force Modeling in the Paper Forming Process", Master thesis, Chalmers University of Technology, June 2014.

Lindström, S.B., "Simulations of the dynamics of fibre suspension flows", Lic. thesis, Mid-Sweden University, Sundsvall (2007).

Mark, A., Rundqvist, R. and Edelvik, F., Comparison Between Different Immersed Boundary Conditions for Simulation of Complex Fluid Flows, *Fluid Dynamics and Material Processing*, Vol. 7(3), pp. 241, 2011a.

Mark, A., Svenning, E., Rundqvist, R., Edelvik, F. et al., Microstructure Simulation of Early Paper Forming Using Immersed Boundary Methods, *TAPPI Journal*, Vol. 10 (11), pp. 23-30, 2011.

Mark, A. and van Wachem, B.G.M., Derivation and Validation of a Novel Implicit Second-Order Accurate Immersed Boundary Method, *Journal of Computational Physics*, Vol. 227, pp. 6660-6680, 2008.

Rhie, C. and Chow, W. Numerical Study fo the turbulent flow past an airfoil with trailing edge separation, AIAA J1 21, 1527-1532 (1983).

Ross, R.F. and Klingenberg, D.J., *J. Chem. Phys.* 106(7): 2949 (1997).

Simo, J.C. and Vu-Quoc, L. On the dynamics in space of rods undergoing large motions – a geometrically exact approach. *Computer Methods in Applied Mechanics and Engineering,* 66:125-161, 1988.

Stockie, J. Simulation the dynamics of flexible wood pulp fibers in suspension, In: *Proc. of the 16th Ann. IEEE Symp. On HPG Syst. and App.* Pp 145-151 (2002).

Svenning, E., Development of a nonlinear Finite Element beam model for dynamic contact problems applied to paper forming, Master thesis, Chalmers University of Technology, Göteborg, Sweden, 2011.

Svenning, E., Mark, A., Edelvik, F. et al., Multiphase Simulation of Fiber Suspension Flows Using Immersed Boundary Methods, *Nordic Pulp & Paper Research Journal*, Vol. 27 (2) , pp. 184-191, 2012.

Vervey, E.J.W., Overbeek, J.Th.G., *Theory of the Stability of Lyophobic Colloids*, Elsevier, Amsterdam, 1948.

Yamamoto, S. And Matsuoka, T., *J. Chem. Phys.* 100(4): 3317 (1994).

Rheology of pulp fibre suspensions at medium and high consistency

Florin Ciolacu[1]

[1]*Department of Natural and Synthetic Polymers, "Gheorghe Asachi" Technical University of Iasi, Iasi, Romania*

Keywords: rheology, pulp fibre suspensions, consistency, vaned rotor

Abstract

The paper presents the design, calibration and validation of a rotational device that has been adapted to measure the rheological behaviour of pulp suspensions. The effect of fibre refining degree and fibre mass concentration on flow dynamics in a rotating shear tester has been quantified as a function of the shear stress. It was found that suspension shear stress decreases by reducing the fibre mass concentration and/or the fibre length.

Introduction

Flow of fibre suspensions is a key factor in papermaking. Suspensions of pulp fibres are processed in paper industry in various ranges by mass consistency, C_m (mass of fibres divided by the total mass of suspension). Kerekes et al. (1985) classified the ranges as follows: low consistency LC (C_m=0–8%), where the suspension is a water–fibre slurry; medium consistency MC (C_m=8–20%) created by dispersing a mat formed by vacuum filtration of low consistency suspension; high consistency HC (C_m=20–40%) formed by mechanically pressing water from a medium consistency suspension and ultra-high consistency (Cm=40%) formed by evaporative drying. (Derakhshandeh et al. 2011). However, the terms low-, medium- or high consistency have not the same meaning for papermakers. Table 1 contains the meanings of these terms for the various operations in which fibrous suspensions are involved in papermaking.

Table 1 Consistency definitions

	Slushing	Screening	Cleaning	Bleaching	Refining
LC	< 6.0%	<1.5%	<1.5%	-	3.0–6.0%
MC	< 12%	<4.5%	<2.5%	10 - 15%	10–13%
HC	< 19%	-	2.5–6 .0%	25–35%	28–35%

The flow dynamics of fibre suspensions have been discussed by many authors; however, the best way to measure and to define their rheological properties is still under discussion. At this moment, there are no standard methods for measuring the rheological behaviour of pulp suspensions under typical papermaking conditions.

Fibre suspension flocculation phenomena are essential for papermaking since they directly affect the fluid mechanics of fibre suspension flows (Holm, 2004) and the sheet formation process. Consequently, fibre flocculation is considered as a key factor for paper formation, paper strength, paper opacity, machine runnability and efficiency, coating and printing quality, etc.

There is no doubt that fibre length is one of the most important papermaking characteristics of fibres. A long fibre is able to establish a large number of bonds to other fibres and as such will be anchored more strongly in a fibre network compared with a short fibre; on the other hand, fibres which are too long form papers with a structure of great unevenness - poor formation (Ciolacu, 2013).

Rheometer is a highly sophisticated item of instrument engineering both in development, manufacturing and marketing and also for the consumers and users. At present the development of rheometers is justified only in individual cases by needs of existing oriented to the practical purposes branch rheological sciences. The main drawbacks of commercial rheometers in study of pulp fibre suspensions flow are the small size of gap and wall slip phenomena. To accommodate the size of fibres and flocs, gap size is increased.

Flows in rotary devices are a useful complement for the model development. The flow in a rotating shear tester operating at different velocities will return much information regarding the rheology of the pulp suspensions.

The main objective of this study was to develop a measuring device for a rotational rheometer with coaxial cylinders (Searle type) able to allow rheological characterization of fibrous suspensions at small and medium consistencies. Highlighting the influence of beating degree of pulp and stock consistency on the rheological behaviour of suspensions is another objective of this study.

Experimental Facility

Materials

For this rheological study, a bleached softwood kraft pulp was chosen as fibrous material. It was refined up to 70 minutes in a Jokro mill (ISO 5264-3: 1979) and six samples with different values of the beating degree have been achieved in this way (23, 28, 36,53, 65, 70ºSR).

Experimental equipments

For the case of a rotary device without baffles, there will be a significant slippage at the walls, especially the rotor wall. Based on existing information from previous studies (Head, 1952; Duffy & Titchener, 1975; Gullichsen & Harkonen,1981; Bennington et al.,1990) it was designed a

new geometry for a pairs of cylinders to allow the rheological study of pulp fibre suspensions on a rheometer Searle-type RHEOTEST® (Figure 1).

The inner cylinder was obtained by adapting a cylinder type S3 from a rheometer RHEOTEST® by applying six baffles on his outer surface (vaned rotor). The outer cylinder was designed and made from a transparent material (Plexiglas) in order to monitor the flow of pulp. Its diameter has been increased from the cylinder S (40 mm) to 58 mm to provide a larger flow section and the internal surface was also equipped with six rectangular section baffles.

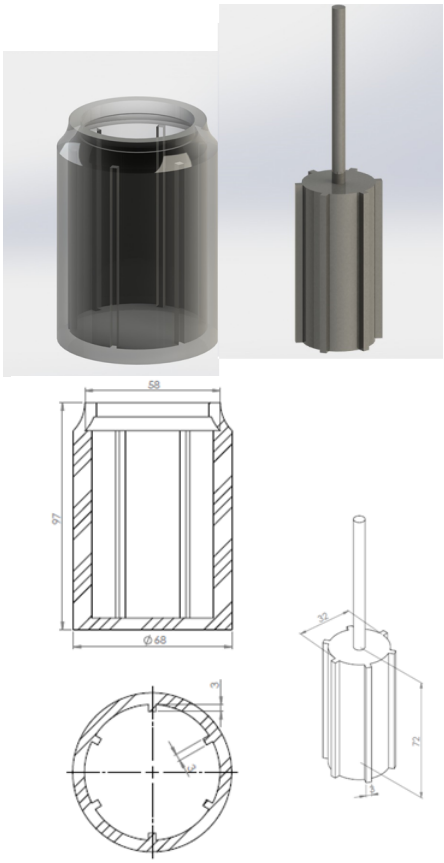

Figure 1: The new geometry of outer cylinder and vaned rotor (inner cylinder).

Calibration

A useful concept when studying fluid flows is the one regarding the dynamic similarities. A flow that at first appeared different but under same circumstances exhibits the same pattern is called dynamically similar. This concept has been used for the calibration of the viscometers. Thus, for each geometry, the non-Newtonian fluid that for a fixed rotational speed has the same torque as the calibration fluid, has also its same viscosity (Blanco, 2007).
Calibration tests with 2% CMC (carboxymethyl cellulose) solution in the same range of rates of shear were performed for the device. In the Figure 2, the calibration process is demonstrated by the same values of viscosity recorded for the same shear rates.

Results and Discussion

Figure 3 shows the viscosities for different consistencies of softwood bleached kraft pulp. The sharing rates were between 0.1 and 100[s^{-1}]. The dependence of viscosity on shear rate can be described with the power low as it can be seen on the graphics.

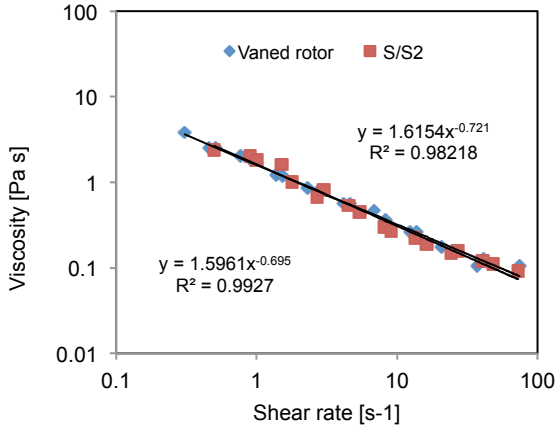

Figure 2: Calibration of new rheometer with a solution of 2% CMC

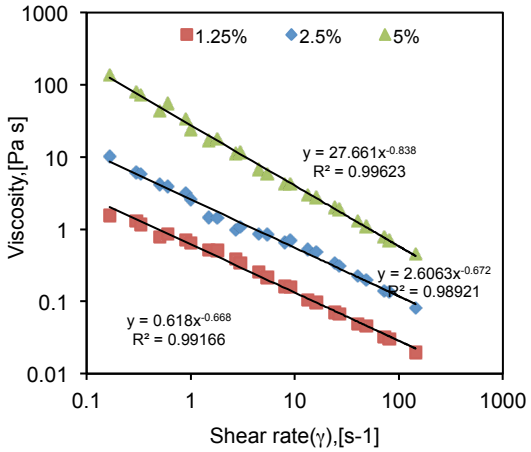

Figure 3: Viscosity *vs.* shear rate for different consistency of pulp fibre suspensions

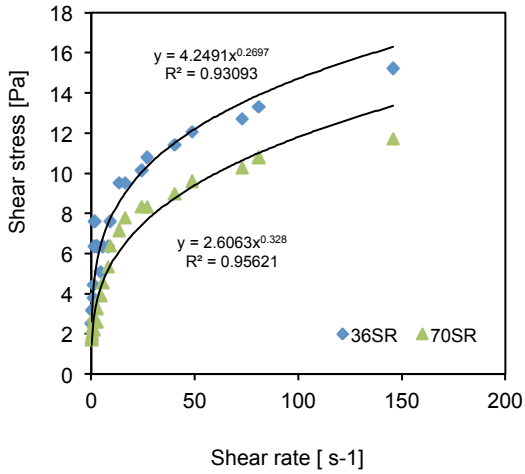

Figure 4: Shear stress *vs.* shear rate for two pulp fibre suspensions with different beating degree

Figure 4 demonstrates the dependence of the shear stress on the beating degree of cellulose fibres (in fact dependence of the shear stress on the fibres length and flexibility).

Conclusions

The new device with vaned rotor can measure the strength of fibre network to flow, the rheological behaviour of pulp suspensions at different concentrations and the pulp relative apparent viscosity. With this device it is possible to obtain good reproducibility and a high resolution within the studied concentration interval.
This equipment avoids the settling of fibres, favours the uniformity of the suspension and the interaction fibre-rotor.
The effect of fibre refining degree and fibre mass concentration on flow dynamics in a rotating shear tester has been quantified as a function of the shear stress. It was found that suspension shear stress decreases by reducing the fibre mass concentration and/or the fibre length. It is observed that the behaviour of the pulp suspension in the new viscometers was similar with that described in the literature. When the rotational speed is low, viscosity is very high due to the existence of a plug of fibres that exerts a great resistance on the rotor.

References

Bennington, C.P.J., Kerekes, R.J., Grace, J.R.,. The yield stress of fibre suspensions. Canadian Journal of Chemical Engineering 68 (10), 748–757 (1990)

Blanco, A., Negro, C., Fuente, E. and Tijero, J., Rotor selection for a Searle-type device to study the rheology of paper pulp suspensions, Chemical Engineering and Processing, 46:37-44, (2007)

Ciolacu, F., Cellulose Fibres in the Papermaking Process in Pulp Production and processing: from papermaking to high-tech products, Ed. Popa V. I., Smithers Rapra, 217-252 (2013)

Derakhshandeh, B., Kerekes, R.J, Hatzikiriakos, S.G., Bennington, C.P.J., Rheology of pulp fibre suspensions: A critical review, Chemical Engineering Science, 66, 3460–3470 (2011)

Duffy, G.G., Titchener, A.L., The disruptive shear stress of pulp networks, Svensk Papperstidning 78 (13), 474–479 (1975)

Gullichsen, J., Harkonen, E., Medium consistency technology. Tappi Journal 64 (6), 69–72 (1981)

Hammarström, D. A Model for Simulation of Fiber Suspension Flows, Licentiate thesis, Technical Reports from KTH Mechanics, Royal Institute of Technology, SE-10044 Stockholm, Sweden (2004)

Head, V.P., A shear criterion for the hydraulic behaviour of paper stocks in pumps, pipes, valves and flow meters. Tappi Journal 35 (6), 260–266. (1952)

Holm R., Doctoral thesis - Fluid mechanics of fibre suspensions related to papermaking, KTH, Stockholm, 2005.

Kerekes, R.J., Soszynski, R.M., Doo, P.A.T., The flocculation of pulp fibres. In: Proceedings of the 8th Fundamental Research Symposium, Mechanical Engineering Publications, Oxford, England, pp.265–310, (1985).

Detailed measurement of fibre suspension pipe flow velocity profile

Roope Lehto[1], Sanna Haavisto[12], Maria Cardona[3], Juha Salmela[2], Michael McCarthy[4], Robert Powell[3], Antti Koponen[5], Markku Kataja[1]

[1]*University of Jyvaskyla, Department of Physics*
[2]*Spinnova Ltd., Jyväskylä, Finland*
[3] *University of California in Davis, Department of Chemical Engineering and Materials Science*
[4] *University of California in Davis, Department of Food Science and Technology*
[5]*VTT Technical Research Centre of Finland*

Keywords: rheology, flow, optical coherence tomography, OCT, wall slip, slip flow, MFC

Abstract

A rheometric method based on velocity profiling simultaneously by optical coherence tomography (OCT) and magnetic resonance imaging (MRI) was introduced and used in a preliminary study of the rheological and boundary layer flow properties of a microfibrillated cellulose. The two velocity profiling methods appear adequate and complementary for rheological characterization of opaque complex fluids. The MRI technique is useful in measuring the velocity profile in the interior parts of the tube, while the optical technique is capable of high-resolution measurement of the boundary layer flow close to the tube wall. The results indicate typical shear thinning behaviour in the interior part of the tube. The near wall behaviour shows existence of a slip layer related to a concentration gradient near the tube wall.

Introduction

Pulp fibre wall consists of a natural composite material comprised of cellulose microfibrils. Lately, there has been a growing interest towards disintegrating the fibre structure to its elementary fibrils, thereby producing natural raw stock for novel materials. Wood pulp can be disintegrated with mechanical shearing possibly augmented with chemical and enzymatic treatments. The produced fibrils, called micro (nano) fibrillated cellulose fibres (MFC), have nanoscale diameters and length of several micrometers (Vartiainen et. al. 2011). Similar to other natural and synthetic fibre suspensions, the rheological and flow properties of aqueous MFC suspensions are diverse, and depend strongly on the fibre properties and fibre mass concentration. The general characteristics of suspensions of relatively simple fibres can, to some extent, be classified in terms of Crowding number which depends on concentration, dimensions and material density of fibres, and correlates with the mean number of contacts between fibres in the suspension. Such classification is not applicable in MFC suspension. As an aqueous suspension, MFC has interesting rheological properties, for example, gel formation at a very low concentration, thixotropy, and shear thinning behaviour. These properties derive primarily from the inherent entangled network formed during the disintegration of fibres into fibrils and are quite different from e.g. those of wood fibres. The MFC fibrils have very high specific surface area, aspect ratio, strength and flexibility which together with partially disintegrated fibres strengthen the network within the suspensions (Pääkkö et. al. 2007).

Rheometric methods utilizing velocity profiling are based on measuring the actual flow velocity profile and wall shear stress simultaneously. The techniques applicable especially for optically turbid media are typically based on Nuclear Magnetic Resonance Imaging (NMRI) (Powell et. al. 1994) or Ultrasound-Doppler Velocity Profilometry (UVP) (Wunderlich & Brunn 1999). Both UVP and NMRI have been tested for several rheologically complex fluid and multiphase systems of practical interest in e.g. in food, paper and chemical industry. The concept is well established and has been implemented as in-line rheometers in industrial processes providing means for process monitoring and quality control (Wiklund et.al. 2008)
Velocity profiling with UVP and NMRI allows replacing an assumed velocity field by an actually measured profile in analysing the data for rheological properties of the fluid. However, due to their limited spatial resolution and, especially for UVP, disturbance caused by the tube wall – fluid interface (Wiklund et.al. 2007, Wunderlich & Brunn 2000, Kotzé et. al. 2013), these methods are hardly accurate enough to resolve the flow profile in the immediate vicinity of the tube wall, where e.g. apparent slip can occur. Optical Coherence Tomography (OCT) is a non-invasive technique capable of fast real-time high-resolution imaging of the internal structure of an opaque scattering medium in the vicinity of its surface. The imaging depth of OCT is limited by the attenuation of light in the material, and can be up to 2.5 mm in air. In addition to giving access of structural data, the method can provide velocity information. Furthermore, the OCT method appears capable of accurate high-resolution measurement of velocity profile very close to a channel wall, and is thus well suited in detailed study of

the boundary layer flow behaviour of complex fluids with appropriate optical properties (Haavisto et. al 2014, Haavisto et. al. 2015).
In this work we report results on rheological and boundary layer flow properties of a micro-fibrillated cellulose suspension, obtained by a novel in-line rheological method utilizing velocity profiling. The velocity profiles are measured by combining two complementary methods, the optical coherence tomography and nuclear magnetic resonance imaging. Here, OCT is used to measure the velocity profile in the immediate vicinity of a transparent tube wall (typically closer than 0.5 mm), while NMRI provides the same information in the interior parts of the tube.

Experimental Setup

The measurement unit consisted of a 2.5 m long optical grade glass pipe with an inner diameter of 19 mm. The flow in the pipe was driven using a low-pulsation progressive cavity pump (Seepex MD series). Total volume of the sample in the flow loop and in the tank was 13.5 litres. The fluid temperature in the loop was set to 21^{o}C with a digital temperature controller (PolyScience, model 9610). The volumetric flow rate in the loop was adjusted manually using the pump control voltage. The flow rate was measured with a magnetic flow meter (Siemens, Sitrans F M MAGFLO). The flow rate range was 8-160 ml/s equalling Reynolds numbers of approximately 600-11000 (for water). The fluid temperature during each trial point was measured with a thermocouple. The wall shear stress at each flow rate was found based on pressure difference measurement between two 1.5 mm diameter taps drilled through the pipe wall located at 74 and 126 diameters downstream from the pipe inlet. The pressure difference measurement was done using calibrated sensors (Rosemount, sensor types 3051 and 2051).
Velocity profiles in the pipe flow were measured with OCT, UVP, Laser Doppler anemometry (LDA) and MRI (operated by UCDavis). The OCT device was Telesto Spectral Domain OCT having a central wavelength of 1310 nm. In order to ensure that each measurement technique is working correctly and that the operation of the flow loop is appropriate the experiments were started with tap water. The water measurements also served to demonstrate the accuracy of combining the velocity data from different techniques since the velocity profile is well known for water flow in a straight tube with circular cross-section and smooth walls.
In addition to tap water, the materials used in the experiments were xanthan gum solution, microfibrillated cellulose suspension and pine pulp suspension. Table 1 lists the used materials and some measurement details. This data will be made available in the COST Action FP1005 knowledge base. The microfibrillated cellulose used in this study was a commercial product Celish KY-100G by Daicel Industries, Japan. The microfibrillated cellulose is made of purified wood pulp, but the fibre surfaces are very strongly fibrillated compared to pine wood pulp. The used pine pulp was bleached kraft softwood also selected as a reference material in the Action. Xanthan gum used in the present study was Ticaxan by Tic Gums. MFC and pine pulp suspensions were diluted to desired concentrations and then disintegrated with a stirrer for a certain time. In addition, before each measurement series with each suspension was circulated in the flow loop for a while to stabilize the suspension structure.

Table 1. Materials and measurement techniques used in the study.

Material	Concentration	Measurement techniques used	Analysis
Tap water	-	MRI, OCT, LDA	Mean velocity profiles, viscosity
Xanthan gum	100 ppm	MRI, OCT, LDA	Mean velocity profiles, viscosity
MFC	0.4, 1 and 1.5% by weight	MRI, OCT, UVP	Mean velocity profiles, viscosity, yield stress
Pine pulp	0.4% by weight	MRI, OCT, UVP	Mean velocity profiles, viscosity, yield stress

For OCT velocity profile measurements creamer powder was added to suspension as a light scattering tracer. Structure measurements were done without added tracer. Imaging frequencies (axial scan rates) of 5.5, 28 and 91 kHz were used depending on the velocity.

Results and conclusions

In Figure 1 shown is an example of mean flow velocity profiles of 0.4% MFC in a tube of diameter 19 mm, as measured with OCT, and MRI techniques. The overall behaviour of the velocity profiles measured with OCT and MRI appears consistent, and it seems possible to construct an estimate of the entire profile after appropriate corrections and normalization of the velocity profiles with the measured flow rate. At this point, we can deduce that the high-resolution OCT data (shown in Figure 2) reveals that in a narrow near-wall region, the velocity profile is very steep and approaches rapidly zero with decreasing distance from the wall with no actual wall slip as suggested by MRI.

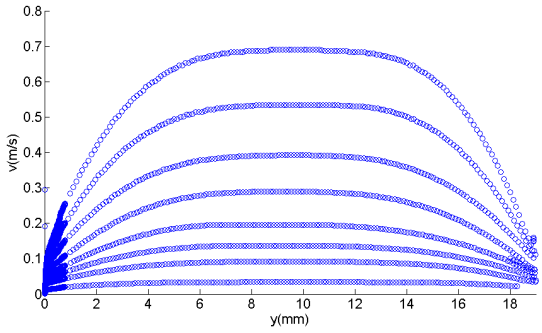

Figure 1: Flow velocity profiles for 0.4% MFC suspension, combined from OCT and MRI measurements.

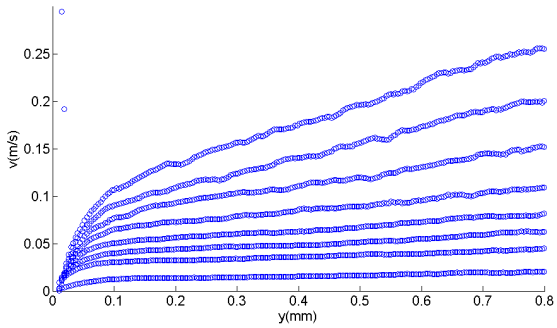

Figure 2: A closer look at the same profiles near wall, measured with OCT.

The results show typical shear thinning behaviour in the interior part of the tube while the near wall behaviour shows existence of a slip layer of thickness ~200 μm. Both the velocity profile measurement and the imaging mode data obtained by the optical coherence tomographic method indicate that the slip layer is related to a concentration gradient appearing near the tube wall. In a sublayer of thickness ~100 μm, the fluid appears nearly Newtonian, and the viscosity value approaches that of pure water with decreasing distance from the wall.

Acknowledgements

We gratefully acknowledge valuable co-operation network of COST ACTION FP 1005 (Fibre Suspension Flow Modelling) and ERCOFTAG SIG 43 (Fibre Suspension Flows). Academy of Finland (project Rheological Properties of Complex Fluids) is gratefully acknowledged for supporting this work.

References

Vartiainen, J., Pohler, T., Sirola, K., Pylkkanen, L., Alenius, H., Hokkinen, J., Tapper, U., Lahtinen, P., Kapanen, A., Putkisto, K., Hiekkataipale, P., Eronen, P., Ruokolainen, J., & Laukkanen, A. Health and environmental safety aspects of friction grinding and spray drying of microfibrillated cellulose. Cellulose, Vol. 18, 775-786 (2011)

Pääkkö M., Ankerfors M., Kosonen H., Nykänen A., Ahola S., Österberg M., Rukolainen J., Laine J., Larsson P.T., Ikkala O. & Lindström T. Enzymatic hydrolysis combined with mechanical shearing and high-pressure homogenization for nanoscale cellulose fibrils and strong gels. Biomacromolecules, Vol.8 (6), 1934–1941 (2007)

Powell, R.L., Maneval, J.E., Seymour, J.D., McCarthy, K.L. and McCarthy, M.J. The Nuclear Magnetic Resonance Imaging for Viscosity Measurements. Journal of Rheology, Vol. 38 (5), 1465-1470 (1994)

Wunderlich, T. & Brunn, P.O. Ultrasound pulse Doppler method as a viscometer for process monitoring, Flow Measurement and instrumentation, Vol. 10 (4), 201-205 (1999)

Wunderlich, T; Brunn, P.O. A wall layer correction for ultrasound measurement in tube flow: Comparison between theory and experiment. Flow Measurement and Instrumentation, Vol. 11(2), 63-69 (2000)

Kotzé, R., Wiklund, J., Haldenwang, R. Optimisation of Pulsed Ultrasonic Velocimetry and Transducer Technology for Industrial Applications. Ultrasonics, Vol. 53: 459–469 (2013)

Wiklund, J. & Stading, M., Application of in-line ultrasound Doppler-based UVP–PD rheometry method to concentrated model and industrial suspensions, Flow Measurement and Instrumentation, Vol. 19 (3-4), 171-179 (2008)

Wiklund, J., Shahram, I. & Stading, M. Methodology for in-line rheology by ultrasound Doppler velocity profiling and pressure difference techniques. Chemical Engineering Science, Vol. 62, 4277-4293 (2007)

Haavisto, S., Koponen, A.I. & Salmela, J. New insight into rheology and flow properties of complex fluids with Doppler optical coherence tomography, Frontiers in Chemistry, Vol. 2 (27), 1-6 (2014)

Haavisto, S., Salmela, J. & Koponen, A.I. Accurate velocity measurements of boundary-layer flows using Doppler optical coherence tomography, Experiments in Fluids, Vol. 56 (5) (2015).

Numerical study of fiber flocculation in the turbulent air flow of an asymmetric planar diffuser

Jelena Andric[1], Stefan B. Lindström[2], Srdjan Sasic[1], Håkan Nilsson[1]

[1]*Department of Applied Mechanics, Chalmers University of Technology, Göteborg, Sweden*
[2]*Department of Management and Engineering, The Institute of Technology, Linköping University, Linköping, Sweden*

Keywords: particle-level fiber model, fiber flocculation, turbulent flow

Abstract

Particle-level simulations are employed to investigate the flocculation of rod-like fibers in an asymmetric planar diffuser with a turbulent Newtonian fluid flow. Both the fiber inertia and non-creeping fiber-flow interactions are taken into account. The fibers are modeled as chains of rigid, cylindrical segments. The equations of motion account for hydrodynamic forces and torques exerted by the fluid on the fiber segments. The Reynolds-averaged Navier-Stokes equations together with the eddy viscosity turbulence model are used to describe the fluid motion. A stochastic model is employed to account for the turbulent fluctuations and therefore capture the fiber dispersion. The fibers are assumed to interact through short-range attractive forces that cause them to interlock in flocs whenever the fiber-fiber contacts occur during the flow. It is found that the formation of fiber flocs is governed by both the turbulent dispersion and the lateral motion of fibers which is, triggered by the flow gradients.

Introduction

Transport of elongated fibers is present in different industrial applications such as pulp and paper processing, dry-forming of pulp mats, and composite manufacturing. Understanding the mechanisms behind the suspension structure formation is essential for process design and optimization, and the improvement of product quality. The formation and disruption of fiber flocs is of particular interest. Numerical analysis of fiber suspension flow with non-creeping fiber-flow interactions represents a challenging task.

The aim of this study is to investigate the flocculation of rigid fibers in a turbulent flow field of an asymmetric planar diffuser. The particle-level rigid fiber model is used to study the fiber motion and the formation of fiber flocs is analysed.

Nomenclature

d	fiber diameter (m)
H	inlet channel height (m)
k	turbulence kinetic energy (J/kg)

Greek letters

ϕ	floc species (-)
ω	specific dissipation (1/s)

Subsripts

i,j	fiber index

Fiber Model

A fiber is modeled as a chain of rigid, cylindrical segments (Lindström and Uesaka 2007, Schmidt et al. 2000), see Fig. 1. The relative orientation between the orientation vectors of two neighbouring fiber segments remains constant, i.e. the fiber cannot deform. The present work deals only with straight fibers although the model can accommodate an arbitrary fiber shape. The total hydrodynamic force and torque exerted by the fluid on the fiber segments are expressed as the sum of the viscous (creeping fiber-flow intreactions) and inertia (non-creeping fiber-flow interactions) components, as previously proposed by Lindström and Uesaka (2007).

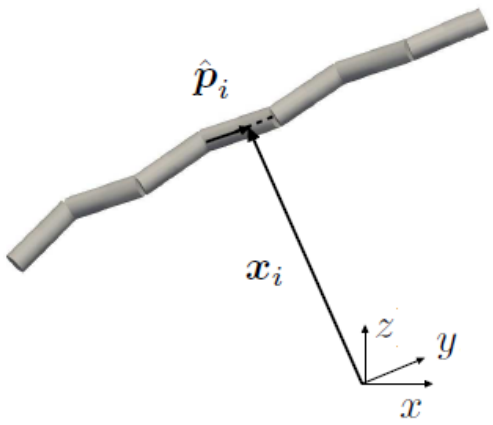

Figure 1: Fiber geometry definition. The figure illustrates a non-straight fiber, making the segments visible. The present work deals with straight fibers only.

The segment distance algorithm (Vega and Lago 1994) is used to determine whether two segments i and j from two different fibers are in contact. Figure 2 illustrates the interaction between two fiber segments. If the shortest distance between the segment surfaces is smaller than the fiber diameter d , it is assumed the fibers interact through short-range attractive forces that cause them to interlock in a floc.

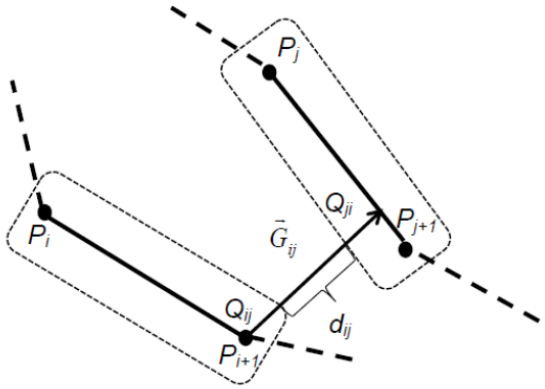

Figure2: Interaction between two segments from two different fibers.

Flow Case Description

The particle-level rigid fiber model proposed by Andric et al. (2013) is used together with the flow field in an asymmetric planar diffuser. Figure 2 shows the computational domain that is set up according to the experimental case of Buice and Eaton (2001). The steady-state incompressible Navier-Stokes equations with the standard k-ω turbulence model (Versteeg and Malalasekera 1995) are used to describe the fluid motion. The steady-state results for predicted axial velocity profiles and turbulent kinetic energy at different locations along the diffuser are validated using the experimental results of Buice and Eaton (2001) and Obi et al. (1993).

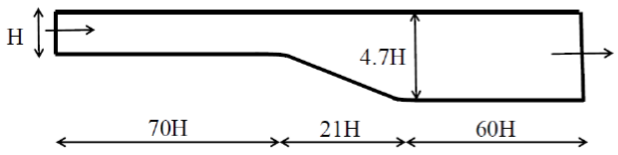

Figure3: Asymmetric planar diffuser (not to scale).

Results and Discussion

We investigate the flocculation mechanisms in dilute rigid fiber suspensions due to turbulent flow in a planar diffuser. A random walk dispersion model is used to model the turbulent fluctuations (Gosman and Ioannides 1983). The fiber positions and orientations are initially uniformly randomized. The fiber contact model is employed at each time step to find all fiber interactions. The formation of fiber flocs is observed all across the domain, see Fig. 4.

Figure 4: Fibers and fiber flocs – a fully developed solution. Top: all fibers; bottom: fibers in flocs.

The development of the mass fraction of flocs with two fibers ϕ_2 is shown in Fig. 5. The reference case is the one with the heavy fibers and activated dispersion model. A significant elevation in the flocculation rate is observed in the diffuser section. The velocity gradient in the flow direction and the inertia of the fibers lead to a velocity difference between the fibers and the flow. This relative velocity in combination with the anisotropic hydrodynamic resistance tensors of the fibers leads to the lateral fiber motion, which contributes to the flocculation rate in the diffuser. The exclusion of turbulent dispersion (dashed curve) reduces the flocculation rate. The light fibers (fiber density reduced by a factor five, dash-dotted) curve demonstrates the effect of fiber inertia. The influence of the flow gradients on the flocculation rate is supported by including the results for the reference case for the straight channel. It should be noted that that the fiber number density is greater in the channel than in the diffuser due to different total volumes.

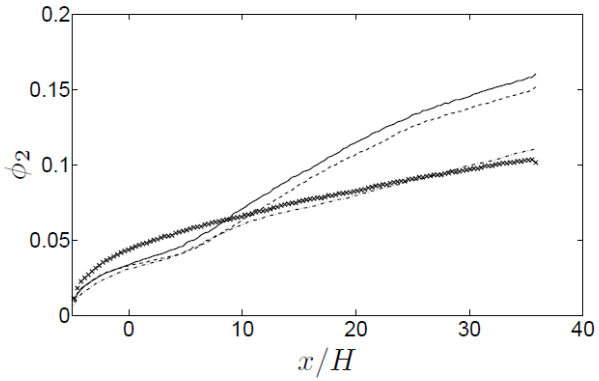

Figure 5: Mass fraction of flocs with two fibers (ϕ_2) along the diffuser. Solid curve: with dispersion model; Dashed curve: without dispersion model; Dash-dotted curve: low inertia fibers with dispersion model; Marker×: straight channel flow with dispersion model.

Conclusions

A particle-level fiber model is employed to probe the flocculation in dilute suspensions of rigid fibers in the turbulent air flow of an asymmetric planar diffuser. The fibers are represented as chains of rigid, cylindrical segments. The Reynolds-averaged Navier-Stokes equations describe the fluid flow, and a stochastic dispersion model is employed to capture the turbulent fluctuation. When fiber-fiber interactions occur, the fibers interlock in flocs. The study demonstrates that the turbulent dispersion and the

lateral motion of the fibers, triggered by the flow gradients, are the main mechanisms that govern the flocculation in the diffuser.

References

Andric, J., Lindström S.B., Sasic, S. & Nilsson H. A particle-level rigid fiber model for high-Reynolds number flow, implemented in a general purpose CFD code, 8th International Conference on Multiphase Flow ICMF (2013).

Buice, C.U. & Eaton, K.J. Experimental investigation of flow through an asymmetric plane diffuser. J Fluids Eng. 123, 819-828 (2001).

Gosman, A.D. & Ioannides E. Aspects of computer simulation of liquid-fueled combustors. J. Energy 7, 482-490 (1983).

Lindström, S.B. & Uesaka T. Simulation of motion of flexible fibers in viscous fluid flow. Phys. Fluids 19, 113307 (2007).

Obi S., Aoki K. & Masuda S. Experimental and computational study of turbulent separating flow in an asymmetric plane diffuser. 9th Symposium on Turbulent Shear Flows, Koyoto, Japan, 16-19 August (1993).

Schmid C.F., Switzer L.H. & Klingenberg D.J. Simulations of fiber flocculation: Effects of fiber properties and interfiber friction. J. Rheol. 44, 781-809 (2000).

Vega C. & Lago S. A fast algorithm to evaluate the shortest distance between rods. Computers Chem. 18, 55-59 (1994).

Versteeg H.K. & Malalasekera W. An introduction to computational fluid dynamics. Pearson Education Limited (1995).

Characteristic flocculation time in free jet of pulp of paper (nozzle of headbox)

Salaheddine Skali Lami[1]

[1]*LEMTA, University of Lorraine, Nancy, France*

Keywords: Flow of Pulp of paper Re-flocculation time, Entanglement in fibres network

Abstract

The flocculation of the fibers, resulting from a dynamic equilibrium in an established flow, changes with time when the flow parameters are changed. In order to evaluate the characteristic time of flocculation, we have studied the variation of the floc size during the passage of a flow of pulp of paper between two planes in to a free jet (wall stress discontinuity). This characteristic time is an important parameter in the papermaking process because it defines an optimal distance between the headbox outlet and the wire for a given velocity of the jet of pulp of paper.

Introduction

In the flow of pulp of paper the non-uniformity of the concentration distribution of the fibers (flocculation) in the flow is related to the intensity of turbulence in the flow (Yokogawa et al. (1985) and Shimizu et al . (1986)).
This strong flocculation-turbulence interaction determines the fiber flocculation rates in an established steady flow. The flocculation rates can evaluate by optical techniques, Shimizu and Wada (1989) used this technique to evaluate flocculation rate in the headbox in the case of high-consistency Sheet Forming. This balance flocculation/turbulence is greatly changed if the production of turbulence fades. This situation is reflected in the headbox of the paper machine where the jet exits from confined jet at outlet of headbox.
The approach proposed in this paper describes the relative change of the size of the floc due to the wall stress discontinuity that the jet undergoes its nozzle outlet. In the confined portion of the jet, the floc is subjected firstly to the turbulent stresses maintained by walls which tend to disperse flocs into individual fibers, and secondly to the elastic forces between the fibers that ensure the cohesion of flocs. In the free jet, splat particularly suffers the elastic forces that increase its cohesion and reduce its size. The behavior of the floc is then assimilated to a solid type linear viscoelastic (Kelvin-Voigt) whose the relaxation time depends on the type of fiber used and the nature of their crosslinking. This theoretical approach is based on the equations developed by Batchelor (1971).
Our experimental study is to determine the evolution of the floc size in different parts of the plane flow (confined part) and in the free jet. The goal is to evaluate the relaxation time of the floc. The measurements, made using a battery of photoelectric sensors are used to estimate the size of the flocks by signal processing (autocorrelation and cross-correlations).

Nomenclature

C	Concentration
G	Elastic modulus (Pa)
U,V	Velocity (m s^{-1})

Greek letters

σ	Stress tenser (Pa)
ε	Deformation tenser
ξ	Entanglement rate
μ	Viscosity (Pas)

Subscripts

f	floc

Experimental Facility

The headbox used is a cuboids 800 * 260 * 320 mm. Prior to that fund, the suspension (bleached Kraft 1%) passes through a cylindrical pipe (ϕ40mm) and downstream flow is confined between two planes (e = 10 mm). This channel, which forms the jet, is equipped with parietal electrochemical sensors and a linear array of photoelectric cells (8 phototransistors as TIL81 spaced by 10 mm. The photoelectric cells can be also placed on the free jet when the first cell is 10 mm from the beginning of the free jet.

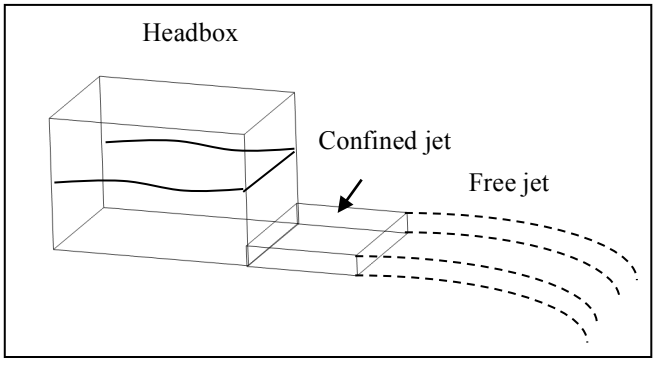

The photocells are used to evaluate the floc size. We can determine wall shear rate and therefore the wall shear stress by electrochemical method using wall probes. The velocity profiles and turbulence intensity are measured by the LDA in both parts the confined jet in the free jet.

Theoretical approach

The mean value of stress on a volume of floc can be writing by the viscous part σ_{ij} and elastic part σ'_{ij}:

$$\sigma_{ij}^{f} = \frac{1}{V}\sum_{1}^{n}\int_{A_0-A_1}\sigma_{ik}x_j n_k dA + \int_{A_1}\sigma'_{ik}x_j n_k dA \qquad (1)$$

Where A_1 is de surface of one fibre connected to other fibres and Ao is the total surface of fibre. By integration of (1) :

$$\sigma_{ij}^{f} = \sigma_{ij}C(1-\xi) + \sigma'_{ij}C\xi \qquad (2)$$

$$Where \begin{cases} C: concentration\ of\ fibres \\ \xi = 1\ fibers\ attached\ over\ their\ entire\ length \\ \xi = 0\ dispersed\ fibres \end{cases}$$

$$\sigma_{ij} = \mu\frac{d\epsilon}{dt} \quad and \quad \sigma'_{ik} = G\epsilon$$

$$Where \begin{cases} \epsilon: tenser\ of\ deformations \\ \mu: viscosity\ of\ fluid \\ G: elastic\ modulus \end{cases}$$

The equation 2 reflects the behavior of a linear viscoelastic solid type Kelvin-Voigt with creep function:

$$f(t) = \frac{1}{G\xi}\left(1 - e^{-\frac{t}{\theta}}\right) \text{ With } \theta = \frac{\mu(1-\xi)}{G\xi} \qquad (3)$$

θ : relaxation time that is function of entanglement rate ξ (ξ=1 solid behaviour; ξ=0 liquid behaviour).

Results and Discussion

With electrochemical technique, the wall shear rate show that (Fig.1) the wall shear stress of pulp of paper is higher than wall shear stress of water. This shows that the flow of pulp contains flocs for velocities ranging from 0.2 to 4 m / s. Indeed at the wall the viscosity is the same as that of either the pulp of paper or water.

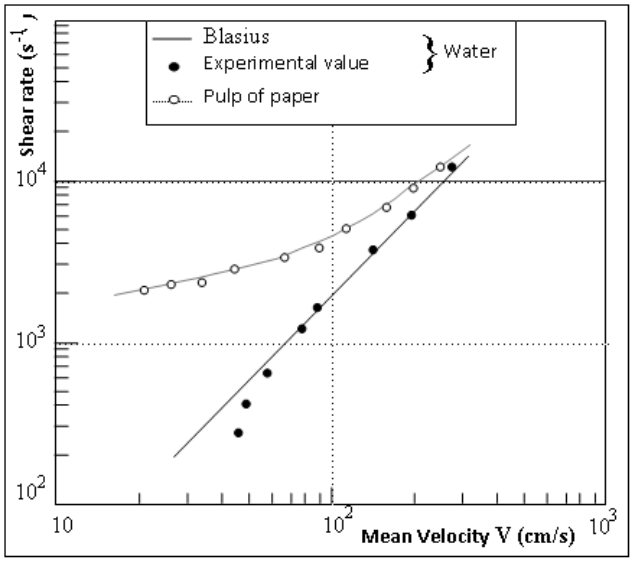

Figure 1: Wall shears rates in confined jet vs a mean velocity.

The LDA measurements (Fig.2) realised in the confined jet and in the beginning of free jet, shows that the variations of velocity profiles and the RMS of velocity. These results confirm the reduction of turbulence after the passage of the confined jet to the free jet.

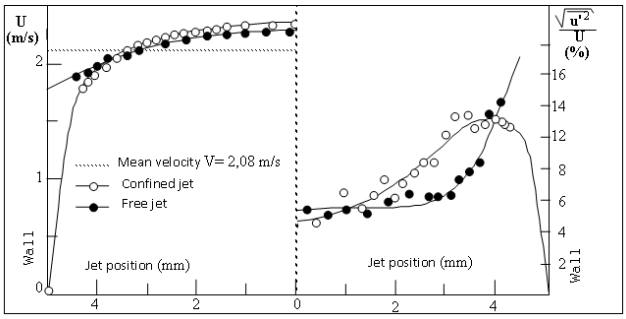

Figure 2: Velocity and RMS profiles in confined jet and free jet.

The measurement of the average floc size was performed by photoelectric cells (Fig. 3). The photoelectric cells are used also in free jet.

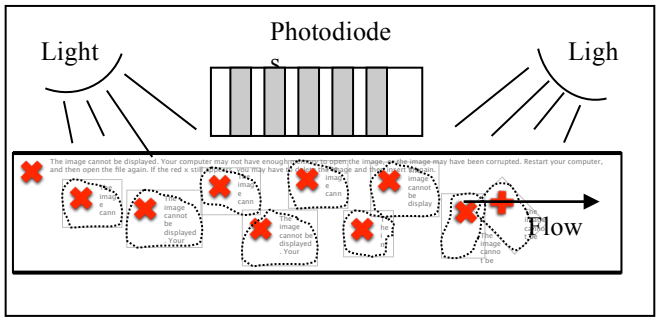

Figure 3: Schematic device for a floc size measurements

This size of flocs decreases as the velocity increases in the confined jet part (Fig. 4 and Table 5).

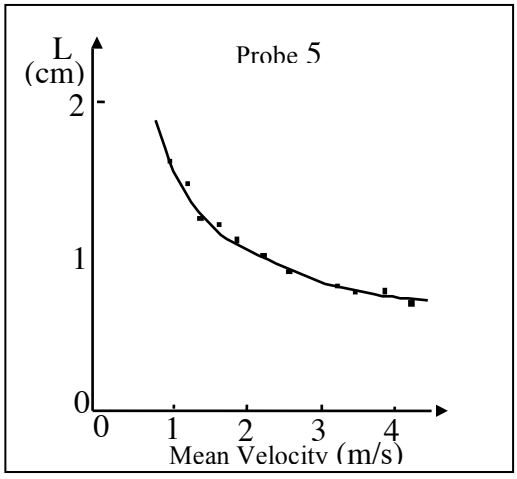

Figure 4: Floc size vs velocity in confined jet

Mean Velocity (en m/s)	1	1.5	2	2.5	3	3.5	4
Size of flocs (en cm)	1.69	1.27	1.09	0.96	0.86	0.78	0.72

Table 1: Floc size vs velocity in confined jet

In the free jet ((Fig.5) the size of floc decreases along the jet (variation over time) to a minimum and increases thereafter. This decrease is explained by the fact that turbulence fades which changes the flocculation / turbulence balance. The flocs, in this non-equilibrium situation, undergo creep by the elastic forces that decrease their size but increase their cohesion. This behavior results from the discontinuity of the production of turbulence in the jet. The elastic forces then act as restoring forces.

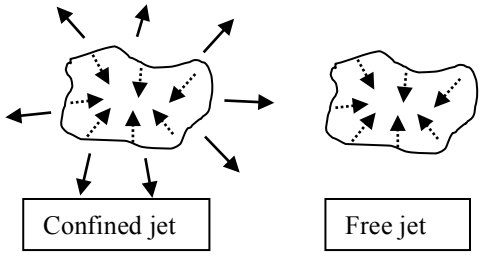

The increasing the size of the flocs beyond a certain position in the jet is due to the accumulation of free fiber on the flocs.

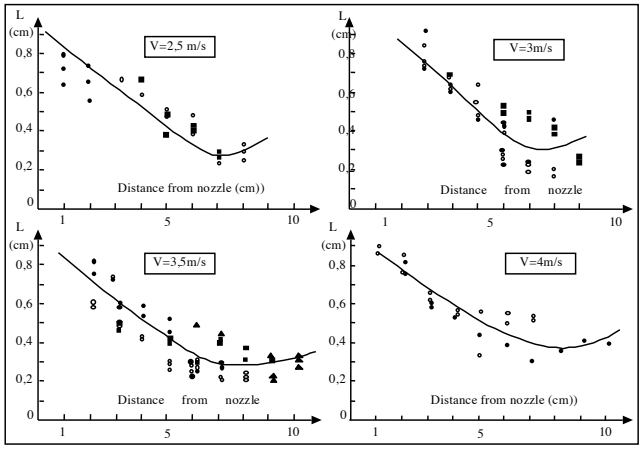

Figure 5: Size of flocs vs distance from nozzle at different velocities.

Based on the position where the floc size is minimal as it relates to the average velocity of flow we deduce a relaxation time see Table 2.

Position from the nozzle (cm)	6	7,5	8	8,5
Mean velocity (m/s)	2,5	3	3,5	4
Relaxation time (10-3 s)	24	25	23	21

Table 2: Relaxation time vs mean velocity

In the free jet, the floc size is changing along thereof. It decreases regardless of flow for approximately 23 ms (see Tab.2) and increases thereafter.
The model, based on the behavior of Kelvin Voigt, we propose to describe the behavior of the flocs (relationship 3) involves a relaxation time. Experimental results for the refined Kraft pulp (C = 10 g/L, and length l≈6mm, diameter d= 22μm), θ is 23 ms gives for μ = 1.02 10^{-3}Pa.s and G = 2Pa, used to calculate entanglement rate ξ≈3%.

Conclusions

In this study we sought to experimentally verify the relaxation time of flocculation for long fibres of pulp of paper. The measures of the size of the flocs, are carried out before the jet outlet nozzle (acting as references) and in a free jet. The results show that the size of flocs decreases in free jet bat their cohesion increases by elastic forces due to the entanglement of the fibers.
The proposed approach makes it possible to describe the flocculation of the pulp as an intermediate structure between a solid and a liquid. The results show that the relaxation time of the flocs is independent of the jet velocity and has a value of the order of 23ms for a concentration of fibers 1%. This concentration is usually used for papermaking. The relaxation time (23ms) leads to entanglement rate of the fibers in the floc of about 3%

Acknowledgements

I would like to thank the CTP (Grenoble) for helping to achieve this work

References

Yokogawa, A., Suzuki, M., Shimizu, T.. Study on flow characteristics of pulp suspension flow – measurement of turbulence intensity and fiber concentration unevenness. B. JSME 28, 846–853.(1985).

Shimizu, T., Yokogawa, A., Suzuki, M., Nakamura, I. Study on flow characteristics of pulp suspension: 2nd report – flocculation measurements of a thick fiber suspension. Bulletin JSME 29, 1487–1493. (1986).

Shimizu, T., Wada, K.. Study on flow characteristics of pulp suspension. Nippon Kikai Gakkai Ronbunshu, B Hen/Trans. Japan Soc. Mech. Engrs, B 55, 3314–3319.(1989).

Batchelor, G. K. The stress generated in non-dilute suspension of elongated particles by pure straining motion. JFM. Vol. 46, 813. (1971).

Turbulent flow of concentrated pulp suspensions in a pipe – numerical study based on a pseudo-homogeneous approach

Carla Cotas[1], Dariusz Asendrych[2], Fernando Garcia[1], Pedro Faia[3], Maria Graça Rasteiro[1]

[1]*Chemical Engineering and Forest Products Research Centre (CIEPQPF), Chemical Engineering Department, Faculty of Sciences and Technology, University of Coimbra, Coimbra, Portugal*
[2]*Częstochowa University of Technology, Institute of Thermal Machinery, Częstochowa, Poland*
[3]*Electrical and Computers Engineering Department, Faculty of Sciences and Technology, University of Coimbra, Coimbra, Portugal*

Keywords: turbulent pulp flow, drag reduction, damping function, rheology, lubrication layer

Abstract

The flow of non-Newtonian fluids is present in many processes in the pulp and paper industry. Computational Fluid Dynamics can be used to predict the flow of pulp suspensions. The commercial CFD software, ANSYS FLUENT®, was used to simulate the fully developed turbulent flow of *eucalyptus* and *pine* pulps. A pseudo-homogenous approach was applied by considering the viscosity of pulp as a function of shear rate and consistency. Additionally, the model takes into account a very thin layer surrounding the core region, lubrication layer, where just pure water or few fibres are considered to be present. The presence of fibres in that layer was implemented considering the consistency as a function of the distance to the pipe wall. Since a *drag reduction* effect has been identified in fibre suspensions flow, a low-Reynolds *k-ε* (LRN) turbulence model was applied - Chang-Hsieh-Chen (CHC) LRN model. The modification to the standard CHC LRN model was based in the damping function proposed by Bartosik (2010, 2011) to study the flow of solid particles. The new damping function includes an additional term based on the fibre aspect ratio. The numerical results were validated comparing the pressure drop values with experimental values. The CFD model is able to reproduce the *drag reduction* effect and predicts well the experimental measurements.

Introduction

The flow of non-Newtonian fluids is present in a wide range of industries, as for example, in the pulp and paper mills. The flow conditions can influence significantly the characteristics of the final product and, also, contributes for the high energy costs associated with the pulp and paper manufacturing. These energy costs can be minimised if the overdesign of industrial equipment based on empirical correlations, with a specific range of applicability, is avoided. Thus, knowledge of the pulp flow behaviour is important for the optimum design of the industrial equipment and flow systems on the pulp and paper industry.
The present study is focused on modelling the turbulent flow of *Eucalyptus* and *Pine* fibre suspensions in a pipe, applying Computational Fluid Dynamics (CFD) tools, using a commercial CFD software, ANSYS FLUENT®. The strategy followed is a pseudo-homogeneous approach in which the non-Newtonian behaviour of the pulp is incorporated by considering its viscosity as a function of shear rate and consistency. Additionally, the model takes into account the existence of a very thin layer at the pipe wall, surrounding the core region, where a few number of fibres or just pure water can be present. In the first case, the consistency is considered as a function of the distance to the pipe wall. The fact that *drag reduction* effects have been identified in the flow of pulp suspensions, makes appropriate to select low-Reynolds *k-ε* (LRN) turbulence models. The turbulence model studied was the Chang-Hsieh-Chen (CHC) LRN turbulence model (Chang et al. 1995). This model was implemented using User-Defined Functions (UDFs) on ANSYS FLUENT. This type of approach, in spite of its wide application to study polymers and particulate flows, has seldom been tried to deal with pulp fibre suspensions flow. The damping function f_μ on the CHC turbulence model was modified taking into account the modifications proposed in the literature (Bartosik 2010, 2011) to study the turbulent flow of spherical particles, when a *drag reduction* effect is present. A modified version of this damping function taking into account the characteristics of the fibres is proposed. The model parameters were tuned based on experimental information about the flow and rheology of pulp suspensions, and then validated by comparing the numerical pressure drop with the experimental values. A good fitting was achieved for pressure drop values when considering the new damping function proposed in this work.

Nomenclature

c	pulp consistency (% w/w)
$\bar{c}$	mean pulp consistency (% w/w)
f_μ	damping function
L_{fibre}	fibre length (m)
r	radial coordinate equation (2)
r	fibre aspect-ration equation (3)
R	pipe radius (m)
U_b	bulk velocity (m s^{-1})

Greek letters

$\Delta P/L$	Pressure drop (Pa m^{-1})
$\dot{\gamma}$	shear rate (s^{-1})
μ	dynamic viscosity of suspension (Pa s)
τ_y	yield stress (N m^{-2})
τ_w	wall shear stress (N m^{-2})

Experimental Facility

The experimental information used in this work to tune and validate the CFD model involves flow data and rheological data. Two different types of pulp were studied: *Eucalyptus* and *Pine* pulp suspensions.

The rheological information was adopted from (Blanco et al. 2007 ;Ventura et al. 2007). The viscosity expression can be represented as a function of shear rate and consistency by the following equation (Cotas et al., 2015):

$$\mu = K'_c \left(\dot{\gamma}\right)^{\alpha_c \beta_c} \quad (1)$$

The surface fitting of equation (1) to the rheological data leads to the following parameters: (*i*) *Eucalyptus* pulp – K'=0.0085, α=6.97 and β=-0.26 (R^2=0.98), and (*ii*) *Pine* pulp – K'=0.0754, α=5.90 and β=-0.28 (R^2=0.94).

The flow data was adopted from (Ventura et al. 2008, 2011) where the pressure drop was obtained in a pilot rig properly adapted to study the flow of pulp suspensions. The test section was composed of a smooth pipe with a total length of 4 m and pipe diameter of 0.0762 m. The fully developed turbulent flow was simulated for two consistencies in each pulp tested: (*i*) *Eucalyptus* pulp – 1.50 and 2.50% w/w, and (*ii*) *Pine* pulp – 1.50 and 2.30% w/w, considering different mean flow velocities for each consistency.

Numerical Approach

The strategy followed in this work is based on a rheological single-phase model. The flow is assumed as: (*i*) incompressible flow, (*ii*) steady-state, (*iii*) non-Newtonian fluid flow, (*iv*) isothermal, and (*v*) 2D axisymmetric geometry. Two distinct regions are considered, the core region where the non-Newtonian behaviour of pulp is implemented in the CFD model considering equation (1) taking into account that the mean pulp consistency is constant, and the lubrication layer where the presence of fibres or just pure water can be considered. This last case is implemented imposing the viscosity in the lubrication layer equal to water viscosity. If the model takes into account the presence of fibres in the lubrication layer, the pulp consistency is considered as a function of distance to the pipe wall described by the following expression:

$$c(r) = \bar{c} - \bar{c}\left\lfloor r - \left(R - L_{fibre}\right)\right\rfloor / L_{fibre} \quad (2)$$

where L_{fibre} is equal to 0.706mm, *Eucalyptus* pulp, and 2.564 mm, *Pine* pulp. Detailed information is presented in Cotas et al. (2015).

The CHC LRN turbulence model was chosen to model turbulence since a *drag reduction* effect was proved experimentally. The complete system of equations and numerical solution procedure is described in Cotas et al. (2015). The modifications studied by Bartosik (2010, 2011) to simulate the turbulent flow of solid particles with success, motivated the replacement of the *original* damping function f_μ in the CHC model by a different damping function. In a first stage the original Bartosik damping functions were tested. However, since this approach did not provide a good enough fit, further modifications were introduced. This new damping function is based on the damping function proposed by Bartosik (2010, 2011) adapted to incorporate the fibres characteristics as described by equation (3):

$$f_\mu = exp\left[-\frac{3.4\left(1+\tau_y/\tau_w\right)+r^{1/4}\left(1+\mathrm{Re}_t/50\right)^2}{\left(1+\mathrm{Re}_t/50\right)^2}\right] \quad (3)$$

where r is the fibre aspect ratio calculated considering a fibre diameter of 0.016mm. The wall shear stress τ_w is calculated based on the experimental pressure drop as suggested by Bartosik (2010). The yield stress was obtained from the experimental rheological data. From this data it was to describe yield stress as a function of pulp consistency by a simple power equation:

$$\tau_y = A\, c^B \quad (4)$$

Eucalyptus pulp – A=1.59, B=2.32, and *Pine* pulp – A=7.94, B=2.08.

Results and Discussion

The main result evaluated is the pressure drop. In Figure 1 are presented the numerical and experimental pressure drop values obtained for the *Eucalyptus* and *Pine* pulp tests when the model takes into account the presence of fibres in the lubrication layer, equation (2). The results obtained when just pure water is considered in the lubrication layer, are presented in Figure 2.

As expected, the standard CHC LRN model is able to reproduce the *drag reduction* effect. However, the pressure drop values are still not acceptable and those values are over-predicted.

The CHC LRN model with the new damping function (Figures 1 and 2, CHC model modified) proposed in this work, equation (3), is able to reproduce the *drag reduction* effect present in the turbulent flow of pulp suspensions. The numerical predictions reproduce well the experimental pressure drop measurements either when considering the flow of *eucalyptus* or *pine* pulp. The differences observed, mainly for the lower consistency case (*eucalyptus* pulp) can be due to poor accuracy of the rheological fitting. The rheological information is not accessible for very low shear rates where the main differences in viscosity are present. This fact results in a viscosity equation which is adequate for most of the cases tested, but which is not able to deal properly with the very low shear rate zones.

The inclusion or not of fibres in the lubrication layer (Figures 1 and 2) is not influencing significantly the numerical predictions. However, the CFD model should be as realistic as possible, thus, the presence of fibres in the lubrication layer gives physical meaning to the model even

if no significant numerical deviations were observed.

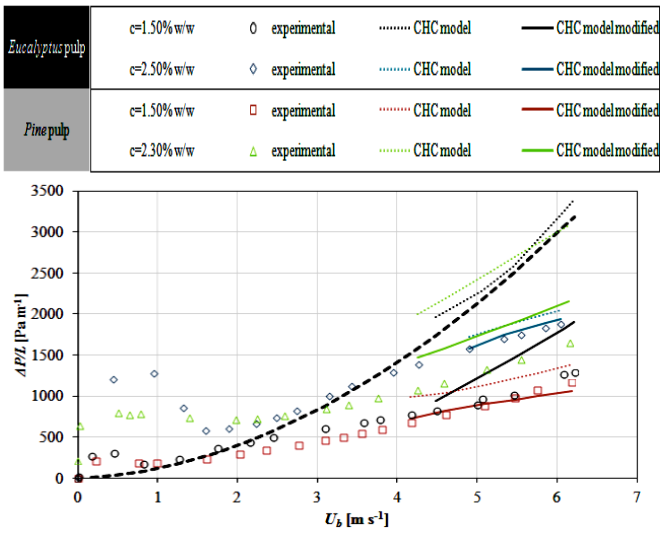

Figure 1: Pressure drop values, *Eucalyptus* and *Pine* pulp flow, considering the presence of fibres in the lubrication layer. Dashed line corresponds to the pressure drop for only flow of water in the same pipe.

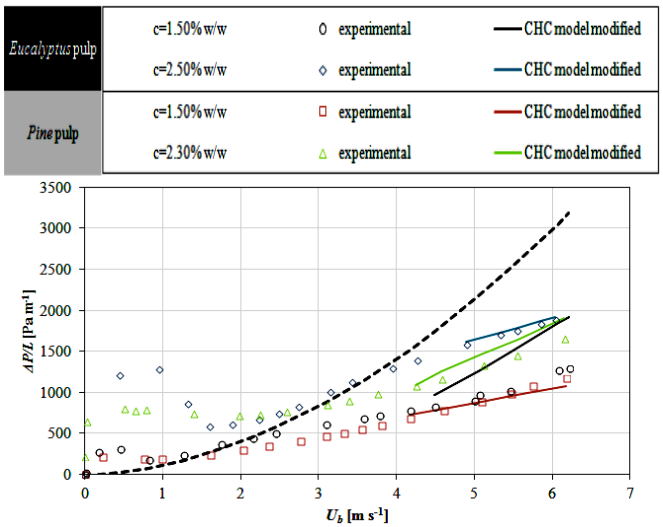

Figure 2: Pressure drop values, *Eucalyptus* and *Pine* pulp flow, considering just pure water in the lubrication layer. Dashed line corresponds to the pressure drop for only flow of water in the same pipe.

Conclusions

In the present work a numerical study of *eucalyptus* and *pine* pulp flow under different conditions, using the commercial CFD software ANSYS Fluent, was performed. UDFs were used to reproduce the CHC LRN model and to implement modifications in the CFD model. These modifications focussed on the non-Newtonian behaviour of pulp suspensions (local viscosity as a function of local shear rate and local consistency). Also a very thin layer, near the pipe wall, surrounding the core region, where no fibres or a very low concentration of fibres was considered, was investigated. Additionally, the CHC LRN model was modified by introducing a modified version of the damping function proposed by Bartosik (2010, 2011) that had been used successfully to predict the flow of solid particles.

The *drag reduction* effect which has been described in the case of fibre suspensions flow could be reproduced with the standard CHC LRN model as well as with the CHC LRN model modified taking into account equation (3). This new damping function takes into account a characteristic of pulp flow, the yield stress, and also the fibre characteristics, the fibre aspect ratio. The model proposed allowed a good description of the turbulent flow of the two types of fibres studied. The consideration of the presence of fibres in the lubrication layer had not significant impact on the numerical predictions. However, the CFD model under development can have a better physical meaning if the presence of fibres is included, since in reality a few fibres are always present near the wall.

Acknowledgements

The present work was developed under the projects PTDC/EQU-EQU/112388/2009 and Pest/C/EQB/UI0102/2013, financed by FCT/MCTES (PIDDAC) and co-financed by the European Regional Development Fund (ERDF) through the program COMPETE (POFC), and in close connection with the COST Action FP1005.

References

Bartosik, A. Application of rheological models in prediction of turbulent slurry flow. Flow, Turbulence and Combustion, Vol. 84, 277-293 (2010)

Bartosik, A. Simulation of the friction factor in a yield-stress slurry flow exhibits turbulence damping near the pipe wall. Journal of Theoretical and Applied Mechanics, Vol. 49, 283-300 (2011)

Blanco, A., Negro, C., Fuente, E. & Tijero, J. Rotor selection for a Searle-type device to study the rheology of paper pulp suspensions. Chemical Engineering and Processing, Vol. 46, 37-44 (2007)

Chang, K.C., Hsieh, W.D. & Chen, C.S. A modified low-Reynolds-number turbulence model applicable to recirculating flow in pipe expansion. Journal of Fluids Engineering, Vol. 117, 417-423 (1995)

Cotas, C., Asendrych, D. & Rasteiro, M.G. Numerical simulation of turbulent pulp flow: influence of the non-Newtonian properties of the pulp and of the damping function. In Proc. 8th International Conference for Conveying and Handling of Particulate Solids, Tel-Aviv, Israel, 3-7 May, 2015

Ventura, C., Blanco, A., Negro, C., Ferreira, P., Garcia, F. & Rasteiro, M. Modeling pulp fiber suspension rheology. TAPPI Journal, Vol. 6, 17-23 (2007)

Ventura, C., Garcia, F., Ferreira, P. & Rasteiro, M. Flow dynamics of pulp fiber suspensions. TAPPI Journal, Vol. 7, 20-26 (2008)

Ventura, C.A.F., Garcia, F.A.P., Ferreira, P.J., Rasteiro & M.G. Modeling the turbulent flow of pulp suspensions. Industrial & Engineering Chemistry Research, Vol. 50, 9735-9742 (2011)

Spheroids in wall turbulence: Part 1 Effect of mean shear

Lihao Zhao, Niranjan Reddy Challabotla, and Helge I. Andersson

Department of Energy and Process Engineering, Norwegian University of Science and Technology, Trondheim, Norway

Keywords: Non-spherical particles, turbulent channel flow, direct numerical simulation, mean shear

Abstract

The present work focused on suspensions of inertia-free spheroidal particles in a turbulent channel flow. Direct numerical simulations (DNSs) were performed for five different spheroidal aspect ratios λ = 0.01, 0.33, 1, 10, and 50. Effect of mean fluid shear on the tracer spheroids' orientation and rotational dynamics was investigated. The flattest disks preferentially aligned their symmetry axes normal to the wall whereas the longest rods were parallel with the wall. The aspherical tracers translated as a fluid element but did not adapt to the fluid vorticity due to its non-spherical shape. The results showed that the mean particle spin was reduced with increasing departure from sphericity.

Introduction

Understanding the dynamics of anisotropic particles in a turbulent carrier fluid over a solid wall is of fundamental interest and a key in making advances in many natural and industrial processes, as well as in bio-fluids applications: the dispersal of plant seeds with irregular shapes, pulp fibres in papermaking, suspensions of bio-mass particles in a combustion chamber, and the inhaled non-spherical particles in human respiratory system. The dynamics of particles with anisotropic shapes are commonly investigated by assuming regular axisymmetric shapes, i.e. either prolate (rod-like) or oblate (disk-like) spheroids. Spheroidal particles interact with wall turbulent flow in complex ways depending on various factors: near-wall shear, turbulence structure, and particle shape and inertia. Inertia-free spheroids with size smaller than the Kolmogorov length scale are expected to behave as tracers which passively follow the fluid motion, whereas the rotational motion does not necessarily adapt to the fluid vorticity. The dynamics of inertia-free spheroidal particles in homogenous isotropic turbulence has been subjected to several numerical studies (Pumir & Wilkinson 2011, Gustavsson et al. 2014) and also a few experimental investigations (Parsa et al. 2012, Marcus et al. 2014). It has been observed that disk-like particles tumble more than rod-like particles (Marcus et al. 2014). Rod-like particles preferentially align with the fluid vorticity vector and the vorticity component along the rod axis does not contribute to their tumbling. In contrast to the rod-like particles, disks align perpendicular to the fluid vorticity vector and this preferential orientation results in higher tumbling rates (Gustavsson et al. 2014).

The majority of previous studies of inertial spheroidal particles were focused on particle dynamics in turbulent channel flow. In particular, the dynamical behavior of inertial rod-like particles has been explored by means of DNS along with the Lagrangian point-particle methodology (Zhang et al. 2001, Mortensen et al. 2008, Zhao et al. 2014). The orientational and rotational dynamics of inertial disk-like particles in channel flow turbulence have only very recently been reported (Challlabotla et al. 2015a), whereas inertia-free spheroids in a turbulent channel flow were explored by Challlabotla et al. (2015b).

In this extended abstract, the focus is on the effect of mean shear on orientational and rotational dynamics of the inertia-free spheroids with five aspect ratios from 0.01 to 50 in the near-wall region. Inertia effects will be dealt with in Part 2.

Governing Equations and Numerical Method

We adopt an Eulerian-Lagrangian approach to study the dynamics of inertia-free spheroidal particles suspended in a fully-developed turbulent channel flow. The continuous fluid phase is governed by the incompressible Navier-Stokes equations which are intergrated numerically in a DNS approach with the same Navier-Stokes solver as in our earlier studies (Mortensen et al. 2008, Zhao et al. 2014)

$$\frac{\partial u_i}{\partial x_i} = 0, \qquad \frac{\partial u_i}{\partial t} + u_j \frac{\partial u_i}{\partial x_j} = -\frac{\partial p}{\partial x_i} + \frac{1}{Re_\tau}\frac{\partial^2 u_i}{\partial x_j \partial x_j}, \tag{1}$$

where u_i is the i^{th} component of the velocity vector and $Re_\tau = u_\tau h/\nu$ is the Reynolds number based on the wall friction velocity, u_τ, and on the channel half-height, h.

A general spheroidal particle is characterized by three semi-axes a = b ≠ c. The aspect ratio $\lambda = c/a$ distinguishes between prolate ($\lambda > 1$) and oblate ($\lambda < 1$) spheroids, whereas $\lambda = 1$ corresponds to an isotropic particle, i.e. a sphere. DNS of prolate spheroidal point-particles suspended in a turbulent channel flow was first performed by Zhang et

al. (2001), followed by Mortensen et al. (2008), Marchioli et al. (2010), and Zhao et al. (2014). Recently Challabotla et al. (2015a) extended the methodology to oblate spheroidal particles. Here, the same methodology is adopted to study the dynamics of tracer spheroidal point-particles in channel flow turbulence. The translational motion of the inertia-free spheroids is following the local fluid elements and the rotational motion adjusts such that the Jeffery-torques (Jeffery 1922) vanish exactly, i.e.

$$\begin{aligned} \omega_x' &= -\Lambda S_{yz}' + \Omega_x' \\ \omega_y' &= \Lambda S_{xz}' + \Omega_y' \\ \omega_z' &= \Omega_z'. \end{aligned} \qquad (2)$$

This set of equations demonstrate the coupling between the particle rotation vector ω_i' and fluid rotation vector Ω_i' and the fluid strain rate tensor S_{ij}'. The shape parameter $\Lambda = (\lambda^2 - 1)/(\lambda^2 + 1)$ is a measure of the degree of asphericity and $\Lambda = 0$ for spheres.

The frictional Reynolds number is $Re_\tau = 180$. All variables are normalized by viscous scales for velocity (u_τ), length (ν/u_τ), and time (ν/u_τ^2). The size of the computational domain is $12h \times 6h \times 2h$ in the streamwise, spanwise and wall-normal directions, respectively, and 192 grid points are used in each coordinate direction. The grid resolution in the streamwise and spanwise directions become $\Delta x^+ = 11.3$ and $\Delta y^+ = 5.6$, while the non-uniform grid spacing in the wall-normal direction varies from $\Delta z^+ = 0.9$ next to the walls to 2.86 in the channel center. The time intergration is performed with a constant time step $\Delta t^+ = 0.036$. Periodic boundary conditions are used in the two homogeneous directions and no-slip and impermeability conditions are imposed at the channel walls.

The suspension of non-inertial spheroids is assumed to be dilute and the particle size is smaller than the Kolmogorov length. These assumptions justify the one-way coupled simulation where the feedback from the spheroidal particles on the fluid phase is ignored as well as neglection of particle-particle collisions and the use of the Jeffery torques expressions used to derive equation (2). Particle-wall collisions are fully elastic so that a spheroid keeps its linear and angular momentum in the two homogeneous directions after a collision. Simulations of inertia-free spheroids (i.e. St = 0) are performed for five different particle shapes $\lambda = 0.01$, 0.33, 1, 10, and 50 all with semi-axis $a^+ = 0.36$. 500 000 spheroids of each shape are randomly injected into the same turbulence field at time $t = 0$. Orientational and rotational particle statistics are computed by averaging instantaneous data in time between $720\nu/u_\tau^2$ and $2520\nu/u_\tau^2$ and also in the homogeneous streamwise and spanwise directions.

Results and Discussion

The shape has a strong influence on particle orientation and the rotation dynamics, as illustrated by the instantaneous plots of spheroids with λ = 0.01 and 50 in Figure 1.

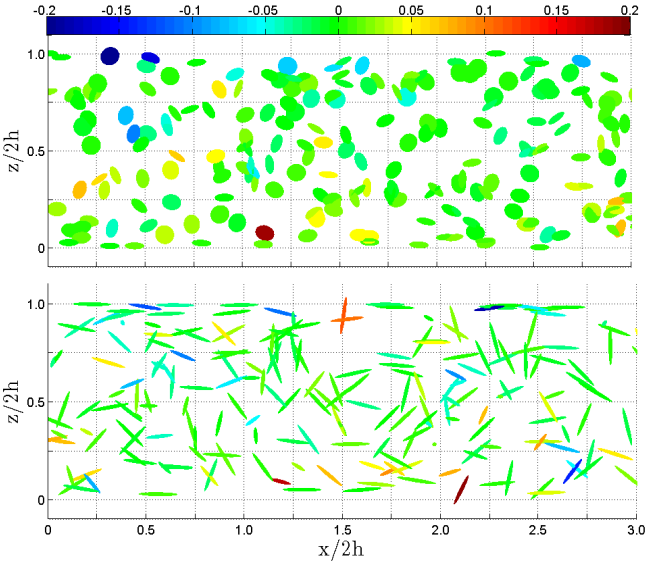

Figure 1: Instantaneous distribution of disk-like particles with aspect ratio λ = 0.01 and rod-like particles with λ = 50. The particles are projected into the (x, z)-plane and the shape reflects the particle orientation while colour-coding represents the particles spanwise angular velocity ω_y normalized by the viscous time scale.

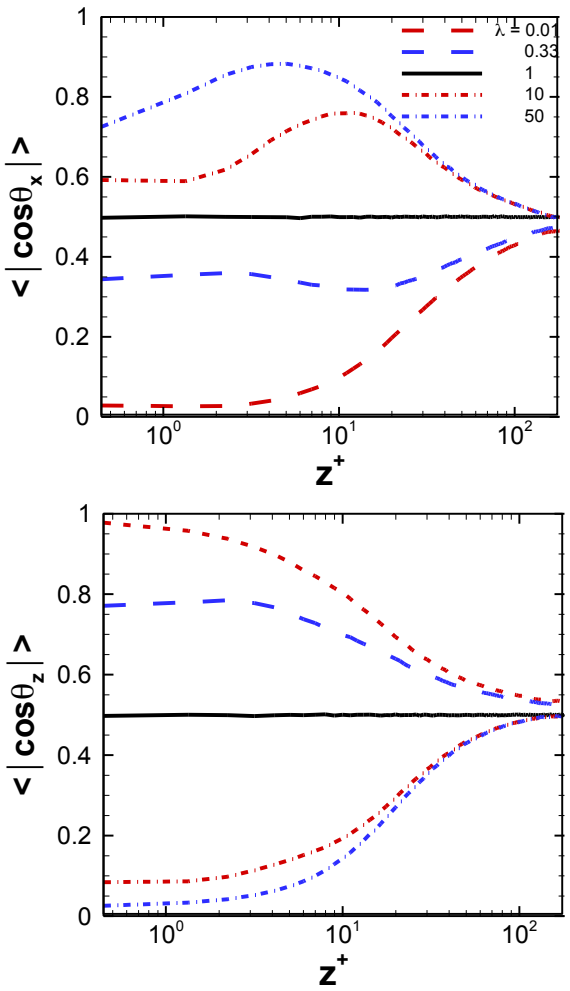

Figure 2: The mean absolute values of the direction cosines $<|\cos\theta_i|>$ for five different particle aspect ratios λ = 0.01 - 50. (a) streamwise direction, and (b) wall-normal direction.

The variations of the absolute values of the mean direction cosines from the wall to the channel center are shown in Figure 2 for the entire range of aspect ratios from λ = 0.01 to 50. θ_i is defined as the angle between the particle sysmmetry axis and the x_i-direction. It can be observed from Figure 2(a) that the preferred orientation of the spheroids varies monotonically from misalignment towards alignment in the streamwise direction as the aspect ratio λ increases from 0.01 to 50. The flattest spheroids (λ = 0.01) are preferentially orientated perpendicular to the flow direction whereas the longest spheroids with λ = 50 are preferentially aligned with the mean flow. Challabotla et al. (2015a) reported that inertial disks exhibited a strong preferential orientation in the spanwise direction, i.e. $|\cos\theta_y| \approx 1$, whereas the flattest disks (λ = 0.01) with only modest inertia (St = 1) surprisingly exhibited a strong preference for wall-normal orientation, i.e. in keeping with $|\cos\theta_z| \approx 1$ for the present inertia-free disks. In the core region of the channel, however, $|\cos\theta_x| \approx |\cos\theta_y| \approx |\cos\theta_z| \approx 0.5$ irrespective of particle shape. This suggests that both rods and disks orient themselves randomly in the almost isotropic vorticity field at the channel center (Andersson et al. 2015).

The strongly anisotropic fluid vorticity field in the near-wall region, in combination with the preferential particle orientations observed in Fig. 2, makes the rotational dynamics of the spheroidal particles crucially shape-dependent. The mean particle spin or angular velocity about the spanwise axis is shown in Figure 3, whereas the mean spin in the two other directions is zero. An exceptionally strong shape-effect on $<\omega_y>$ is seen in the vicinity of the walls, but this shape dependency gradually fades away outside of the buffer region, i.e. for $z^+ > 30$. The spherical particles rotates faster than any of the other particle shapes and the spinning of the inertia-free spheres inevitably matches the fluid spin. The mean spin decreases with increasing asphericity and the flattest disks (λ = 0.01) and the longest rods (λ = 50) rotate substantially slower than the spheres. This phenomenon can be attributed to their preferential orientations shown in Figure 2.

Conclusions

In this abstract, orientation and rotation statistics of inertia-free spherodial particles in wall-bounded turbulence have been reported. Five different spheroidal tracers were considered, ranging from oblate disk-like particles (λ = 0.01) to prolate rod-like particles with λ = 50. The flattest disks were strongly aligned in the wall-normal direction whereas the longest rods aligned themselves with the wall. The inertia-free particles were evenly distributed across the channel, but the shape-dependence of their preferred orientations carried over to their angular velocity or spin. The strong mean spanwise spin observed for spherical particles (λ = 1) decreased with increasing asphericity both for rod-like and disk-like spheroids.

Inertia effects are considered in Part 2 of this investigation.

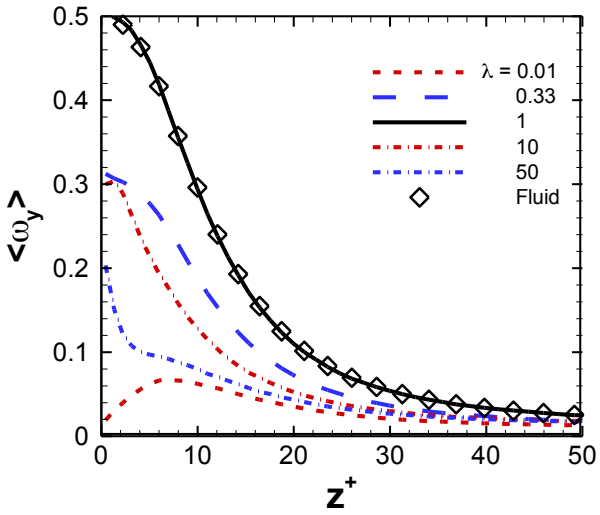

Figure 3: Mean particle angular velocity normalized by the viscous time scale.

Acknowledgements

This study has been supported by the Research Council of Norway through research fellowships to N.R.C. and L.Z. (project no 213917/F20 Turbulent Particle Suspensions) and grants of computing time (Programme for Supercomputing).

References

Andersson, H.I., Zhao, L. & Variano, E.A. On the anisotropic vorticity in turbulent channel flows, ASME J. Fluids Eng., Vol. 137, 084503 (2015).

Challabotla, N. R., Zhao, L. & Andersson, H. I. Orientation and rotation of inertial disk particles in wall turbulence. J. Fluid Mech. Vol. 766, R2 (2015a).

Challabotla, N. R., Zhao, L. & Andersson, H. I. Shape effects on dynamics of inertia-free spheroids in wall turbulence. Phys. Fluids, under review (2015b).

Gustavsson, K., Einarsson, J. & Mehlig, B. Tumbling of small axisymmetric particles in random and turbulent flows. Phys. Rev. Lett., Vol. 112, 014501(2014).

Jeffery, G. B. The motion of ellipsoidal particles immersed in a viscous fluid. Proc. R. Soc. Lond. A, Vol 102, 161-179 (1922).

Lundell, F., Södberg, L. D. & Alfredsson, P. H. Fluid mechanics of papermaking. Annu. Rev. Fluid Mech., Vol. 43, 195-217 (2011).

Marchioli, C., Fantoni, M. & Soldati, A. Orientation, distribution, and deposition of elongated, inertial fibers in turbulent channel flow. Phys. Fluids, Vol. 22, 033301 (2010).

Marcus, G. G., Parsa, S., Kramel, S., Ni, R. & Voth, G. A. Measurements of the solid-body rotation of anisotropic particles in 3D turbulence. New J. Phys., Vol. 16, 102001 (2014).

Mortensen, P. H., Andersson, H. I., Gillissen, J. J. J. & Boersma, B. J. Dynamics of prolate ellipsoidal particles in a turbulent channel flow. Phys. Fluids, Vol. 20, 093302 (2008).

Parsa, S., Calzavarini, E., Toschi, F. & Voth, G. A. Rotation rate of rods in turbulent fluid flow. Phys. Rev. Lett., Vol. 109 (13), 134501 (2012).

Pumir, A. & Wilkinson, M. Orientation statistics of small particles in turbulence. New J. Phys., Vol. 13, 093030 (2011).

Zhang, H., Ahmadi, G., Fan, F.-G. & McLaughlin, J. B. Ellipsoidal particles transport and deposition in turbulent channel flows. Int. J. Multiphase Flow, Vol. 27, 971-1009 (2001).

Zhao, L., Marchioli, C. & Andersson, H. I. Slip velocity of rigid fibers in turbulent channel flow. Phys. Fluids, Vol. 26, 063302 (2014).

Spheroids in wall turbulence: Part 2 Effect of inertia

Helge I. Andersson[1], Lihao Zhao[1], Niranjan Reddy Challabotla[1] and Evan Variano[2]

[1] *Department of Energy and Process Engineering, Norwegian University of Science and Technology, Trondheim, Norway*
[2]*Department of Civil and Environmental Engineering, University of California, Berkeley, Berkeley CA 74720*

Keywords: Non-spherical particles, turbulent channel flow, direct numerical simulation, mean shear

Abstract

Suspensions of inertial spheroidal particles in a turbulent channel flow have been studied by direct numerical simulations (DNSs) with an Eulerian-Lagrangian approach. The effect of particle inertia on particle rotational and orientational dynamics were investigated at the channel centre, where the vorticity field is nearly homogenous and isotropic (without mean shear). The statistical results showed that at the channel center oblate spheroids tend to rotate orthogonally to their symmetry axes whereas prolate particles rotate around their symmetry axes. This trend is attenuated with an increase of particle inertia, so that highly inertial spheroids rotate more isotropically about their principle axes. The weakened preferential rotation pattern was explained by examining alignment of their orientation relative to the fluid vorticity. Prolate spheroids tend to align their symmetry axis in the direction of the vorticity vector while oblate spheroids tend to align with their symmetry axis orthogonal to the fluid vorticity.

Introduction

Non-spherical particles suspended in turbulent flows is commonly encountered in engineering and environmental applications such as inhaled particles in human's lung, plankton dynamics in the ocean, combustion systems, and paper making, to name a few. Non-spherical particles react on turbulent flow structures in complex ways which depend both on particle shape and inertia. A bi-axial ellipsoid, i.e. a spheroid, is widely adopted to closely represent non-spherical particles and the shape of a spheroid is readily parameterized by the aspect ratio λ defined as the ratio between the symmetry axis and the two equal axes.

In the past decade, the dynamics of inertia-free spheroids in homogeneous isotropic turbulence (HIT) has been studied in various numerical (Pumir & Wilkinson 2011, Gustavsson et al. 2014) and also experimental investigations (Parsa et al. 2012, Marcus et al. 2014). It has been observed that disk-like particles tumble more than rod-like particles (Gustavsson et al. 2014, Marcus et al. 2014). Rod-like particles preferentially align with the fluid vorticity vector (Pumir & Wilkinson 2011, Marcus et al. 2014) and, in contrast, disks align perpendicular to the fluid vorticity vector, which results in higher tumbling rates (Gustavsson et al. 2014). The variance of the total rotation rate of a spheroidal particle is almost independent of the particle shape (Byron et al. 2015). Strong effects of particle shape on tumbling and spinning were reported for small deviations from spherical shape in the range of $0.1 < \lambda < 10$. The particle rotation rates turned out to be almost insensitive to changes in particle shape outside of this interval (Parsa et al. 2012).

Inertial spheroidal particles in decaying isotropic turbulence have been numerically investigated (Siewert et al. 2014), but the majority of studies that include inertial aspherical particles have been conducted in a turbulent channel flow (Zhang et al. 2001, Mortensen et al. 2008, Marchioli et al. 2010, Zhao et al. 2014) but primarily focused on particle clustering, turbophoresis, and particle motion.

In this extended abstract, the focus is on inertial effects on rotational and orientational dynamics of spheroids in the center region of the channel where the vorticity field is nearly homogeneous and isotropic (Andersson et al. 2015).

Governing Equations and Numerical Method

An Eulerian-Lagrangian approach is employed in present study of inertial spheroids in turbulent channel flow. The fluid phase is governed by the mass and momentum conservation equations:

$$\frac{\partial u_i}{\partial x_i} = 0, \qquad \frac{\partial u_i}{\partial t} + u_j \frac{\partial u_i}{\partial x_j} = -\frac{\partial p}{\partial x_i} + \frac{1}{Re_\tau} \frac{\partial^2 u_i}{\partial x_j \partial x_j}, \tag{1}$$

where u_i is the i^{th} component of the velocity vector and $Re_\tau = u_\tau h / \nu$ is the Reynolds number based on the wall frictional velocity, u_τ, and on the half channel height, h.

DNS of prolate spheroidal point-particles suspended in a turbulent channel flow was first performed by Zhang et al.

(2001), and recently Challabotla et al. (2015a, b) extended the methodology to oblate spheroidal particles. Here, the same methodology is again adopted to study the dynamics spheroidal point-particles in channel flow turbulence. The motion of spheroidal particles is described by using different Cartesian coordinate systems: the inertial frame, the particle frame, and the co-moving frame. The inertial frame, $\mathbf{x} =< x, y, z >$, spans the computational domain. The particle frame, $\mathbf{x'} =< x', y', z' >$, is attached to the particle with its origin at the particle mass-center and the coordinate axes are aligned with the principal directions of particle inertia.

The translational and rotational motions of an spheroid are governed by:

$$m\frac{dv_i}{dt} = F_i; \quad I_{ij}^{'}\frac{d\omega_j^{'}}{dt} + \acute{U}_{ijk}\omega_j^{'}I_{kl}^{'}\omega_l^{'} = N_i^{'} \qquad (2)$$

where ϵ_{ijk} is the Levi-Civita alternating or permutation tensor. The translational motion of a spheroid is governed by Newton's 2nd law of motion expressed in the inertial reference frame in which also the turbulent flow field is obtained. The rotational motion is governed by Euler's equation which is formulated in the particle frame. The hydrodynamic drag force F_i and torque N'_i acting on a spheroidal particle were derived by Brenner (1964) and Jeffery (1922), respectively.

The frictional Reynolds number is $Re_\tau = 180$. The size of the computational domain is $12h \times 6h \times 2h$ in the streamwise, spanwise and wall-normal directions, respectively, and 192 grid points are used in each direction. The grid resolution in the streamwise and spanwise directions become $\Delta x^+ = 11.3$ and $\Delta y^+ = 5.6$, while the non-uniform grid spacing in the wall-normal direction varies from $\Delta z^+ = 0.9$ next to the walls to 2.86 in the channel center. The time intergration is performed with a constant time step $\Delta t^+ = 0.036$. Periodic boundary conditions are used in the two homogeneous directions and no-slip and impermeability conditions are imposed at the channel walls. The suspension of the spheroids is assumed to be dilute and the particle size is smaller than the Kolmogorov length. These assumptions justify the one-way coupled simulation where the feedback from the spheroidal particles on the fluid phase is ignored as well as neglection of particle-particle collisions and the use of the Jeffery torques. Simulations of inertia-free spheroids (St = 0) and inertial spheroids (St = 30) are performed for different particle shapes λ = 0.01, 0.1, 0.33, 1, 3, 10, and 50 all with semi-axis $a^+ = 0.36$. 500 000 spheroids of each shape are randomly injected into the same turbulence field at time $t = 0$. Orientational and rotational particle statistics are computed by averaging instantaneous data in time between $5400\ \nu/u_\tau^2$ and $9000\ \nu/u_\tau^2$ and also in the homogeneous streamwise and spanwise directions. All statistics are averaged in time and over space in a rectangular box surrounding the channel center ($175 < z^+ < 185$).

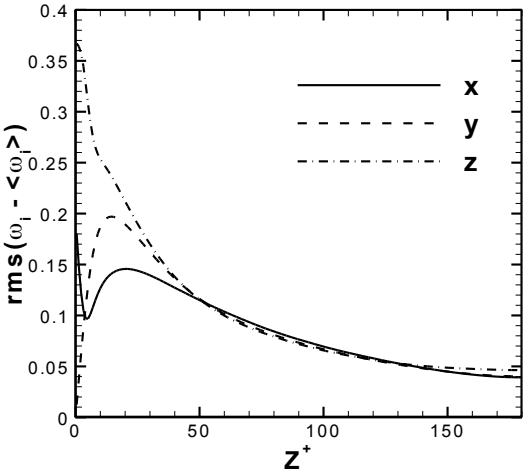

Figure 1: Root-mean-square fluid vorticity fluctuations (normalized by ν/u_τ^2) plotted against wall-distance z^+.

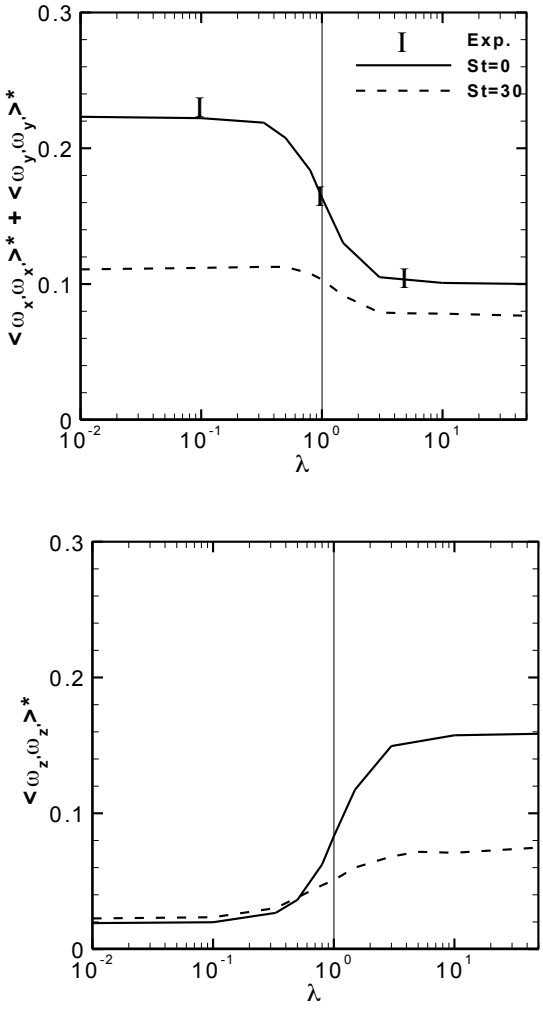

Figure 2: Channel-center results of (a) tumbling and (b) spinning components of enstrophy versus aspect ratio λ. Star quantities are normalized with Kolmogorov timescale τ_η. Symbols in (a) are laboratory data by Parsa et al. (2012) and Marcus et al. (2014).

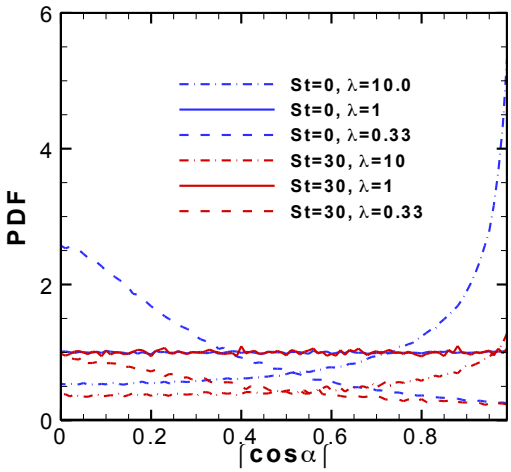

Figure 3: Channel-center distributions of the particles' alignment angle α with local fluid vorticity vector. Solid lines represent spherical particles, dashed lines are disk-like particles and dashed-dotted lines are rod-like particles.

Results and Discussion

The profiles in Figure 1 show that near the channel centerplane, the rms vorticity fluctuations are somewhat anisotropic and the fluctuations of spanwise vorticity have a greater magnitude than the two other directions. The Reynolds number effect on the anisotropy of the fluid vorticity field in the channel center has recently been examined by Andersson et al. (2015).

We observe from Fig. 2(a) that at the channel center for St = 0 oblate spheroids tumble more than prolate spheroids, consistently with the previous findings in HIT. The tumbling of disks and spinning of rods are reduced in Fig. 2(a, b). Inertia reduces the particle enstrophy and makes rotation more isotropic with respect to the particles' principle axes. The reduction in the spheroid's tendency to emphasize specific components of rotation can be explained by examining alignment of their orientation relative to the fluid vorticity (the inner product between a particle's orientation vector and fluid vorticity vector yields an angle α). Figure 3 shows that disks tend to align with their symmetry axis (z') orthogonal to the fluid vorticity. This alignment leads to strong tumbling and weak spinning (Marcus et al. 2014, Byron et al 2015). Rods show the opposite behavior, aligning parallel to the local vorticity, which enhances the particle spinning (Parsa et al. 2012, Gustavsson et al. 2014). For all shapes studied inertia weakens the alignment effect at the channel center, making rods less likely to emphasize spinning and disks less likely to emphasize tumbling. While inertia weakens the alignment tendencies, it does not eliminate them entirely, nor does it reverse them.

Conclusions

In the present abstract DNSs of suspensions of both prolate and oblate spheroids in a turbulent channel flow at Reynolds number $Re_\tau = 180$ were reported. The focus was on the inertial effects on the spheroids rotation about their non-symmetry axis (tumbling) and about their symmetry axis (spinning). Preferential alignment between the spheroid's orientation vector and the fluid voriticity vector was observed. Inertia-free spheroids with St = 0 behave in the same way at the center of the turbulent channel flow as in homogeneous isotropic turbulence (Marcus et al 2014). Particle inertia (St = 30) makes the particle rotation and alignment more isotropic, i.e. less dependent on the shape of the spheroids.

The effects of mean shear in the wall region are considered in Part 1 of this investigation.

Acknowledgements

This work has been supported by grants from the Peder Sather Center for Advanced Study at UC Berkeley and from the Research Council of Norway (Contract No. 213917/F20). The support by COST ACTION FP1005 is appreciated.

References

Andersson, H.I., Zhao, L. & Variano, E.A. On the anisotropic vorticity in turbulent channel flows, ASME J. Fluids Eng., Vol. 137, 084503 (2015).

Brenner, H. The Stokes resistance of an arbitrary particle – IV Arbitrary fields of flow, Chem. Eng. Sci., Vol. 19, 703-727 (1964).

Byron, M., Einarsson, J., Gustavsson, K., Voth, G., Mehlig, B. & Variano, E. Shape-dependence of particle rotation in isotropic turbulence. Phys. Fluids, Vol. 27, 035101 (2015).

Challabotla, N. R., Zhao, L. & Andersson, H. I. Orientation and rotation of inertial disk particles in wall turbulence. J. Fluid Mech. Vol. 766, R2 (2015a).

Challabotla, N. R., Zhao, L. & Andersson, H. I. Shape effects on dynamics of inertia-free spheroids in wall turbulence. Phys. Fluids, under review (2015b).

Gustavsson, K., Einarsson, J. & Mehlig, B. Tumbling of small axisymmetric particles in random and turbulent flows. Phys. Rev. Lett., Vol. 112, 014501(2014).

Jeffery, G. B. The motion of ellipsoidal particles immersed in a viscous fluid. Proc. R. Soc. Lond. A, Vol. 102, 161-179 (1922).

Lundell, F., Söderberg, L. D. & Alfredsson, P. H. Fluid mechanics of papermaking. Annu. Rev. Fluid Mech., Vol. 43, 195-217 (2011).

Marchioli, C., Fantoni, M., and Soldati, A. Orientation, distribution, and deposition of elongated, inertial fibers in turbulent channel flow. Phys. Fluids, Vol. 22, 033301 (2010).

Marcus, G. G., Parsa, S., Kramel, S., Ni, R. & Voth, G. A. Measurements of the solid-body rotation of anisotropic

particles in 3D turbulence. New J. Phys., Vol. 16, 102001 (2014).

Mortensen, P. H., Andersson, H. I., Gillissen, J. J. J. & Boersma, B. J. Dynamics of prolate ellipsoidal particles in a turbulent channel flow. Phys. Fluids, Vol. 20, 093302 (2008).

Ni, R., Ouellette, N. T. & Voth, G. A. Alignment of vorticity and rods with Lagrangian fluid stretching in turbulence. J. Fluid Mech. Vol. 743, R3 (2014).

Parsa, S., Calzavarini, E., Toschi, F. & Voth, G. A. Rotation rate of rods in turbulent fluid flow. Phys. Rev. Lett., Vol. 109 (13), 134501 (2012).

Pumir, A. & Wilkinson, M. Orientation statistics of small particles in turbulence. New J. Phys., Vol. 13, 093030 (2011).

Zhang, H., Ahmadi, G., Fan, F. G. & McLaughlin, J. B. Ellipsoidal particles transport and deposition in turbulent channel flows. Int. J. Multiphase Flow, Vol. 27, 971-1009 (2001).

Zhao, L., Marchioli, C., and Andersson, H. I. Slip velocity of rigid fibers in turbulent channel flow. Phys. Fluids, Vol. 26, 063302 (2014).

Hydrodynamic Torque of Finite Rotating Cylinder in Low Reynolds Number Flow

Jari T. Kolehmainen[1] and Dariusz Asendrych[2]

[1]*Department of Mechanical Engineering and Industrial Systems, Tampere University of Technology, Finland*
[2]*Institute of Thermal Machinery, Czestochowa University of Technology, Poland*

Keywords: cylinder, torque coefficient, rotating flow, Stokes flow, hydrodynamic torque, CFD

Abstract

Point-wise modelling of a particle immersed in fluid requires knowledge about the interaction of the particle with ambient fluid translation, shear and vorticity. The hydrodynamic information of such flow patterns is typically compressed in a coefficient. The aim of this paper is to investigate how cylindrical particle rotation translates into hydrodynamic torque. The hydrodynamic torque of the cylinder was computed using Ansys Fluent and then compared with the formula derived for the ellipsoid and Stokesian formula based on coefficients found by least squares fitting of Ansys Fluent data. The Stokes flow based model was found to be much more accurate than the formula derived for an ellipsoid in the low Reynolds range.

Introduction

Cylinders and ellipsoids are often used to model non-spherical particles due to their simplicity. Non-spherical particles are found in wide range of industrial applications ranging from pulp manufacturing to pharmaceutical processing.

Most multi-phase models treat particles as point-wise objects and relate the particle's hydrodynamic force and torque to ambient fluid velocity, vorticity, and shear-rate. The information regarding the object geometry is enclosed in various coefficients connected with different flow types.

For low Reynolds number flows around an ellipsoid there exists an analytical solution for force, torque, and stresslet (Kim & Karrila, 1991). There are also solutions for ellipsoids with finite Reynolds number such as of (O'Donnell & Helenbrook, 2005). Unfortunately, for cylinders the case is more complex and no general solution exists.

The drag and lift forces on a cylinder in translational flow with low to moderate Reynolds numbers have been studied in recent literature, for instance by (Vakil & Green, 2009) and (Mando & Rosendahl, 2010).

The hydrodynamic torque on a non-spherical particle can be caused by translational flow or by fluid vorticity or shear (Zastawny et. al., 2012). The torque of a particle is strongly related to its orientation that has strong effect on the rheological bulk viscosity (Kim & Karrila, 1991).

Currently, the torque models available in the literature for cylinders are either based on ellipsoid formulas with correction coefficients (Switzer, 2002) or on semi-analytical expressions that assume Stokes flow, infinite cylinder or other simplifications (Mando & Rosendahl, 2010).

This paper reports hydrodynamic torques of rotating cylinder with finite aspect ratio in low Reynolds number limit. It also discusses accuracy of the pre-existing models for predicting the torque.

Nomenclature

C_T	torque coefficient
d	cylinder's diameter [m]
D	elements of Stokesian matrix
Re	Reynolds number
T	torque [Nm]
Greek letters	
ω	angular velocity [rad/s]
λ	aspect ratio
ν	kinematic viscosity [m^2/s]
ρ	density [kg/m^3]

Theoretical Framework

In general, the hydrodynamic torque of a rotating non-spherical particle depends on the angular velocity in a non-linear manner. There are multiple ways to define Reynolds number for rotating non-spherical particles (see e.g. Mando & Rosendahl, 2010). In this paper, we will use the volume based diameter as done in (Zastawny et. al., 2012) since it allows for comparison within wide range of non-spherical particles. Hence the Reynolds number becomes:

$$Re = \frac{\omega^* \left(\sqrt[3]{3/2\lambda}\, d_p\right)^2}{\nu}, \quad (1)$$

where ω^* is characteristic angular velocity taken here as the norm of the total angular velocity, and

$$d_p = \sqrt[3]{3/2\,\lambda}\, d. \quad (2)$$

However, if the Reynolds number is sufficiently low the relationship between the torque and angular velocity may be

assumed as linear:

$$\begin{bmatrix} T_0 \\ T_1 \\ T_2 \end{bmatrix} = \begin{bmatrix} D_0 & 0 & 0 \\ 0 & D_1 & 0 \\ 0 & 0 & D_1 \end{bmatrix} \begin{bmatrix} \omega_0 \\ \omega_1 \\ \omega_2 \end{bmatrix}, \quad (3)$$

where the coordinate system is fixed on the cylinder's major and minor axes. The subscript 0 corresponds to the major axis and 1 to the minor one. If the Reynolds number increases the torque starts to depend on the square of angular velocity. For this reason it is customary to define the dimensionless torque coefficient as

$$C_{T,i} = \frac{T_i}{\rho d_p^5 \omega^* \omega_i} = \frac{D_i}{\rho d_p^5 \omega^*} \quad (4)$$

Simulation Method

In total 28 different cases were inspected. The cylinder angle to rotation axis was varied from 0 degrees to 90 degrees with 15-degree step. Furthermore, four different aspect ratios were considered, namely 5, 10, 15, and 20. The Reynolds number based on Eq. (1) was kept constant 0.1. This resulted in volume based diameter of 2.466mm and angular velocity of 0.01654/s.

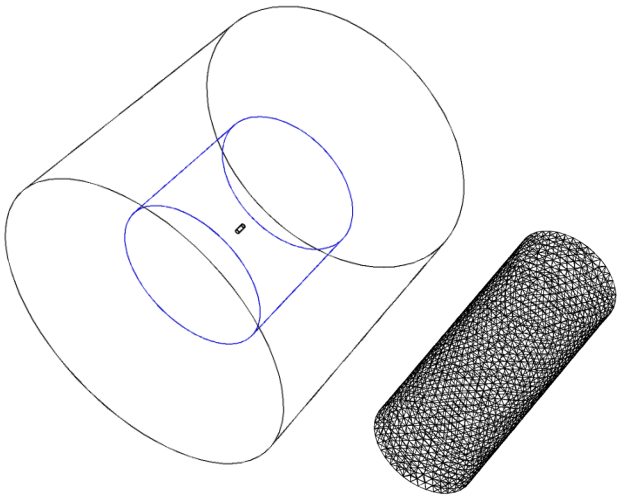

Figure 1: View of the computational domain (left) with the sliding mesh interface (blue lines) and the particle located in the centre. Magnified view of surface mesh on the cylinder (right).

The hydrodynamic torque on the particle was solved using Ansys Fluent 14.5. The cylinder was rotated using non-conformal sliding mesh interface. The whole domain (and the associated mesh) was decomposed into two cylinders, with the inner one surrounding the particle and rotating with the user defined angular velocity. The outer cylinder was still and it was bounded by cylindrical solid wall and symmetry boundary conditions enforced in both ends of the cylinder.

The mesh was generated by Ansys ICEM-CFD mesh generator and consisted of roughly 1,300,000 elements which varied slightly depending on the cylinder orientation angle. The sliding mesh interface was set far from the cylinder and refined to avoid unwanted interactions. Fig. 1 shows the computational domain and the mesh pattern at the particle's surface.

The solver was 1st order implicit transient solver. Pressure correction was done by PISO method with one correction, convective terms were discretized by 2nd order upwind scheme, and diffusive terms were discretized by 2nd order central difference scheme. The time was marched until the reported torque converged on the second decimal.

Results and Discussion

The results computed by Ansys Fluent were compared to corrected ellipsoid formula given in (Switzer, 2002) and to semi-analytical torque formula for cylinder presented in (Mando & Rosendahl, 2010).

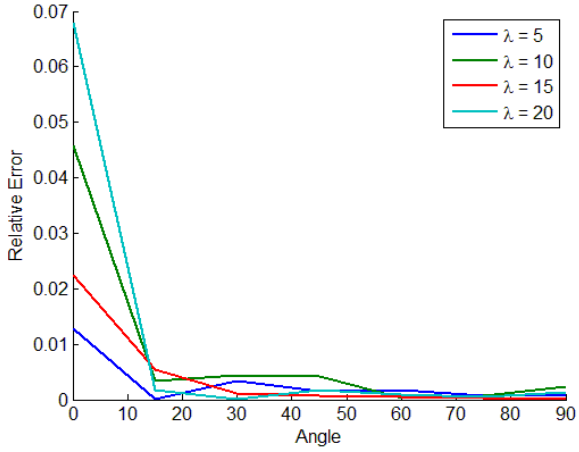

Figure 2: Relative error of the Stokesian model with various angles and aspect ratios.

The torque can be expressed in terms of the inclination angle and the elements of the Stokesian matrix Eq. (3). This leads to the following expression:

$$T_i = \omega^* [cos(\alpha_i)^2, sin(\alpha_i)^2][D_0, D_1]^T \quad (5)$$

where α_i stands for the inclination angle that is the angle between the cylinder major axis and the rotation axis. The torque in Eq. (5) is the torque with respect to the rotation axis. Zero inclination angle corresponded to the cylinder aligned with rotation axis. Using least squares fitting (LSF) to Eq. (5) allowed to compute Stokesian matrix elements from the exported torque. Eq. (5) was then recomputed using the LSF produced coefficients to see how well the torque predicted by the Stokesian model fits to the Ansys Fluent data. The results are shown in Fig. 2. As can be seen the model error is very small, but increasing as the aspect ratio increases. This is probably due to increasing tip velocity as the cylinder's length increases.

The respective torque coefficients for the minor and major axes are shown in Fig. 3. The major axis coefficient is decreasing with respect to aspect ratio while the minor axis coefficient is increasing. This is to be expected as the tip velocity grows larger with longer cylinders, and the boundary velocity decreases as the diameter decreases. The non-monotonic behaviour of major axis coefficient in Fig. 3 is probably an error caused by finite accuracy of the simulations. The maximum torque coefficient for major axis

torque was 0.452, and for minor axis it was 32.6. Hence the minor axis coefficient was found to larger three orders of magnitude than the major axis coefficient. They should reach the same magnitude for the aspect ratio approaching to unity.

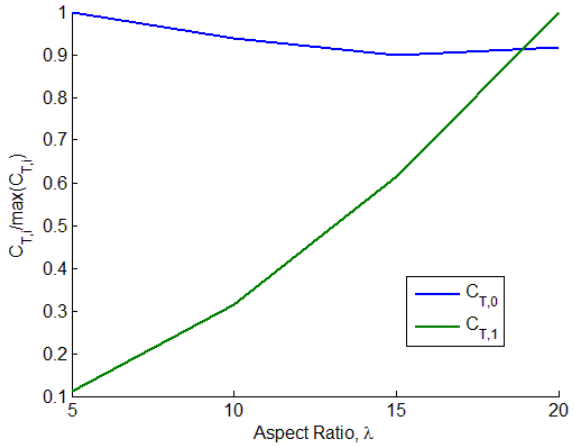

Figure 3: Scaled major and minor axes torque coefficients. The scaling factor coefficients were found to be 32.6 and 0.452 for the minor and the major axes, respectively.

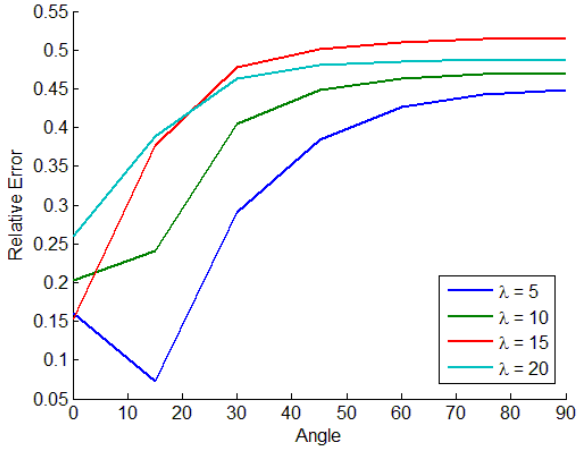

Figure 4: Relative error of corrected ellipsoid formula given in (Switzer, 2002).

The results were also compared to other models available in the literature. Sample comparison to (Switzer, 2002) formula for various aspect ratio values is shown in Fig. 4. The deviations from the own CFD data are growing along with the particle's inclination angle and they reach appr. 50% which can be considered as too large for most applications.

Conclusions

This work investigated hydrodynamic torque of rotating cylinder. The torque was determined by Ansys Fluent 14.5 and compared to corrected ellipsoid formulas based on analytical solution of Stokes flow available in source literature and to results predicted by LSF based Stokes flow.

The errors of corrected ellipsoid formula were up to 50% while the LSF based model led to much lower errors, not exceeding 7%. This would suggest that results based on the ellipsoid modelling would have significant errors.

Furthermore, quantitative torque coefficients were reported for the rotations along the minor and major axes. With this Reynolds number range simple Stokesian modelling resulted in fairly small errors as shown in Fig. 2, in particular for rotation around the minor axis.

Future work is needed to study the effect of the particle's aspect ratio allowing to derive the explicit formula for the torque coefficient. The qualitative behaviour with respect to aspect ratio would probably be similar to ellipsoids, but this was not investigated in this study. Extending the analysis for higher Reynolds numbers would also give invaluable insight into hydrodynamic torque beyond the Stokesian flow regime being especially important from the viewpoint of practical applications.

Acknowledgements

Authors would like to thank COST Action FP-1005 for funding an STSM of Dr. J. Kolehmainen and making this research possible.

References

Kim S. & Karrila S., Microhydrodynamics: principles and selected applications. Dover (1991)

Mando M. & Rosendahl L., On the motion of non-spherical particles at high Reynolds number. Powder Technology, Vol. 202, 1-13 (2010)

O'Donnell B. & Helenbrook B., Drag on ellipsoids at finite Reynolds numbers. Atomization and Sprays. Vol. 15, 363-376 (2005)

Switzer L., Simulating system of flexible fibers. PhD Dissertation, University of Wisconsin-Madison (2002)

Vakil A., Green S., Drag and lift coefficients of inclined finite circular cylinders at moderate Reynolds numbers. Computers and Fluids, Vol. 38, 1771-1781 (2009)

Zastawny M., Mallouppas G., Zhao F., van Wachem B., Derivation of drag and lift force and torque coefficients for non-spherical particles in flows. International Journal of Multiphase Flows, Vol. 39, 227-239 (2012)

On the validity of Jeffery moments for elongated particles in turbulent channel flow

Jure Ravnik[1], Cristian Marchioli[2], Alfredo Soldati[2]

[1]*Faculty of Mechanical Engineering, University of Maribor, Smetanova 17, SI-2000 Maribor, Slovenia*
[2]*Faculty of Mechanical Engineering, University of Udine, via delle scienze 208, 33100, Udine, Italy*

Keywords: particle tracking, fibre, prolate ellipsoid, velocity gradient tensor, Jeffery moments

Abstract

Many multiphase flow studies are based on the Lagrange-Euler numerical simulations of motion of particles in a turbulent fluid flow. The governing equations, which are used by most researchers, are based on a linear approximation of the flow velocity around the particle's centre. Only the particle centre is tracked and the motion is based on the flow velocity and velocity gradient estimated at the position of the particle centre. In this paper we examine the validity of such an approach for elongated particles - fibres. We find that, when the fibre size exceeds the Kolmogorov length scale of the turbulent flow, the error associated with the linear approximation of the flow around the fibre and the subsequent error in the calculation of forces and moments acting on the fibre is non-negligible and grows exponentially with fibre size. Statistics of this error for the motion of fibres in a DNS of a fully developed turbulent channel flow in terms of fibre size, orientation and position are presented in the paper. Fibres with different inertia (Stokes numbers 1 to 25) and size (from 0.1 to 36 Kolmogorov length scales) are considered. The results show an exponential increase of the error up to fibre length of five Kolmogorov length scales, after which, a plateau is reached. The error associated with fibres having the same size as the Kolmogorov length scale is about 1%.

Nomenclature

u	Flow velocity
a^+	length of the minor semi-axis of an ellipsoid
St	Stokes number

Greek letters

η_k	Kolmogorov length scale
λ	Fiber length versus width ratio

Introduction

Many Euler-Lagrange type simulations of particle laden flows consider particles to be pointwise and extrapolate forces on the particles based on the flow at the location of the centre of the particles.

The kinematics of motion was considered by Fan and Ahmadi (1995) by writing the equation for translational displacement of the fibre. The orientation of the fibre is described by the four Euler parameters. Their evolution through time is related to the angular velocity. The rotational motion of a non-spherical fibre moving in a flow field is governed by the Jeffery (1992) moments. Dynamics of translational motion is taken into account by the equation of motion for small rigid spheres proposed by Maxey and Riley (1983), while Brenner (1963) developed the drag expression for arbitrary fibres.

Usually, the fibre equations of motion are derived based on the assumption that the fluid field around the centre of mass of the fibre varies linearly in space. In other words, this means that the velocity gradient tensor should be constant in space in an area that is larger than the fibre (Jeffery (1922)). In a turbulent flow field, the size of the smallest scales is defined by the Kolmogorov length scale η_k. For the turbulent channel, the Kolmogorov length scale varies from 2 close to the wall to 4 in the centre of the channel. In the following analysis, we used $\eta_k = 2$. to provide conservative estimates.

For fibres shorter than the Kolmogorov length scale, we expect the Jeffery assumption to be valid. These fibres are smaller than the turbulent structures, thus we can expect the flow field to vary linearly in space around the fibre. On the other hand, the validity of Jeffery's assumption is not clear for larger fibres. In the following, we will provide an answer to the question exactly how large can the fibres be as compared to the Kolmogorov length scale, for the Jeffery's assumptions to hold.

In order to estimate the changes of the flow field in the area around the fibre, we sample the flow field at several locations along the long axis of a fibre. Figure 1 shows the distribution of velocity gradients along a couple of fibres. Looking at the small fibres (prolate ellipsoids) with length over Kolmogorov length ratio of $2a^+\lambda/\eta_k = 0.1$ we observe that the velocity gradient components are indeed constant along the fibre. This means that the velocity field around the fibre varies linearly and it can indeed be approximated using a Taylor series around the fibre's centre. In the case of large fibres, those having $2a^+\lambda/\eta_k > 10$, we observe large variations of the velocity gradient components indicating that the velocity flow field around the fibre changes non-linearly, as the fiber spans several turbulent

structures. It can be also observed that the fibre orientation also plays significant role. Comparing the velocity gradient distribution in the case of a fibre oriented in a wall normal direction versus the fibre oriented into a streamwise direction, we observe larger scattering of values in the case of wall normal orientation. This is caused by the properties of turbulent channel flow, which features larger velocity gradient changes in the wall normal direction.

In order to find a quantitative measure for changes along the fibre, we ran simulations and calculated statistics. Averaging over many fibres and many time steps, we measure the following

- change of components of the velocity gradient tensor along the fibre
- change in the calculation of Jeffrey moments

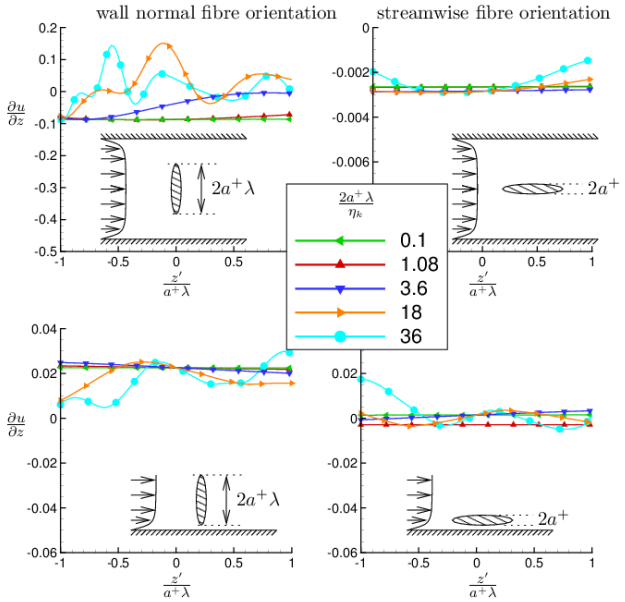

Figure 1: Profiles of the instantaneous velocity gradient component along the length of fibre are shown for various fibre lengths. Fibres were inserted into the centre of the channel (top row) and close to the wall (bottom row) oriented into streamwise (right panels) and wall normal (left panels) directions.

Flow database

To produce statistics presented in this paper we tracked fibers using DNS flow results. In the DNS database there are results of a Poiseuille flow of an incompressible, isothermal and Newtonian fluid in a plane channel at friction Reynolds number 150. The corresponding bulk Reynolds number is 2250. The DNS was performed by a pseudo-spectral flow solver as described by Soldati and Marchioli (2009, 2010, 2013). Periodic boundary conditions were imposed in streamwise and spanwise direction and no-slip boundary conditions were imposed at the two walls. Time integration is done using second-order Adams-Bashforth scheme for the non-linear terms, which are calculated in a pseudo-spectral way with de-aliasing in the periodic directions and an implicit Crank-Nicolson scheme for the viscous terms. The domain is discretizised by 128x128x129 nodes.

Results

We randomly inserted 100.000 fibres into the flow. Initially the fibre velocity was equal to the fluid velocity at the position of the fibre. Before the start of gathering data for statistics, we ran the simulation for 2000 time steps. This is longer than ten fibre characteristic time scales so the fibres had ample time to adopt to the flow field and the initial conditions have no influence of the statistics. After this period, statistics were gathered for 6666 time steps. The tracking was based on the work by Ravnik and Hriberšek (2013).

We chose 11 points along the fibre, where the velocity gradients were evaluated. In order to sample a wide range of ratios of fibre length versus the Kolmogorov length scale, we chose five fibres. Furthermore, we changed the fibre density, to change the fibre inertia to St=1, 5, 25.

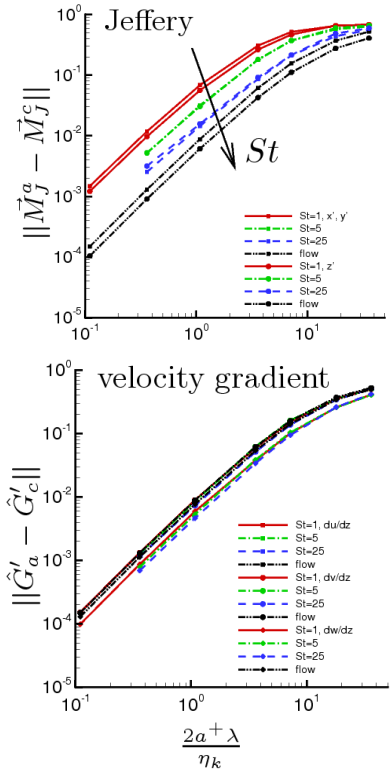

Figure 2: Relative RMS versus the ratio between fibre length and Kolmogorov length scale. Top panel: Jeffery moments, bottom panel: velocity gradient components. Statistics denoted by "flow" were obtained by randomly sampling the flow field.

The relative RMS of individual components of the velocity gradient tensor for different fibres is shown in the bottom right panel of Figure 2. We observe an increase in the RMS with fibre length. This can be explained by the fact that longer fibres sample larger portions of the flow field and as their length increases over the Kolmogorov length scale,

they span over the smallest turbulent structures and reach regions of significantly different flow conditions. When the fibre length is equal to the Kolmogorov length scale, the relative RMS is less than 1%, thus such error is expected in fibre tracking. Individual components of the tensor yield RMS difference of the same order of magnitude. The largest RMS is found at the du/dz components, which is expected, as the greatest velocity field variation is found along the long semi-axis of the ellipsoid.

The top panel of Figure 2 shows the difference between Jeffery moments calculated by the velocity gradient tensor averaged along the fibre and the Jeffery moments calculated using velocity gradients at the centre of the fibre. The difference increases with increasing fibre length reaching a plateau for very long fibres. Larger fibers sample regions of flow where velocity gradients change significantly and thus assumptions of constant velocity gradients of Jeffery is violated. Fibres with low inertia are able to follow the flow structures and thus sample regions of the flow field, where changes of velocity gradients is substantial. In consequence we observe a large difference in the calculation of Jeffrey moments. As inertia increases, the fibres move more and more independently of the smaller flow structures, and the approximation of Jeffrey moments is better. The most accurate Jeffery moments are obtained when only randomly sampling the flow field.

Conclusions

We have shown that when the length of elongated particles - fibres - is longer than the Kolmogorov length scale of turbulence, the flow along the fibres changes significantly and cannot be approximated by extrapolation from the values at the centre of the fibres. The Jeffery moments were derived under the assumption that the velocity gradient tensor is constant in space in an area that is larger than the fibre. We have shown that this assumption is violated when the fibre length is larger than the Kolmogorov length scale. The statistics show an exponential increase of the error with fibre length. The error is less than 1% for fibers, which have a length equal to the Kolmogorov length scale. The error is smaller for high inertia fibres and larger for low inertia fibres. In turbulent channel flow fiber orientation is important only for fibres smaller than the Kolmogorov length scale. The error is smaller when fibers are oriented into the streamwise direction. When comparing fibres at difference distances from the wall, we observed no difference for low inertia fibres. High inertia fibers exhibit smaller error when they are located very close to the wall and when they are close to the centre of the channel.

Acknowledgements

J.R. would like to thank COST Action FR1005 for funding short term scientific missions at the University of Udine, where work presented at this conference was performed.

References

Brenner, H. The Stokes resistance of an arbitrary particle, Chem. Eng. Sci, Vol 18:1--25, (1963).

Fan F. and Ahmadi G. A sublayer model for wall deposition of ellipsoidal particles in turbulent streams, J. Aerosol Sci., Vol 26, 813-840, (1995).

Gallily I. and Cohen. A.-H. On the orderly nature of the motion of nonspherical aerosol particles II. Inertial collision between a spherical large droplet and axially symmetrical elongated particle, J. Colloid Interface Sci., Vol 68, 338-356, (1979).

Jeffery, G.B The motion of ellipsoidal particles immersed in a viscous fluid, Proc. R. Soc. A, Vol 102, 161-179, (1922).

Marchioli C., Fantoni M., and Soldati A. Orientation, distribution and deposition of elongated, inertial fibers in turbulent channel flow, Phys. Fluids, Vol 49:033301, (2010).

Marchioli C. and Soldati A. Rotation statistics in wall shear turbulence, Acta Mechanica, Vol 224:2311--2329, (2013).

Maxey M.R. and Riley J.J. Equation of motion for a small rigid sphere in a nonuniform flow. Phys. Fluids, Vol 26:883-889, (1983).

Ravnik J. and Hriberšek M. High gradient magnetic particle separation in viscous flows by 3D BEM, Comput Mech, Vol 51:465-474, (2013).

Shapiro M. and Goldenberg M., Deposition of glass fiber particles from turbulent air flow in a pipe, J. Aerosol Sci., Vol 24:65--87, (1993).

Soldati A. and Marchioli C., Physics and modelling of turbulent particle deposition and entrainment: Review of a systematics study, Int. J. Multiphase Flow, Vol 35, 827-839, (2009).

Dispersion of rigid fibers in turbulent channel flow

Cristian Marchioli[1], Alfredo Soldati[1]

[2]*Faculty of Mechanical Engineering, University of Udine, via delle scienze 208, 33100, Udine, Italy*

Keywords: Wall turbulence, rigid fibers, rotation statistics, direct numerical simulation, Lagrangian tracking

Abstract

We examine the effect of local shear and turbulence anisotropy on the rotation of elongated rigid fibers. To this aim, statistics of the fiber angular velocity, Ω, are extracted from direct numerical simulation of turbulence coupled with Lagrangian fiber tracking. We show that elongation is important for fibers with small inertia (St ≤ 5 in our flow-fiber combination), and that, in the strong shear region near the wall, fiber anisotropy adds to flow anisotropy to induce strong deviations on fiber rotation with respect to spherical particles.

Nomenclature

u	Flow velocity
a^+	length of the minor semi-axis of an ellipsoid
St	Stokes number

Greek letters

η_k	Kolmogorov length scale
λ	Fiber length versus width ratio

Introduction

A possible approach for modelling rotation of fibers in turbulence is to describe the time evolution of fiber angular velocity as a stochastic (random walk) process in orientation space [1]: In analogy with the translational motion of tracers and particles in Homogeneous Isotropic Turbulence (HIT), one can hypothesize that the Lagrangian time series of angular velocity are characterized by a Gaussian probability distribution with Markovian properties. Based on this hypothesis, fiber rotation can be described within the theory of diffusion as a Ornstein-Uhlenbeck (OU) process [2], which is completely characterized by a statistically-stationary Gaussian distribution and auto-covariance which takes the specific form of a negative exponential. This modelling approach assumes that both translational diffusion and rotational diffusion are homogeneous and isotropic. This assumption was proven acceptable for unbounded flows where dispersion is in- deed stationary and Gaussian [3, 4, 5], and may be partly ex- tended also to wall-bounded shear flows [6, 7], where Lagrangian velocity autocorrelations exhibit exponential decay if particles are not sampling near-wall regions of high turbulence anisotropy. All these studies, however, are concerned with spherical particles. Much less effort has been devoted to exploring the applicability of standard diffusion laws to non-spherical particles, as in the case of fibers: Previous modelling attempts focus on HIT [1, 8, 9], and thus neglect effects due to turbulence anisotropy. Recent studies [9, 10], however, show that orientation of elongated fibers is correlated with local velocity gradients and that the strength of this correlation is heavily influenced by fiber shape. These findings suggest that anisotropy of fibers adds to anisotropy of turbulence to deviate fiber behavior (in particular, rotation rates) from that predicted by stationary Gaussian dispersion models. In this work, we examine the effect of local shear and flow anisotropy on the rotational dynamics of fibers with different elongation and inertia. This analysis is exploited to assess the extent to which diffusion laws can be applied to describe fiber rotational dispersion in wall-bounded turbulence. More specifically, we are interested in assessing the possibility of modelling rotation as an OU pro- cess depending both on flow parameters (shear, anisotropy) and on fiber parameters (inertia, elongation).

Physical Problem and Numerical Methodology

The reference flow configuration is Poiseuille flow of incompressible, isothermal and Newtonian fluid in a plane channel at friction Reynolds number $Re_\tau = u_\tau h/\nu = 150$, with u_τ the friction velocity, ν is fluid viscosity and h is the channel half-height. We performed pseudo-spectral DNS, imposing periodic boundary conditions in the streamwise (x) and spanwise (y) directions and no-slip conditions at the walls. Time integration a 2nd-order Adams-Bashforth scheme for the non-linear terms and an implicit Crank-Nicolson scheme for the viscous terms. The channel size is 1885 × 942 × 300 wall units (identified with the superscript "+" and obtained using ν and u_τ) in x, y and z, discretized with 128 × 128 × 129 nodes.

Lagrangian fiber dynamics is treated as in [11]. The translational equation of motion of an individual fiber is given by the linear momentum equation $d\boldsymbol{u}_p/dt=\boldsymbol{F}/m$, where $\boldsymbol{u}_p$ is fiber velocity, $\boldsymbol{F}=\mu\boldsymbol{K}(\boldsymbol{u}_{@p}-\boldsymbol{u}_p)$, with μ the fluid dynamic viscosity, K the resistance tensor and $\boldsymbol{u}_{@p}$ the fluid velocity at fiber position, is the total hydrodynamic drag force acting on the fiber (strictly valid for an ellipsoid under

creeping flow conditions) and $m = 4\pi a^3 \lambda \rho_p/3$ is fiber mass with a the semi-minor axis, λ the aspect ratio of the ellipsoid, and ρ_p is fiber density. The resistance tensor $\boldsymbol{K}$ is expressed in the Eulerian frame of reference, $\boldsymbol{x} =< x, y, z >$. Two other Cartesian coordinate systems, both with origin at the fiber center of mass, are used to describe fiber motion: a Lagrangian frame of reference, $\boldsymbol{x'}$, and a co-moving frame of reference, $\boldsymbol{x'}$, with axes parallel to the inertial frame. The rotational motion of the fiber is governed by the following equation: $d(\boldsymbol{I}\cdot \Omega')/dt + \Omega' \times (\boldsymbol{I}\cdot \Omega') = \boldsymbol{N}'$, where Ω is fiber angular velocity, $\boldsymbol{I}$ is the moment of inertia tensor and $\boldsymbol{N}$ the torque acting on the fiber. The equations of fiber motion are solved using a mixed explicit/implicit differencing procedure [12]. The total tracking time in wall units is $t^+ = 3500$, with time step size equal to that of the fluid: 0.03 in wall units. The main simulation parameters are a, and the fiber response time [13]:

$$St = \frac{2(a^+)^2 \rho_p}{9\rho} \frac{\lambda \ln(\lambda + \sqrt{2-1})}{\sqrt{\lambda^2 - 1}} .$$

In this study, we have selected: $a^+ = 0.36$, $\lambda = 1$ (spherical particles), *3, 10, 50*, and $St = 1, 5, 30, 100$. To ensure converged statistics, swarms of *200,000* fibers are tracked for each particle category, assuming dilute flow and one-way coupling.

Results and Discussion

Rotation statistics are computed for three distinct sub-regions of the channel: viscous sub-layer ($0 < z^+ < 5$ with z^+ the distance from the wall), buffer layer ($5 < z^+ < 50$), and log layer ($50 < z^+ < Re_\tau$). These sub-regions exhibit significantly different shear stress and dissipative flow scales, and may thus produce different fiber rotational dynamics.

Angular velocity statistics

The non-dimensional ensemble-averaged fiber angular velocity is shown in Fig. 1. Only the spanwise component $\langle\Omega_y\rangle$ is shown since $\langle\Omega_x\rangle$ and $\langle\Omega_z\rangle$ are always zero. Profiles highlight the effect of fiber elongation on $\langle\Omega_y\rangle$ for a specific value of *St*. Results for tracer particles ($St = 0$), are also shown (thick solid line).

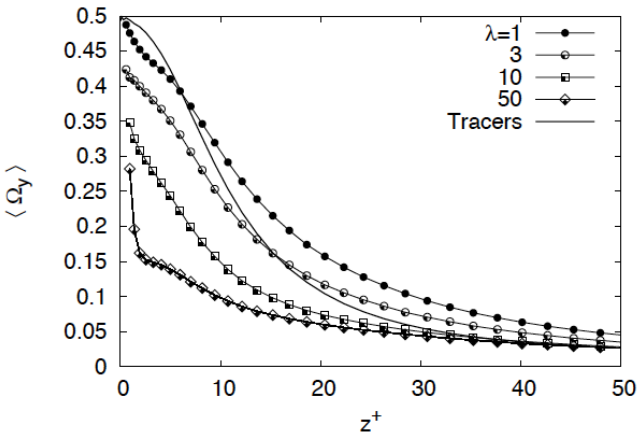

Figure 1: Fiber spanwise angular velocity, $\langle\Omega_y\rangle$, inside the buffer layer ($z^+ < 50$) for fibers with $St = 5$.

Regardless of inertia and shape, values of $\langle\Omega_y\rangle$ are much higher near the wall, where accumulation of the dispersed phase is known to occur [11], than outside of the buffer layer ($z^+ > 50$), where elongation does not seem to alter the expectation value of fiber rotational dynamics significantly. Elongation is important in determining the near-wall behavior of $\langle\Omega_y\rangle$, which decreases as fiber length increases. This implies that fibers spin slower than spherical particles, a consequence of fiber alignment in the longitudinal x − z plane [11]. We also find that shape effects are evident for all values of the aspect ratio λ at small Stokes numbers (St = 5) whereas longer fibers (λ ≥ 10 in the present case) are required to induce significant reduction of $\langle\Omega_y\rangle$ at large Stokes numbers (not shown).

Statistics of rotational turbulent diffusivity

Rotational turbulent diffusivity, normalized here by the angular velocity variance to allow direct comparison among different fiber families, is computed as:

$\Gamma_\Omega(\tau) = \int_0^\tau R_{\Omega_i,\Omega_i}(t)\mathrm{d}t$

where $R_{\Omega i,\Omega i}(\tau)$ is the autocorrelation coefficient of fiber angular velocity, computed in the inertial frame. Our aim is to verify if and under which conditions (degree of shear and turbulence anisotropy, fiber inertia and fiber elongation) the Lagrangian autocorrelation can be approximated as a decaying exponential: $R_{\Omega i,\Omega i}(\tau)=exp(-\tau/T^{ii}_L)$, where $T^{ii}_L = \int_0^\infty R_{\Omega_i,\Omega_i}(\tau)\mathrm{d}\tau$ is the Lagrangian integral timescale of the fiber angular velocity. This quantity provides the simplest measure of the time span over which fiber orientation is self-correlated. This implies an exponential increase of the rotational diffusivity according to the relation:

$$\Gamma_{\Omega_i}(\tau) = T^{ii}_L \left(1 - e^{-\frac{\tau}{T^{ii}_L}}\right).$$

When the exponential term drops to zero for $\tau >> T^{ii}_L$, $\Gamma_{\Omega i}(\tau)$ tends towards a constant value (known as the Fickian asymptote), which is equal to the Lagrangian integral timescale.

In Fig. 2 we compare the time evolution of $\Gamma_{\Omega i}(\tau)$ computed from our DNS+LPT database with the corresponding prediction. Statistical convergence of the numerical results was obtained by ensemble averaging over at least 10^4 trajectories. The agreement in the log region (Fig. 2a) is excellent, even at short times. At longer times, $\Gamma_{\Omega i}(\tau)$ curves recover the Fickian asymptote, confirming that fiber rotation in the channel center is homogeneous and angular velocities have a Gaussian distribution that can be modelled as an OU process. Spherical particles exhibit the highest rotational diffusivity, which decreases monotonically up to $St = 30$ and then increases for larger values of *St*. As expected, deviations become larger in the viscous sublayer (Fig. 2b) where theoretical predictions generally fail, with the exception of short fibers with $L^+/\tau_K^+ \sim O(1)$ and with small inertia. Fiber rotation is strongly non-homogeneous and it may be speculated that angular velocities have a non-Gaussian distribution due to strong shear, high turbulence anisotropy and velocity gradients that are not δ-correlated [10].

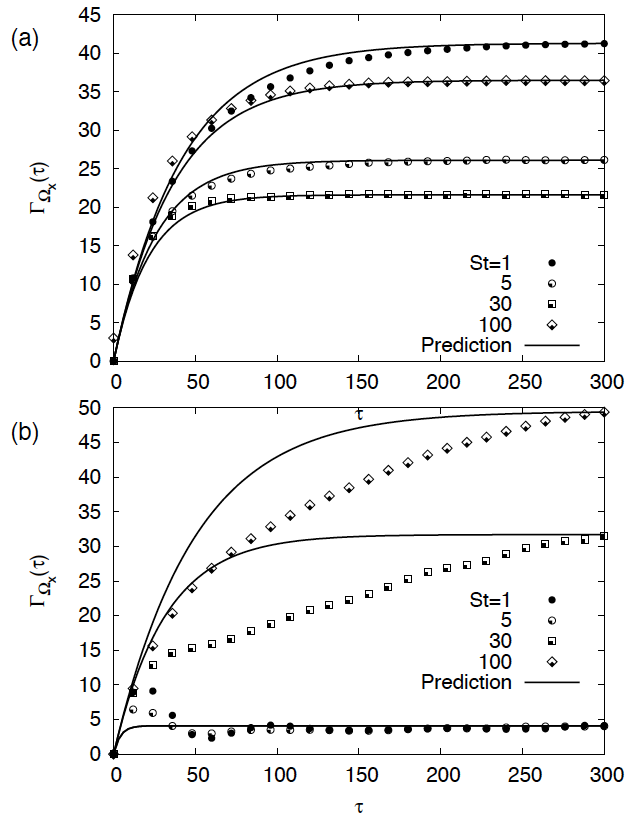

Figure 2: Streamwise rotational diffusivity, $\Gamma_{\Omega y}(\tau)$, in the log layer (a) and in the viscous sublayer (b).

Acknowledgements

The Authors would like to thank COST Action FR1005.

References

[1] C.R. Meyer and E. Variano, *arXiv:1301.0150*, 2012.

[2] V. Bezuglyy, B. Mehlig, M. Wilkinson, K. Nakamura, E. Arvedson *J. Math. Phys*., **47**, 073301 (2006).

[3] N. Mordant, P. Metz, O. Michel, and J.-F. Pinton, *Phys. Rev. Lett*. **87**, 214501 (2001).

[4] G. A. Voth, A. La Porta, A. M. Crawford, J. Alexander, and E. Bodenschatz, *J. Fluid Mech*. **469**, 121 (2002).

[5] P.K. Yeung, *Ann. Rev. Fluid Mech*., **34,** 115-142 (2002).

[6] J. Choi, K. Yeo and C. Lee, *Phys. Fluids*, **16**, 779-793 (2004).

[7] Q. Wang, K.D. Squires and X. Wu, *Atmosph. Env*., **29**, 2417-2427 (1995).

[8] J.A. Olson and R.J. Kerekes, J. Fluid Mech., **377**, 47-64 (1998).

[9] M. Shin and D.L. Koch*, J. Fluid Mech*., **540**, 143-173 (2005).

[10] S. Parsa, E. Calzavarini, F. Toschi, G.A. Voth, *Phys. Rev. Lett.*, **109**, 134501 (2012).

[11] C. Marchioli, M. Fantoni, A. Soldati *Phys. Fluids*, **22**, 033301 (2010).

[12] F.G. Fan, G. Ahmadi, *J. Aerosol Sci*., **26**, 813-840 (1995).

[13] M. Shapiro, M. Goldenberg, *J. Aerosol Sci*., **24**, 65-87 (1993).

Collisions of polydisperse spheroids settling in turbulence

Christoph Siewert[1*], Rudie P.J. Kunnen[2], Wolfgang Schröder[1]

[1]*Institute of Aerodynamics, Department of Mechanical Engineering, RWTH Aachen University, Wüllnerstr. 5a, 52062 Aachen, Germany*
[2]*Fluid Dynamics Laboratory, Department of Applied Physics, Eindhoven University of Technology, P.O. Box 513, 5600 MB Eindhoven, The Netherlands*

[*]*Corresponding author (c.siewert@aia.rwth-aachen.de) currently at: Lab. Lagrange, Université de Nice Sophia-Antipolis, CNRS, OCA, Nice, France*

Keywords: Isotropic turbulence; Particle-laden flows; Ellipsoidal collisions; Direct numerical simulation

Abstract

Collisions of small and heavy non-spherical particles settling in turbulence are very important. For example, in natural systems such as ice clouds and proto-planetary disks the particle spectra evolution is strongly dependent on the collision induced growth rate; in technical systems such as the paper making process the accumulation of fibers is crucial. Nevertheless, the influence of the particle shape on the collision probability in turbulence is virtually unknown. Building on our recent investigation on the collision rate of monodisperse suspensions of ellipsoidal particles (Siewert et al., J. Fluid Mech. 758, 686-701, 2014), we show theoretically and by direct numerical simulations that the behavior of ellipsoids subject to turbulence and gravity is different from the behavior of spheres. Due to the dependence of the particle settling velocity on the particle orientation, the relative velocity at contact is influenced by turbulence. When ellipsoids differ either by mass or shape, their contact velocity is randomized by the randomized particle orientation. For particles heavier than the fluid these orientation dependent settling velocity differences are substantially larger than the relative velocities directly induced by the turbulent fluctuations.

Introduction

During the last decade one field of very active research was the estimation of collision rates of small and heavy spherical particles suspended in a turbulent flow. Motivated by several problems involving collision induced particle growth such as droplet growth in warm clouds [1] and planetesimal formation in protoplanetary disks [2], a large number of numerical [3, 4, 5] and theoretical [6, 7, 8] studies has been conducted on inertial spheres in turbulence. Several interaction phenomena of particle inertia with fluid turbulence and gravity have been identified increasing the collision rate of small particles. Most of these findings are now experimentally verified [9, 10, 11]. Thus, it is accepted that turbulence can dramatically accelerate the particle spectra evolution since at the begin the growth rate of the very small particles is moderately enhanced [12].
However, the collision rates of non-spherical particles in turbulence are virtually unknown since these collisions are notoriously hard to investigate in experiment or simulation. We recently showed that the collision rate of monodisperse suspensions of ellipsoids is drastically increased compared to spheres of the same mass due to an order of magnitude increased contact velocity [13]. In this study, we show results for the bidisperse collision rate of ellipsoids differing in shape.

Nomenclature

g	Gravitational acceleration
η_k	Kolmogorov length scale
τ_k	Kolmogorov time scale
u_k	Kolmogorov velocity scale
$Fr_t = u_k/(\eta_k g)^{0.5}$	Turbulent Froude number
a, b, c	Ellipsoidal principal axes
$\beta = c/a = b/a$	Ellipsoidal aspect ratio
τ_p	Particle translation time scale
v_t	Settling velocity
$Sv = v_t/u_k$	Non-dimensional settling velocity
$St = \tau_p/\tau_k$	Non-dimensional time scale
$\langle\lvert w_r\rvert\rangle$	Mean radial relative velocities
$\cos\alpha = \mathbf{c_1 c_2}/(\lvert\mathbf{c_1}\rvert\lvert\mathbf{c_2}\rvert)$	Contact angle

Theory

Very often the density of particles suspended in a turbulent fluid flow is significantly higher than the fluid density. For liquid or frozen water particles and many types of solid particles in turbulent air a density ratio of the order of 1000 is typical. Hence, the gravity induced settling velocity v_t takes on large values, i.e., is large compared to the turbulent fluctuation velocities even if the particles are smaller than the smallest turbulent scale, the Kolmogorov scale η_k. However, for non-spherical particles this settling velocity is orientation dependent.

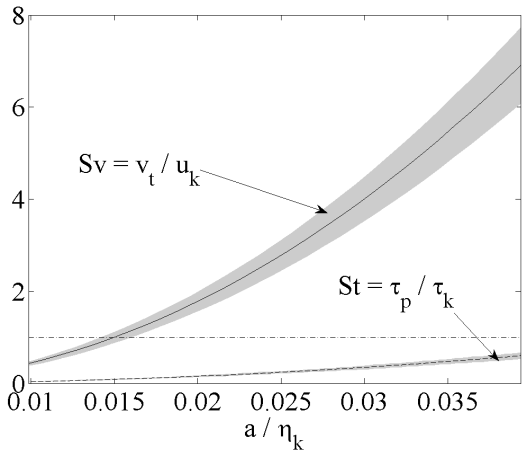

Figure 1: Dimensionless parameters characterizing ellipsoidal particles at an aspect ratio $\beta = 0.25$ in a turbulent flow at a turbulent Froude number $Fr_t = u_k/(\eta_k g)^{0.5} = 0.3$. Settling velocity non-dimensionalized by the Kolmogorov velocity scale $Sv = v_t/u_k$ (–) and particle time scale non-dimensionalized by the Kolmogorov time scale $St = \tau_p/\tau_k$ (- -). The gray shaded area represents the orientation dependent spread.

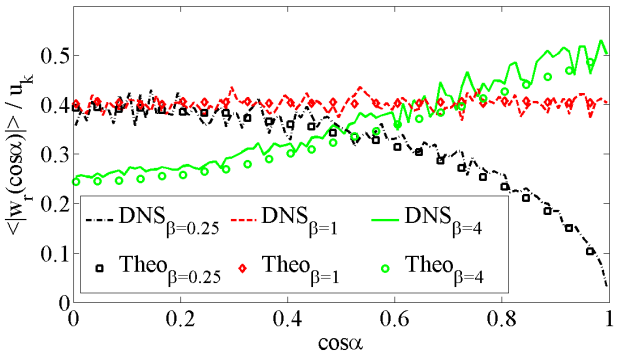

Figure 2: Non-dimensionalized radial relative velocities at contact $\langle|w_r|\rangle / u_k$ of a reference ellipsoid at $a/\eta_k = 0.03$ and $\beta_1 = 0.25$ as a function of contact angle $\cos\alpha = \mathbf{c_1 c_2}/(|\mathbf{c_1}||\mathbf{c_2}|)$ with collision partners at the same mass and volume but changing shape; black dash-dot line $\beta_2 = 0.25$, red dashed line $\beta_2 = 1$, green full line $\beta_2 = 4$. The relative velocity of equal sized spheres, i.e., $\beta_1 = \beta_2 = 1$ is constant at $\langle|w_r|\rangle / u_k = 0.05$ (not shown). For comparison $\langle|w_r|\rangle / u_k$ calculated for the ellipsoids settling randomly orientated in a quiescent fluid is given by corresponding colored symbols.

In this paper, we restrict ourselves to very small, heavy, and rotationally symmetric ellipsoids defined by their axes a = b = c/β, with β being the aspect ratio. However, we think that the arguments presented can be applied to all kind of non-spherical particles with ellipsoids being a first order model. Fig. 1 shows the non-dimensional settling velocity Sv and time scale St of a prolate ellipsoid at the aspect ratio β = 0.25 as a function of its size. While the particle time scale τ_p remains small compared to the Kolmogorov time scale τ_k, the orientation dependent settling velocity is significantly higher than the Kolmogorov velocity scale u_k at this moderate turbulence intensity characterized by the turbulent Froude number $Fr_t = u_k/(\eta_k g)^{0.5} = 0.3$, with g being the gravitational acceleration. Even the orientation dependent spread of the settling velocity is on the order of the Kolmogorov velocity scale.

Thus the turbulent orientation distribution is more important than the turbulent velocity fluctuations themselves. The orientation distribution of inertial non-spherical particles is a very complex problem [14]. For monodisperse ellipsoids we found colliding ellipsoids to be mostly aligned due to the correlated fluid forces and moments; however, the rare unaligned colliding ellipsoids drastically increase the collision probability due to high gravitation induced relative velocities [13]. For polydisperse mixtures of spheres it is know that for increasing particle size differences the correlation between the particles decreases fast [15]. Hence, clustering or preferential concentration is only of minor importance. Extending this argument to polydisperse mixtures of ellipsoids we assume the orientation at contact to be practically random for collision partners of different size or shape. This allows to calculate the relative velocity at contact neglecting the smaller turbulent velocity fluctuations, i.e., to calculate the ellipsoidal relative velocities in a quiescent fluid.

The symbols in fig. 2 exemplarily show the mean radial relative velocities at contact $\langle|w_r|\rangle$ as a function of the contact angel for an ellipsoid at $\beta = 0.25$ in combination with ellipsoids at the same mass but changing shape. While this theoretical relative velocity is constant zero for equal sized spheres (not shown), it is on the order of the Kolmogorov velocity scale for unaligned ($\cos\alpha = 0$), equal ellipsoids [13]. For different shaped ellipsoids it does not drop off for aligned ($\cos\alpha = 1$) particles. Thereby we indicate that the ellipsoidal relatively velocity at contact will be relative independent of the contact angle distribution and very high compared to spheres even for particle combinations at the same mass and volume.

Simulation

To confirm our arguments, we conduct direct numerical simulations of a streamwise decaying turbulent flow and track several million one-way coupled ellipsoids by a Lagrangian point particle model based on Stokes flow conditions [15, 14, 13]. The relative velocity is sampled assuming contact at particle distances corresponding to contacting spheres of equivalent volume [13]. The results are shown as lines in fig. 2 together with the corresponding theoretical values. Despite the data have not fully converged due to the intermittent behavior of the contact relative velocity [5], it can be seen that the results match the theoretical predictions well. The relative velocity is slightly underpredicted due to the neglection of the turbulent fluctuations in the particle settling velocity. However, this turbulent contribution is much smaller than the gravitation induced part of the relative velocity. Hence, at constant particle mass the relative velocities of ellipsoids are an order of magnitude larger than for spheres. The same holds for the collision rate which linearly depends on the radial relative velocity at contact. A second contribution stems from particle clustering. As we will report in a future publication,

the assumption of complete uncorrelation with shape difference is not fully true. Indeed spheres cluster in different regions of the flow than ellipsoids but the regions of prolate and oblate ellipsoids overlap which increases the collision probability even further.

Conclusion

The results highlight the importance of combined effects of turbulence and gravity on small inertial particles. We believe that the presented arguments apply not only to ellipsoids but to all kinds of non-spherical particles as the prerequisite of orientation dependent settling velocities is generally fulfilled by non-spherical particles.

Acknowledgements

The funding of this project in the framework of the priority program SPP1276 METSTROEM by the German Research Foundation (DFG) under grant number SCHR 309/39 is gratefully acknowledged. The authors thank the High Performance Computing Center Stuttgart (HLRS) for the computing resources.

References

[1] Pruppacher, H., and Klett, J., 1997. Microphysics of clouds and precipitation. Kluwer Academic Publishers.

[2] Williams, J. P., and Cieza, L. A., 2011. “Protoplanetary disks and their evolution”. Annu. Rev. Astro. Astrophys., 49(1), pp. 67–117.

[3] Squires, K. D., and Eaton, J. L., 1991. “Preferential concentration of particles by turbulence”. Phys. Fluids, 3A, pp. 1169–1178.

[4] Wang, L.-P., Ayala, O., Rosa, B., and Grabowski, W. W., 2008. “Turbulent collision efficiency of heavy particles relevant to cloud droplets”. New J. Phys., 10, p. 075013.

[5] Bec, J., Biferale, L., Cencini, M., Lanotte, A. S., and Toschi, F., 2010. “Intermittency in the velocity distribution of heavy particles in turbulence”. J. Fluid Mech., 646, pp. 527–536.

[6] Falkovich, G., Fouxon, A., and Stepanov, M. G., 2002. “Acceleration of rain initiation by cloud turbulence”. Nature (London), 419, pp. 151–154.

[7] Chun, J., Koch, D. L., Rani, S. L., Ahluwalia, A., and Collins, L. R., 2005. “Clustering of aerosol particles in isotropic turbulence”. J. Fluid Mech., 536, pp. 219–251.

[8] Ayala, O., Rosa, B., and Wang, L.-P., 2008. “Effects of turbulence on the geometric collision rate of sedimenting droplets. Part 2. Theory and parameterization”. New J. Phys., 10, p. 075016.

[9] Aliseda, A., Cartellier, A., Hainaux, F., and Lasheras, J. C., 2002. “Effect of preferential concentration on the settling velocity of heavy particles in homogeneous isotropic turbulence”. J. Fluid Mech., 468, 10, pp. 77–105.

[10] Saw, E.-W., Shaw, R. A., Salazar, J. P. L. C., and Collins, L. R., 2012. “Spatial clustering of polydisperse inertial particles in turbulence: II. Comparing simulation with experiment”. New J. Phys., 14(10), p. 105031.

[11] Bewley, G. P., Saw, E.-W., and Bodenschatz, E., 2013. “Observation of the sling effect”. New J. Phys., 15(8), p. 083051.

[12] Xue, Y.,Wang, L.-P., and Grabowski,W.W., 2008. “Growth of cloud droplets by turbulent collision-coalescence”. J. Atmos. Sci., 65(2), pp. 331–356.

[13] Siewert, C., Kunnen, R. P. J., and Schröder, W., 2014. “Collision rates of small ellipsoids settling in turbulence”. J. Fluid Mech., 758, pp. 686–701.

[14] Siewert, C., Kunnen, R. P. J., Meinke, M., and Schröder, W., 2014. “Orientation statistics and settling velocity of ellipsoids in decaying turbulence”. Atmos. Res., 142, pp. 45–56. The 16th International Conference on Clouds and Precipitation.

[15] Kunnen, R. P. J., Siewert, C., Meinke, M., Schröder,W., and Beheng, K., 2013. “Numerically determined geometric collision kernels in spatially evolving isotropic turbulence relevant for droplets in clouds”. Atmos. Res., 127, pp. 8–21.

Combined measurements of flow field and rigid fiber rotation/translation in near homogeneous isotropic turbulence

Lilach Sabban, Asaf Cohen, René van Hout

Faculty of Mechanical Engineering, Technion-Israel Institute of Technology, Haifa 32000, Israel

Keywords: Dispersion, Fiber, Holography, Particle/fluid interactions, PIV, Turbulence

Abstract

Time resolved, planar particle image velocimetry (TR-PIV, 3 kHz) and two-orthogonal view, digital holographic cinematography (2 kHz) were used to measure 3D fiber trajectories/orientation dynamics in near homogeneous isotropic air turbulence (HIT) with dilute suspended fibers. HIT (Taylor scale Reynolds number 144) was generated in the center of a 40^3 cm^3 cube by eight woofers mounted on each of its corners. Two different batches of nylon fibers having a length of 0.5 mm and diameter of 14 and 19 μm were released from the chamber's top. Fibers had Stokes numbers of order one and results showed that they resided in regions of low vorticity. Fiber Reynolds numbers based on fiber length were below 30 indicating that turbulence modification due to vortex shedding was absent. Translational dispersion coefficients were higher for the lowest Stokes number fibers. Results further indicated a weak correlation between the fiber's in-plane orientation angle and that of the extensional strain rate.

Introduction

Fiber suspension flows are important in a variety of applications such as the paper making industry and control/prevention of atmospheric or indoor asbest fiber dispersal. In addition, small concentrations of polymers or large aspect ratio fibers can greatly reduce the drag in a turbulent flow.

Olson and Kerekes (1998) derived the equations of mean and fluctuating velocities for rigid, thin inertialess fibers in turbulent flows and showed that translational and rotational dispersion coefficients decreased as the ratio of L_f to the Lagrangian integral length scale increased.

Several numerical investigations have dealt with translational and rotational, inertialess fiber dynamics in 3D turbulent flows. Olson (2001) numerically simulated inertialess fibers in a stochastic turbulent flow and showed that as L_f increased, the rate of the translation and rotational dispersion decreased as a result of spatially averaging eddy interactions along the fiber length. Shin & Koch (2005) simulated the motion of neutrally buoyant fibers in stationary, HIT (Re_λ=16.5-53.3). They showed that auto-correlations of fiber velocity and acceleration decayed more slowly with increasing fiber length. Furthermore, while the large turbulence scales mainly govern translational motion, fiber rotational motion is affected by a wide range of scales. In a DNS simulation of HIT, Ni et al. (2014) showed that fibers and vorticity are aligned with each other since both independently align with the strongest Lagrangian stretching direction, defined by the maximum eigenvector of the left Cauchy-Green strain tensor.

Few experiments in fiber suspensions have been able to measure both the spatially and temporally resolved flow field and fiber dynamics. Parsa et al. (2011) measured the motion of relatively large neutrally buoyant fibers in periodic and non-periodic, chaotic quasi-2D flow while Parsa et al. (2012) resolved the 3D fiber orientation dynamics in 3D turbulence (R_λ = 160 and 214). Parsa et al. (2011) found that the fiber rotation rate was well predicted by Jeffery's equation (Jeffery 1922). In addition, their results indicated that fibers only weakly aligned with the extensional direction of the strain rate tensor while a strong alignment with the direction of Lagrangian stretching was observed.

The present study is aimed at: (i) simultaneously measuring inertial fiber and flow field dynamics (ii) measuring rotational and translational dispersion coefficients in near homogeneous, isotropic air turbulence at Re_λ = 144. The measurements are conducted using high-speed, planar PIV enabling to simultaneously track fibers and flow field. Two orthogonal view, digital inline holographic cinematography was used to measure fiber 3D rotation/translation dynamics. Results on the fiber Reynolds number, preferential alignment with vortical structures and dispersion coefficients are presented.

Nomenclature

g	gravitational constant (ms^{-2})
u'	rms of the fluctuating air velocity (ms^{-1})
p_i	fiber unit orientation vector
D_{ii}	diffusion coefficient (m^2s^{-1})
L_f	fiber length (m)
Re_f	fiber Reynolds number
Re_λ	Taylor microscale Reynolds number
St	Stokes number
T_F	integral time scale (s)
U_r	relative velocity (ms^{-1})

Greek letters

ε	dissipation rate (m^2s^3)
η_k	Kolmogorov length scale (m)
ν	Kinematic viscosity (m^2s)
ρ_f	fiber density (kgm^{-3})
τ_k	Kolmogorov time scale (s)
ϕ_E	in-plane extensional direction of strain rate (rad)
ϕ_f	in-plane fiber orientation angle (rad)

Experimental Facility and Methodology

The measurements were performed in a 40×40×40cm^3 turbulence chamber (Hwang and Eaton 2004, Sabban and van Hout 2011). Near homogeneous, isotropic air turbulence was generated by eight woofers mounted on the corners of the chamber. The woofers were forced at a randomly changing frequency (90 to 110Hz) and phase in order to avoid standing waves. Near-HIT in the center of the chamber was validated by stereoscopic PIV measurements. Resulting Kolmogorov time and length scales were, τ_k= 2.27ms and η_k=185μm respectively; Re_λ=144 and u'=0.5 m/s (the reader is referred to Sabban and van Hout (2011) for further details).

Two sets of nylon fibers (ρ_f = 1.15 g/m^3, courtesy of Dr. Ir. R. Delfos, Technical University Delft) having the same nominal fiber length, L_f = 0.5 mm, but different diameter were released into the chamber. The two sets were characterized by *dtex* = 1.7 and 3.3 g/10,000m, leading to nominal diameters of 14 and 19 μm, respectively; Fiber response times were 2.83 and 5.08ms, respectively.

High-speed PIV measurements were performed using a system comprising a CMOS camera (Photron Ultima APX, 1024x1024 pixels up to 2kHz, 17 μm/pixel), a high speed laser (NewWave Pegasus, 532 nm, 10mJ/pulse), laser sheet optics and acquisition/data processing software (LaVision DaVis 7.4). The CMOS camera was equipped with a long working distance, microscopic lens (Infinity) providing a field of view (FOV) of 6.3×12.6 mm (Fig. 1a). Time resolved data were acquired at 3kHz (10 data sets, each 1.37 s duration), i.e. 6.8 times smaller than τ_k. Flow tracers (0.2-0.3 μm, Glycerine BP/purified water mixture) were introduced into the chamber after which the woofers were activated. In order to reach a statistically steady state, experiments were started at least one minute after activation of the woofers (and just after releasing the fibers). Fibers were released from the top of the chamber using a custom-made particle dispenser. The bottom part of the dispenser consisted of replaceable sieves with two, 2mm laser drilled holes.

The two orthogonal view, digital inline holographic cinematography system (see also van Hout et al. 2013) comprised a high speed laser (Crystalaser, 10 μJ/pulse at 10kHz) two high-speed, lensless CMOS cameras (Photron UltimaAPX), a spatial filter (aspheric focusing lens and 10 μm pinhole), collimating lens, a beam splitter and two mirrors to direct the light to the cameras. The volume of interest (VOI) was a cube of 17^3 mm^3 where the two collimated beams intersected (see Fig. 1b). Data were acquired at 2kHz (10 data sets, each 1 s duration).

Data processing of the TR-PIV images consisted of distinguishing and separating fibers from flow tracers. First, PIV images were binarized and subsequently, line elements were identified by applying the Hough transform. The number of detected tracks equalled 99 and 165 for *dtex* = 1.7 and 3.3, respectively. In each track, a fiber was followed in at least four consecutive frames.

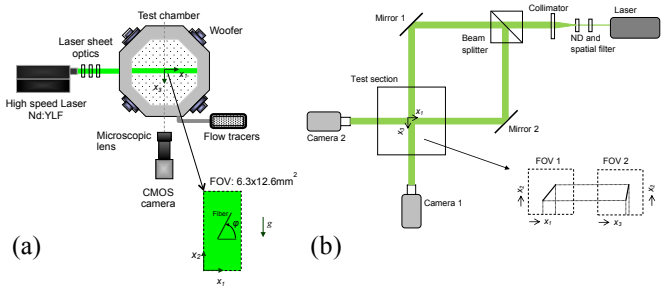

Figure 1: Schematic experimental setup (top view) (a) TR-PIV (b) Two orthogonal view digital inline holographic cinematography system.

Once detected, a rectangular mask was placed at the center of each detected fiber and rotated according to the determined fiber orientation. The resulting masked images now only containing the flow tracers, were processed using PIV (FFT based) algorithms. Velocity fields were obtained by multi-pass processing and decreasing window size, the smallest being 32×32 pixels with 50% overlap resulting in a vector spacing of 197 μm, comparable to η_k.

In addition, time-resolved 3D inertial fiber trajectories were obtained from reconstructed holograms acquired by both cameras. The reconstructions were binarized and collapsed onto one image containing all fibers present in the VOI at a certain time. Tracks were built for each camera separately by using a 'nearest neighbor algorithm'. Subsequently, tracks were matched between cameras based on constant vertical bias difference along tracks. A total of 641 and 538 tracks were found for *dtex* = 1.7 and 3.3, respectively.

Results and Discussion

Histograms of the fiber Reynolds number based on L_f, $Re_f = |U_r|L_f/\nu$ are presented in Fig. 2 for both *dtex* values. In both cases, histograms are strongly skewed with ~80% restricted to $Re_f < 10$. Maxima are about 20 and 30 for *dtex* = 1.7 and 3.3, respectively.

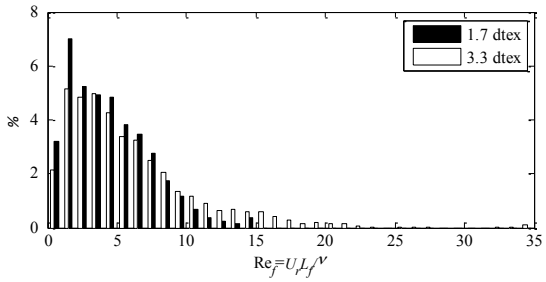

Figure 2: Histogram of the fiber Reynolds number.

Therefore, turbulence enhancement through vortex shedding will be absent when considering the fibers as cylindrical bodies (in a steady uniform flow). Note that for "violently" rotating fibers, one would consider the fiber length to be the relevant length scale, assuming a spherical body of fluid is set in motion by the randomly rotating fibers. In the present case, the standard deviation for completing one rotation was 23.1 and 20.7τ_k for *dtex* = 1.7 and 3.3, respectively.

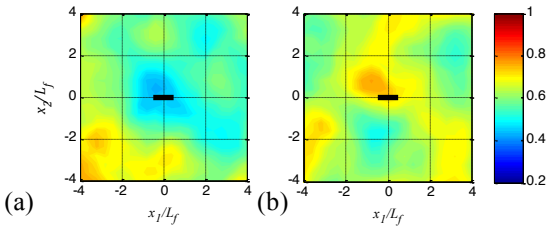

Figure 3: Mean out-of-plane vorticity normalized by its rms value in the fiber vicinity, *dtex* = (a) 1.7, (b) 3.3.

Fig. 3 shows that fibers with Stokes number, St = 1.25 (*dtex* = 1.7), reside in lower vorticity than *dtex* = 3.3 (St = 2.24). The mean swirling strength in the vicinity of the fibers (not shown) further strengthened the observation that fibers reside at the periphery of vortex cores.

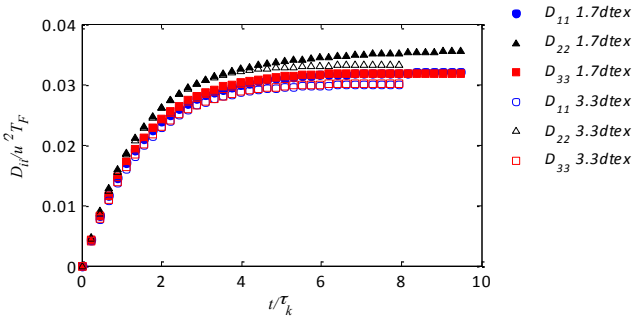

Figure 4: Normalized fiber translational dispersion coefficients as a function of time.

Translational dispersion coefficients shown in Fig. 4, are highest for *dtex* 1.7 while in the direction of gravity for both *dtex* 1.7 and 3.3, D_{22} is higher than in the transverse directions. Thus, increasing inertia reduces dispersion but increases dispersion in the direction of gravity.

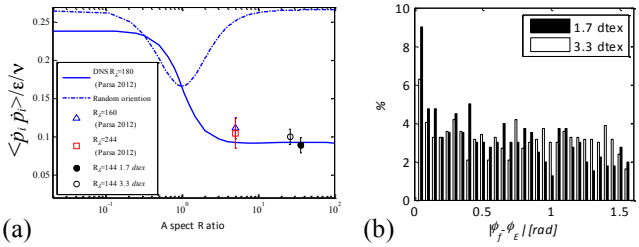

Figure 5: (a) Mean, normalized square rotation rate versus fiber aspect ratio, (b) Difference between fiber and extensional strain rate angle.

From the holographic measurements, the unit orientation vector, $\boldsymbol{p}$, along the fiber was determined. Present results of the normalized mean square rotation rates, $\langle \dot{p}_i \dot{p}_i \rangle / \varepsilon / \nu$, are compared in Fig. 5a to those measured for neutrally buoyant fibers (Parsa et al. 2012), randomly oriented rods and DNS results of anisotropic tracers in HIT (Re_λ=180). Present values are considerably lower than those predicted for randomly oriented rods while there is good agreement with the DNS of anisotropic tracers in HIT (Re_λ=180). Therefore, present results indicate fiber preferential alignment and a weak correlation with the extensional strain rate direction (Fig. 5b).

Conclusions

Measurements of flow field and rigid fiber translation/rotation rate in near homogeneous isotropic air turbulence were investigated. Fiber Reynolds numbers were low and hence turbulent modification was not expected to occur. In addition, vorticity and swirling strength in the vicinity of fibers indicated that inertial fibers reside at the periphery of vortices. Increasing fiber inertia reduced translational dispersion. Values of normalized, mean square fiber rotation rates indicated preferential alignment.

Acknowledgements

This work was supported by the Israel Science Foundation under grant no. 915/10 and in part by the Edmund J. Safra Philanthropic Foundation, the Wolfson Family Charitable Trust and the Technion Fund for Promotion of Research. We furthermore acknowledge the support of EU COST Action FP1005.

References

Jeffery, G.B. The motion of ellipsoidal particles immersed in viscous fluid. Proc. R. Soc. A, Vol. 102, 161-179 (1922)

Olson, J.A. & Kerekes, R.J. The motion of fibres in turbulent flow. J. Fluid Mech., Vol. 377, 47–64 (1998)

Olson, J.A. The motion of fibers in turbulent flow, stochastic simulation of isotropic homogenous turbulence. Int. J. Multiphase Flow, Vol. 27, 2083-2103 (2001)

Parsa, S., Guasto J.S., Kishore, M., Ouellette N.T., Gollup, J.P. & Voth, G.A. Rotation and Alignment of rods in two-dimensional chaotic flow. Phys. Fluids, Vol. 23, 043302 (2011)

Parsa, S., Calzavarini, E., Toschi, F. & Voth , G.A. Rotation rate of rods in turbulent fluid flow. Phys Rev. Lett., Vol. 109, 134501 (2012)

Ni, R., Ouellette, N.T. & Voth, G.A. Alignment of vorticity and rods with lagrangian fluid stretching in turbulence. J. Fluid Mech., Vol. 743, R3 (2014)

Sabban, L. & van Hout, R. Measurements of pollen grain dispersal in still air and stationary, near homogeneous, isotropic turbulence. J. Aeros. Sci., Vol. 42, 867-882 (2011)

Shin, M. & Koch, D.L. Rotational and translational dispersion of fibres in isotropic turbulent flows. J. Fluid Mech., Vol. 540, 143 (2005)

van Hout, R., Sabban, L. & Cohen A. The use of high speed PIV and holographic cinematography in the study of fiber suspension flows. Acta Mech., Vol. 224, 2264-2280 (2013)

Electrical Tomography use for Imaging Pulp Suspensions Flow in Pipes: Restraints and Evolution

Pedro Manuel Faia[1], Maria Graça Rasteiro[2], Fernando Garcia[2], Rui Silva[2], Hugo Costa[1] and Bruno Branco[1]

[1] *Electrical and Computers Engineering Department, Faculty of Sciences and Technology of the University of Coimbra, and CEMUC – Centre of Mechanical Engineering, Portugal.*
[2] *Chemical Engineering Department, Faculty of Sciences and Technology of the University of Coimbra, and CIEPQPF – Research Centre on Chemical Process and Forest Products, Portugal*

Keywords: EIT, Pine and eucalypt pulp suspensions, Multiphase flow, Velocity estimation.

Abstract

Many approaches, either experimental or theoretically based, have been followed to model pulp fibres suspensions flow in pipes. The quality of experimental data is in any case of paramount importance for the accuracy of the flow models. The methods currently used lack the spatial and temporal resolution needed for problem identification and meaningful process control and are generally intrusive and slow. An Electrical Impedance Tomography (EIT) apparatus was developed to circumvent such limitations with additional characteristics of low cost, portability and safety of handling. The usefulness of this equipment is demonstrated to assess the fibres distribution in circular pipes as a function of the flow rate and for the estimation of the suspensions velocity. Some difficulties and implemented solutions are also reported.

Introduction

Electrical Impedance Tomography, EIT, is a imaging technique with many applications in the medical field and industrial processes [1, 2]. EIT has become a popular research and diagnostic tool for both medical and industrial applications because of the low cost of equipment and the non-invasive nature of this imaging procedure. In EIT an electrical current is injected through a set of electrodes placed in the boundary of the domain under study, thereby resulting an electrical field that is conditioned by the materials distribution within the domain. The resulting electrical potentials in the domain perimeter can be measured using the remaining electrodes [3]: the procedure is only complete when all electrodes are used for injection or projection, so the cycle has as many projections as the number of electrodes. For a dynamic system such as suspension flow, it is required that the system performs the reconstruction of the conductivity/resistivity distribution in the possible smallest length of time.
From a mathematical standpoint the EIT problem can be divided in two: a forward problem, that calculates the electrical potentials in the boundary using an initial estimation of the conductivity/resistivity distribution and an inverse problem that reconstructs the conductivity/resistivity distribution based on the electrical potentials measured in the boundary.

Experimental Facility

The tests were conducted in a pilot rig described elsewhere [4] and schematically shown in figure 1. In short, the test section consisted of a horizontal PVC pipe, 7.5m in length and 100 mm in internal diameter. The flow rate can be regulated by manipulation of two valves located after the pump and measured by a flow meter. Appropriate lengths were inserted before and after the test section to account for entrance and exit effects. The EIT electrodes rings consisted of 16 or 32 Titanium based electrodes (each with a diameter of 5 mm), circumferentially and equally spaced, and were mounted in a Perspex tube inserted in the rig between the measuring pressure taps.
The EIT system used in the present work, was already described elsewhere [5]. It measures the differences in both the real and the imaginary parts of the impedance. For all tests presented, an excitation frequency of 10 kHz with $2V_{pp}$ amplitude was imposed, and opposite injection and adjacent measuring protocol were used. For image reconstruction, the open source software EIDORS [6], considering direct differential measured voltages and using a structured Mesh consisting of 2304 linear elements and 1201 nodes, was used. EIDORS implements a non-linear back projection method using a regularized algorithm (Tikhonov regularization). To solve the forward problem the Complete Electrode model (CEM) [7] was chosen. In the reconstructed images of the conductivity distribution in the pipe cross section, the electrode number 1 corresponds to top position in the cross section of the tube; a darker blue colour corresponds to a lower conductivity region, where the concentration of the fibres is higher, while yellow or red colours identify higher conductivities regions, where the fibres are present in lower concentrations.

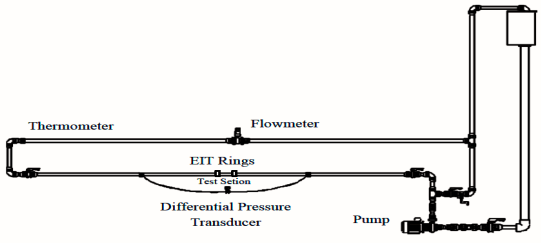

Figure 1: Pilot rig schematic

Results and Discussion

Fibres distribution as a function of suspension velocity and concentration

For the depicted tests in this section, a 32 electrodes ring was used. In the first tests, an *Eucalyptus* pulp suspension, with an averaged fibre length of 0.706±0.03 mm, collected from a local paper mill, was used. EIT images obtained for a flow velocity of 2 m/s and with two different pulp concentrations (industrial water conductivity 1.197 mS/cm) are shown in Figure 2. It can be observed that the pulp suspension collected from the paper mill has unique electrical properties. In fact, a low conductivity difference was found between pulp fibres and the liquid suspension itself. At low velocity it is known that the suspension flows as a plug of fibres and water, and, consequently, a darker blue colour was expected in the inner region, corresponding to a lower conductivity due to the presence of fibre, as compared with the outer region, near the walls. However, this is opposed to the observations (Figure 2). The ions present in high concentration in the industrial medium are highly adsorbed by the fibres, rendering the inner plug region more conductive. The same trend was observed when the fibres were separated from the industrial liquid medium and re-dispersed in tap water doped with NaCl (0.94 mS/cm), although the gradient of the conductivity is smaller in this case.

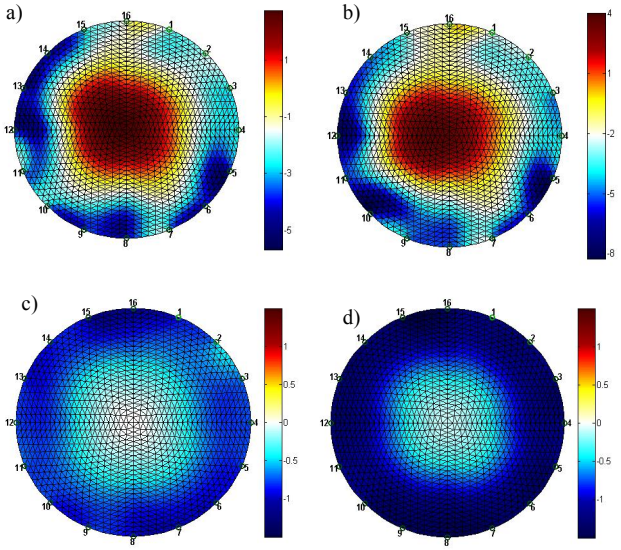

Figure 2: EIT images obtained with a flow velocity of 2 m/s, for pulp concentrations of 2.7 and 1.6 % (w/w), in industrial water, a) and b), and in tap water doped with NaCl with a conductivity of 0.94 mS/cm, c) and d).

It was then decided to squeeze and wash the pulp fibres in water, and by substituting the industrial water by tap water doped with NaCl with an adjusted conductivity to the desired value. The conjugation of both actions allowed the EIT to distinguish correctly the conductivity change differences of the phases present, as observed in figure 3: the fibres plug dimension and the intensity of the blue colour change with the velocity increase. In fact, as the velocity increases the plug starts to spread gradually, which is noticeable by the enlargement of the blue region in the EIT images.

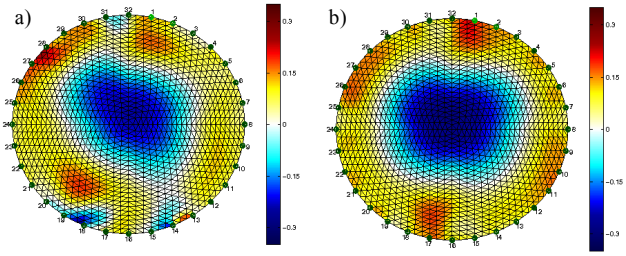

Figure 3: EIT images obtained with a pulp concentration of ± 2.8% (w/w), for flow velocities of 0.7 and 2.6 m/s, in tap water doped with NaCl with a conductivity of 1.705 mS/cm, a) and b) respectively.

Table 1- Table of concentrations and flow velocities tested.

Type of Pulp	Concentration (W/W)	Flow velocities (m/s)	Suspension conductivity ($mS.cm^{-1}$)
Eucalypt	2.35	0.5, 1, 1.5, 2, 2.5, 3	1.460
	1.5	0.5, 1, 1.5, 2, 2.5, 3	1.150
	1	0.5, 1, 1.5, 2, 2.5, 3	1.128
Pine	2.35	0.5, 1, 1.5, 2, 2.5, 3	1.471
	1.5	0.5, 1, 1.5, 2, 2.5, 3	1.461
	1	0.5, 1, 1.5, 2, 2.5, 3	1.435

So once solved the described sensitivity issue, further experimental work was pursued using different types of fibers. The behaviours of *Eucalyptus* pulp suspensions (average Fibre length of 0.706 mm) and of *Pine* pulp suspensions (average Fibre length of 2.18 mm), both collected in a local paper mill, were compared, as in Figure 4, under the conditions listed in Table 1. Before analysing the suspension flow images obtained, we must reinforce that the tomography reflect voltage differences measured. For fibres concentrations of around 2.35%, the fibres distributions in the cross pipe section are diverse for the two types of fibres. Concerning the *pine* suspension a plug type flow behaviour is already visible even at the lowest velocity, with an increase in the plug (size and intensity of the blue colour) when the velocity increases up to 2m/s (see Figure 4 a), c) and e)); however, a further increase in the velocity up to 3m/s leads to a breakage apart of the plug, as in Figure 4 g), as expected for this type of long and stiff fibres. However, concerning the *Eucalyptus* fibres suspension, at the lowest velocity the fibres remain more or less dispersed in the cross pipe section (see Figure 4b)), and the plug only starts to be visible at the velocity of 1m/s and becoming more dense at 2m/s (Figures 4d) and 4f)). Similarly to the pine fibres, a further increase in the Eucalyptus suspension velocity up to 3m/s leads to the plug breakage apart (Figure 4h)). These differences in the EIT reconstructed images for this concentration are related with the physical properties of the fibres, in particular the fibre length and stiffness that originate different interactions between fibres when the suspensions flow in the tube.

For a Fibre concentration of around 1% (EIT images depicted in Figure 5), it was not possible to gatherer consistent data for the *Eucalyptus* fibers. Concerning the *pine* fibres suspension it is evident that they migrate and become agglomerated in a central plug at lower velocities

(in this case 0.5 m/s) than when the suspension is more concentrated as in Figure 4 where the fibres are more dispersed. However, at more diluted suspensions the strength of the interconnection of the fibres is lower and the plug breakage occurs as the velocity increases.

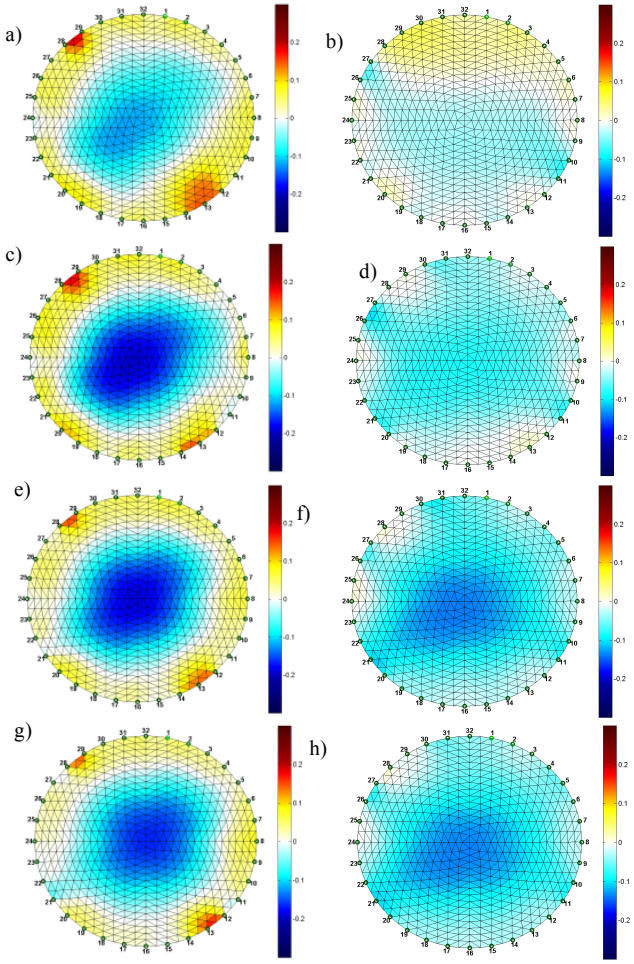

Figure 4: EIT images obtained with a concentration of ≅2.35% (w/w) of *pine* (left column: a), c), e) and g)) and *eucalypt* (right column: b), d), f) and h)) with increasing flow velocity (0.5 m/s, 1m/s, 2m/s and 3m/s, top to bottom).

It must be emphasized at this point that environmental factors that were not easily kept under control may affect the colour mapping of the reconstructed images. In particular, the temperature changes significantly during continuous testing due to the energy input from the pump and the fact the heat extraction was made by passing tap water in a tube immersed in the suspension: the temperature of this cooling water changes significantly according to the seasons. Changes in the suspension temperature affect the viscosity but mainly the electric conductivity of the suspension and, consequently, the colour map of the reconstructed images is affected.

Fibre flow velocity estimation

By using dual EIT planes and cross-correlation, EIT can also be used to determine the velocity profile in a pipe. For example Mosorov et al. [8] used a best-correlated pixel method to measure both axial and radial velocities simultaneously.

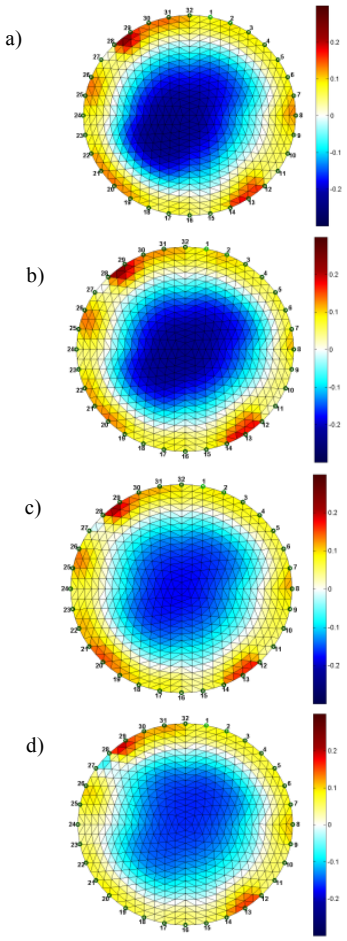

Figure 5: EIT images obtained with a concentration of ≅1% (w/w) of *pine*, a), b), c) and d) respectively for 0.5 m/s, 1m/s, 1.5m/s and 2.5m/s, top to bottom.

Independently of the procedure used a marker is needed. As a first approach, the introduction of a small fraction of conductive or non-conductive solid spheres in the flow was used. After several attempts without success to distinguish these markers in the EIT images, the authors decided to use instead a trace of a highly concentrated NaCl solution as a marker. For the purpose of introducing this NaCl solution in the flowing fibre suspension, an injection system was developed and added to the existing pilot rig: it was located around 3m before the first EIT electrode ring. This injector was built in such a way that the flow suffered almost no disturbance. For all the tests reported in this section, two 16 electrode titanium rings A and B were used, 30 cm separated apart, ring A closer to the injector inlet, as shown in fig. 6. The procedure here reported for estimating velocity was different from those reported in the literature, but, nevertheless, with some similarities with the one described by Dong et al. [9]. Instead of using the complete set of EIT projections, the authors made use of only the first projection: first the potential differences of each pair of the first projection with no marker injection in the flow were acquired; afterwards they were subtracted to the measured voltage differences obtained during the runs with NaCl injection. Finally, the sum of the module of those

differences was computed. For each suspension velocity and Fibre concentration tested, several injection trials were done, to assess the reproducibility of this approach. The conditions used for the velocity estimation are summarized in table 2. Some examples of data obtained with this approach are shown in figure 7: 3 sets of NaCl injections for suspensions containing 1 and 2% of *Eucalyptus* fibres and for the velocity of 0.25 m/s (figure 7 i) - ii)). In that same figure, a graph showing the estimated velocity versus the measured suspension velocity is represented (figure 7 ii): a quite reasonable estimation is obtained, and so the authors approach was validated. Moreover, as Fibre concentration increases the advance of the NaCl front is retarded due to the presence of more fibres, and also due to the structures that build up among fibres. This can be used, in the future, to evaluate those structures as a function of Fibre concentration and flow velocity.

Table 2- Table of fibre concentrations and flow velocities used for the velocity estimation tests.

Concentration (W/W)	Flow velocities (m/s)
3	0.25, 0.5
2	0.25, 0.5, 0.75, 1
1	0.25, 0.5, 0.75, 1

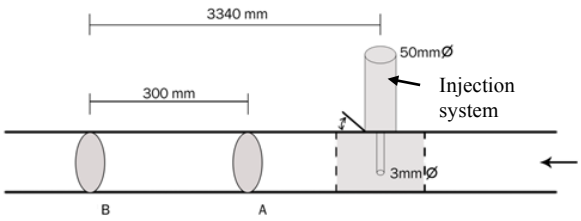

Figure 6: Schematic of the relative position of the EIT electrodes sections and injection inlet.

Conclusions

The authors presented the work carried during the last years regarding the use of EIT for the experimental characterization the distribution of fibres in suspensions flows and for a simple and rapid estimation of the Fibre suspensions velocity. *Eucalyptus* and *Pine* pulp suspensions with different concentrations were tested for varying flow velocities. The portability and the low cost of this technique, considering the results here presented, clearly justify its use at an industrial scale, in spite of its lower spatial resolution when compared with other tomographic procedures

Acknowledgements

COST Action FP1005 support, Fibre suspension flow modelling – a key for innovation and competitiveness in the pulp & paper industry, is gratefully acknowledged. The authors thank the financial support of Fundação para a Ciência e Tecnologia through the projects, contract PTDC/EQU-EQU/112388/2009 (COMPETE-01-0124-FE DER-015247), and contracts Pest-C/EME/UI0285/2013 and Pest-C/EQB/UI0102/2013, both financed by FCT/MCTES (PIDDAC) and co-financed by the European Regional Development Fund through the program COMPETE.

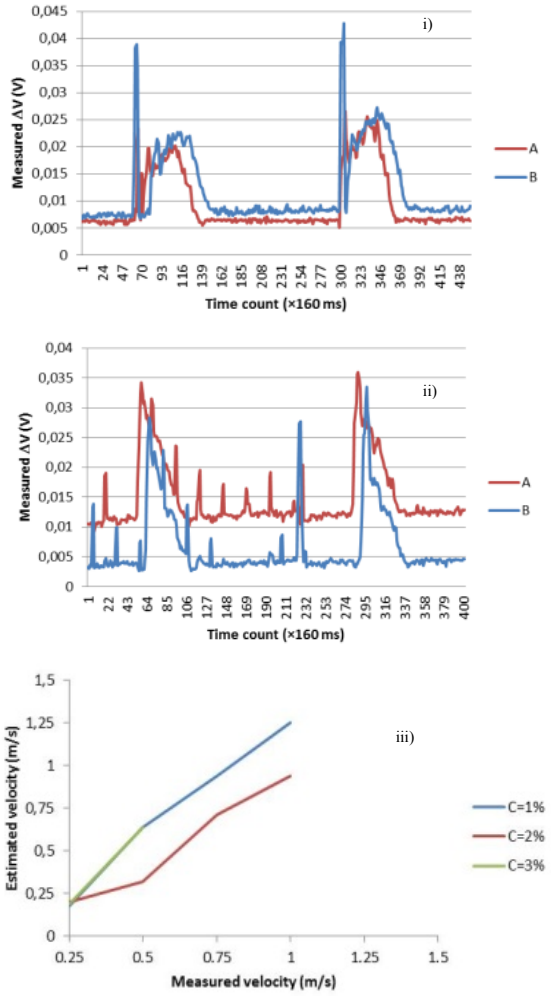

Figure 7: EIT injection test trials for fibre suspension concentrations of 1% and 2%, at the velocity of 0.25 m/s, i) and ii) respectively, and estimated velocity versus measured velocity for all tested Fibre concentrations, iii).

References

[1] Cheney M., Issacson D., Newell J.C., *SIAM Rev.*, **41**, 85, 1999.
[2] Dickin F., Wang M., *Meas. Sci. Technol*. **7**, 247, 1996.
[3] J. Malmivuo, R. Plonsey, *Bioelectromagnetism: Principles and Applications of Bioelectric and Biomagnetic Fields*, Oxford University Press, New York – Oxford, 1995.
[4] Ventura C., Garcia F.A.P., Ferreira P., Rasteiro M.G., *Tappi Journal*, **7**(8), 20, 2006.
[5] Faia P.M., Ferreira A.R., Santos M.J., Santos J.B., Silva R., Rasteiro M.G., Garcia F.A.P., *Particulate Science and Technology*, **30**, 329, 2012.
[6] Polydorides N., Lionheart W.R.B., *Measurement Science and Technology*, **13**(12), 1871, 2002.
[7] Cheng K.S., Isaacson D., Newell J.C., Gisser D.G., *IEEE Transactions on Biomedical Eng*., **36**(9), 918, 1989.
[8] Mosorov V., Sankowski D., Mazurkiewicz L., Dyakowski T., *Measurement Science and Tech*., **13**, 1810, 2002.
[9] Dong F., Xu Y.B., Xu L.J., Hua L., Qiao X.T., *Flow Measurement and Instrumentation*, **16**, 191, 2005.

MRI of fibre suspension flows: Quantification of turbulence intensity

Jordan MacKenzie[1], Fredrik Lundell[1], Agne Swerin[2,3]

[1]*Linné FLOW Centre, KTH Mechanics, KTH Royal Institute of Technology*
[2] *SP Technical Research Institute of Sweden – Chemistry, Materials and Surfaces*
[3]*Department of Chemistry, Surface and Corrosion Science, KTH Royal Institute of Technology*

Keywords: MRI, Fibre suspension flow, Turbulence

Abstract

The focus of the present work is an experimental study of the transition and development of opaque fibre suspensions in Hagen-Poiseuille flow. We have measured the time averaged velocity profiles using phase-contrast MRI (Magnetic Resonance Imaging) at a Reynolds number well below the drag reducing regime. An insert with six holes was used to straighten the flow. We were able to measure the distribution of the mean velocity and streamwise turbulent fluctuations as the flow developed downstream of the flow-straightener. We found that a 1% (w/w) fibre suspension became fully developed 8.5D after exiting the insert. The distribution of the streamwise turbulent fluctuations indicated that the flow, 1D from the insert is asymmetric and highly turbulent. When the flow was fully developed, the streamwise turbulent fluctuations suggest that global instabilities exist in regions within the pipe's cross-section.

Introduction

The flow of cellulose fibre suspensions in straight tubes go through a number of transitional stages. Most authors discuss the stages of transition for fibre suspension flows as either plug, mixed, or turbulent. In the recent work by Jäsberg (2007), the stages of transition were experimentally investigated using both a laser technique and ultrasonic Doppler velocimetry (UDV). Jäsberg (2007) characterized the transition of fiber suspension flows in a pipe to five stages:

I. Plug flow with direct fiber contact with the wall,
II. plug flow regime with lubrication layer,
III. plug flow regime with incipient fluid phase turbulence,
IV. mixed flow regime,
V. fully turbulent regime.

In this work, we extend the research by Jäsberg (2007) and quantify the flow field of both water and cellulose fiber suspensions in Hagen-Poiseuille flow by MRI. We focus on the mixed and fully turbulent regime where by introducing complex geometries, we can observe the development and mixing of fiber suspensions along the streamwise direction.

Nomenclature

f	Friction factor
Re	Reynolds number
MRV	Magnetic resonance velocimetry
D	Pipe diameter (35 mm)
$T.I.$	Turbulence intensity
U_C	Centreline velocity (cm/s)
$\rho\langle u_i u_i \rangle$	Streamwise turbulent stress (g/cm•s^2)

Experimental Facility

The experimental facility is located at KTH Mechanics in Stockholm, Sweden. We measure the flow of water and fibre suspensions in a 35 mm diameter pipe with a permanent 1 Tesla MRI instrument. The MRI-images are captured in a fixed region along the flow loop, which is greater than 100 pipe diameters from the last major disturbance (i.e. from a pipe bend, flow splitting, etc.). During imaging we simultaneously measure the pressure drop and pressure fluctuations using a low and high frequency differential pressure transducer, respectively.

Results and Discussion

To confine our Reynolds number (Re) state space for MRI imaging, we initially measured the friction factor for pulp suspensions and water, for a range of Reynolds numbers. Figure 1 shows that for a 1% (w/w) fibre suspension, the friction factor drops to a value less than that measured with water at a Re ≈ 40 000.

The drop in friction factor indicates turbulent drag reduction,

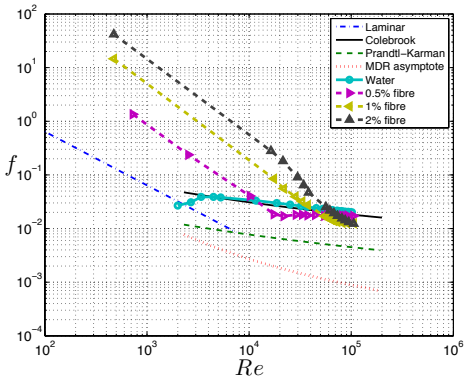

Figure 1: Friction factor vs. Re data for flow through a 35 mm diameter pipe.

which occurs when the flow of a fibre suspension is fully turbulent. Imaging at Reynolds numbers below this limit, we found that at a Re ≈ 10 200, instabilities were apparent in the MRI images for 1% (w/w) fibre suspensions. We interpret the presence of instabilities by the local break down of the fibre plug, a result of the turbulent stresses becoming greater than the plug yield stress. To assess the development of these instabilities in fibre suspension flows, we introduced an insert with six equally spaced 9 mm diameter holes into the flow loop. The insert acts as a body which breaks up large-scale instabilities, resulting in a flow which undergoes mixing. By moving the position of the insert, relative to the magnet's center, we were able to directly measure the stages of mixing and resulting development of water and fibre suspensions in Hagen-Poiseuille flow. Figure 2 presents some of the findings of this study.

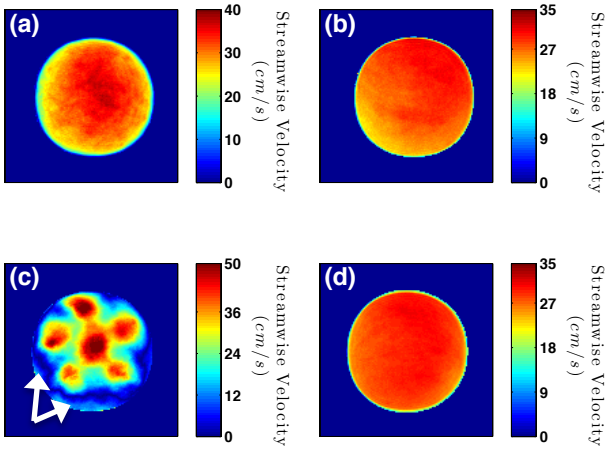

Figure 2: Streamwise velocity profiles measured from MRI. (a) Water (no insert). (b) 1% fibre suspension (no insert). (c) 1% fibre suspension (insert located 1D upstream from the magnet's centre). (d) 1% fibre suspension (insert located 8.5D upstream from the magnet's centre).

Figure 2(a) shows that at a Re ≈ 10 200, the flow is highly unstable in the near wall region without the insert present in the flow. Introducing 1% (w/w) cellulose fibre, Figure 2(b) shows that a large instability in the bottom left quadrant of the pipe exists. We have not, so far, assessed the root cause of this instability; however, it is clear that the turbulent stresses at Re ≈ 10 200 are, in some regions, locally greater than the plug yield stress.

Introducing the insert 1D from the magnet's center, we found that the flow through the insert is slightly asymmetric. Figure 2(c) shows this explicitly, where the maximum velocity within the holes of the insert ranged from 40 – 50 cm/s. The regions which are highlighted with arrows are a result of a lubrication layer forming between the insert and pipe wall. This was unavoidable due to the requirement to move the insert along the pipe's axis, limiting the ability to perfectly seal the gap between the wall and insert's edge. Increasing the distance of the insert and magnet center to 8.5D, we found that the 1% fibre suspension became fully developed, to where the instability observed in Figure 2(b) was no longer present. This can be seen in Figure 2(d).
In an effort to quantify the turbulent stresses, and resulting turbulence intensities using phase-contrast MRI, we adopted the method proposed by Dyverfeldt et al. (2006). They found that, by assuming a spin velocity distribution (e.g. Gaussian), the time averaged turbulent fluctuations could be quantified within each voxel of the MRI scan. As an initial case, we varied the first gradient moment strength over 13 values, essentially capturing the majority of the spin velocity distribution.

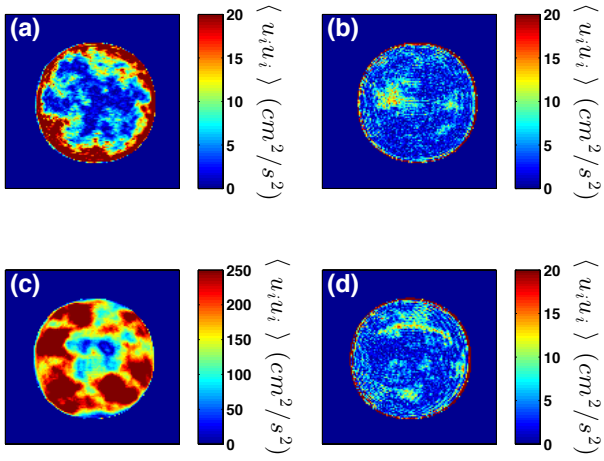

Figure 3: Streamwise turbulent fluctuations measured from MRI. (a) Water (no insert). (b) 1% fibre suspension (no insert). (c) 1% fibre suspension (insert located 1D upstream from the magnet's centre). (d) 1% fibre suspension (insert located 8.5D upstream from the magnet's centre).

The streamwise turbulent fluctuations presented in Figures 3(a) and 3(b) were found by varying the first gradient moment strength over 13 values, resulting in a validation of the Gaussian distribution assumption. It can be seen from Figure 3(a) that the turbulent fluctuations approach 20 cm^2/s^2 near the wall, an order of magnitude higher than in the pipe's core. Comparing the turbulence intensities to, for example, the work of Alfredsson et al. (2012), showed that in both works the turbulence intensity (i.e. T.I. = $\langle u_i u_i \rangle^{0.5}/U_C$) approaches 4% towards a pipe's centreline. With the presence of fibre, Figure 3(b) shows that the turbulent stresses are below 5 g/cm•s^2 in the majority of the pipes cross-section, amounting to a turbulence intensity of approximately 4%. Two regions were found with turbulent stresses approaching 15 g/cm•s^2, and could be a result of global instabilities. The high stress region, which is present left of the pipe's centre, correlates well with a portion of the low streamwise velocities shown in Figure 2(b). We hypothesize that the local increase in shear on the main flow may be leading to an increase in turbulent production in the spanwise direction. This could explain the fibre plug yielding in the bottom left quadrant, potentially leading to fibre settling and accumulation. The accumulation of fibres would likely result in low streamwise velocities along the bottom of the pipe, agreeing with the data shown in Figure 2(b).

The streamwise turbulent fluctuations presented in Figures 3(c) and 3(d) were found with only 2 first gradient moment strengths, resulting in the inability to verify the Gaussian velocity distribution. Nevertheless, Figure 3(c) indicates that

the streamwise velocity fluctuations near the pipe wall approach 20 cm/s. This was predictable considering that high turbulent levels are expected during the early developmental stages of the flow. Lastly, Figure 3(d) agrees well with Figure 3(b), where only small regions within the pipes cross-section exhibited turbulent stresses greater than 10 g/cm•s^2. This is again likely a result of a global instability.

Conclusions

With the experimental flow loop at KTH, we were able to effectively evaluate the friction factor for water and cellulose fibre suspensions for a range of Reynolds numbers. Confining our Reynolds number state space for MRI imaging to what can be described as the mixed regime of fibre suspension flows, we were able to measure the flow field and streamwise turbulent stresses with and without a complex geometry being present in the pipe. We found that in the early stages of fibre suspension mixing while in Hagen-Poiseuille flow, the streamwise turbulent stresses were an order of magnitude greater near the wall than at the pipe's core. Although it is likely that a swirling component exists in the flow, these data suggest that the distribution of turbulent stresses is asymmetric during flow development. The presence of a swirling component could explain the instability present in Figure 2(b) as well, since the streamwise turbulent stresses do not indicate a global instability throughout the entire low velocity region.

Acknowledgements

The authors thank Peter Bendel for his assistance in developing the MRI at KTH for imaging multiphase flows. Funding comes from the Bo Rydin Foundation for Scientific Research. RISE Research Institutes of Sweden AB provided additional funding. The Nils and Dorthi Troëdsson Foundation for Scientific Research supports an adjunct professorship for AS at KTH.

References

Alfredsson, P.H., Örlü, R., Segalini, A. A new formulation of the streamwise turbulence intensity distribution in wall-bounded turbulent flows. Eur. J. Mech. B-Fluid. Vol. 36, 167-175 (2012).

Dyverfeldt, P., Sigfridsson, A., Kvitting, J.P.E., Ebbers, T. Quantification of intravoxel velocity standard deviation and turbulence intensity by generalizing phase-contrast MRI. Magnet. Reson. Med. Vol. 56, 850-858 (2006).

Jäsberg, A. The flow behavior of fiber suspensions in straight tubes: new experimental techniques and multiphase modeling. Doctoral Thesis Department of Physics, University of Jyväskylä, 2007.

Drag reduction by polymer additives in turbulent fiber laden flow: effect of polymer concentration and pipe size

Mattia Simeoni[1], Marina Campolo[2], Alfredo Soldati[1]

[1] *Department of Electrical, Management, and Mechanical Engineering, University of Udine, Udine, Italy*
[2] *Department of Chemistry, Physics, and Environment, University of Udine, Udine, Italy*

Keywords: fiber laden flow, polymers, drag reduction

Abstract

Fiber laden flows are used in many industrial processes (e.g. pulp and paper, wood processing). Depending on fiber characteristics (length, diameter, aspect ratio) and concentration in the flow, fiber transport mode changes from dilute (evenly distributed fibers) to semi dilute or dense. Each transport mode corresponds to different values of pressure drop and energy required to maintain the flow. It is known from 1950s that polymers added in small quantity to the flow can be used as drag reducer (flow enhancer) to contain the pressure drop and/or to improve flowability. In this work we investigated drag reduction by polymer additives in fiber laden flows considering two different pipe diameters (50 and 30 mm). Tests have been performed to evaluate drag reduction produced by polymer in pure water and in fiber laden flow for different values of polymer concentration. The flow was fully turbulent with Reynolds number up to 150,000.

Introduction

Fiber laden flows are used in many industrial processes (e.g. pulp and paper, wood processing). The amount of energy required to transport such kind of flows, depends on the fiber's characteristics and transport mode [1]. For particular conditions, fiber them self may act as drag reducers whereas in other occasions, drag reducing polymers may be added to the flow to improve flowability.
The use of polymer additives is common in civil and process engineering and in many food, pharmaceutical, and biomedical processes [2]. When added to a turbulent flow, polymers are subject to local flow conditions and undergo tumbling, flow orientation, chain stretching, and relaxation. The net effect of all these conformational changes appears as an intrinsic elastic stress which alters the flow field and the dynamics of near wall turbulent structures which control the momentum transfer to the wall [3]. The macroscopic result is a dramatic reduction of the friction factor.
The object of this work is to build a self-consistent data set investigating turbulent drag reduction for fiber laden flows in different pipe diameters (30, 50 mm i.d.) with the final aim of validating the new theoretical correlation and identify scale effects which will allow to improve drag redaction prediction. Nylon fiber (L/D=120, d_f=20 μm) were used in different concentrations (0.25, 0.5, 0.75%) in pure fiber flows and in addition with Polyethylene Oxide (PEO) (0.5, 1, 5 ppm). Volumetric flowrate and pressure drop have been measured for each test condition.

Nomenclature

$\Delta p/L$	Pressure drop per unit length (mbar/m)
Q	Volumetric flowrate (m^3/h)
d_f	Fibers diameter (μm)

Subscripts

f	Fiber

Experimental Facility

The experimental facility consists in two acrylic pipes: one 30 mm i.d., 8 m in length, the other, 50 mm i.d., 12 m in length. Each pipe section (4 m long) is equipped with pressure ports, allowing the measurement of the pressure drop along different pipe sections. A Pedrollo NGA1A (maximum flowrate 350 litres/min) centrifugal pump drives the fluid from a 300 litres tank trough the experimental rig and back to the tank. Müller differential pressure transducers have been used: 700 mbar full scale, adjustable span, 0.075% of the span accuracy. Volumetric flowrate has been measured by means of an Endress&Hauser Proline Promag 10W electromagnetic flowmeter, adjustable span, 0.5% of the read value accuracy. Polymer has been injected into the flow after the centrifugal pump by means of a Medrad Envision CT Injector.

Results and Discussion

In Table 1, the experimental matrix is presented.

Fibers, L/D=120, d_f=20 μm	C=0.25, 0.5, 0.75%
Polymer, PEO	C=0.25, 0.5, 1, 5 ppm
Fiber + Polymer	0.25, 0.5, 0.75% + 0.5, 1, 5 ppm

Table 2: Experimental matrix.

Figures 1 and 2 present the results of pressure drop per unit length with respect to volumetric flowrate, for fiber flow in three different concentrations, in both 30 and 50 mm pipes. As may be seen, drag reduction already occurs for the pure fiber flow but just in the smaller pipe. No effects with increasing concentration have been reported.

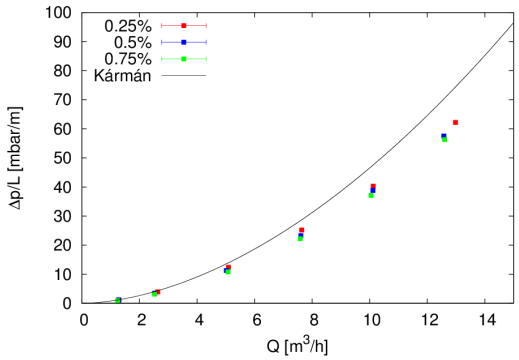

Figure 1: Fiber laden flow, 30 mm pipe, different concentrations

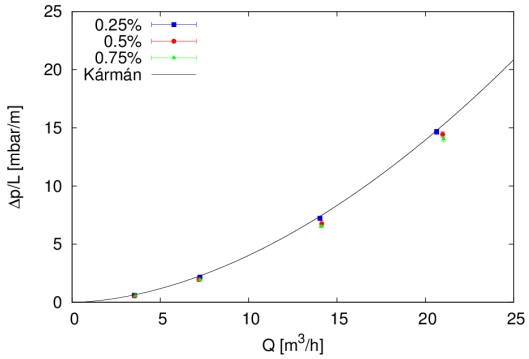

Figure 2: Fiber laden flow, 50 mm pipe, different concentrations

Regarding polymer flows, figures 3 and 4 show the results of the pressure drop for polymer injection at different concentration and for both pipes. Drag reduction increases with increasing polymer concentration and Reynolds number.

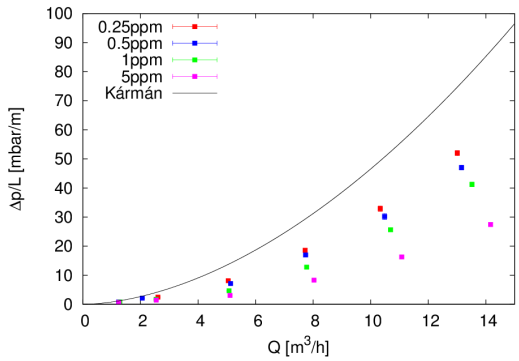

Figure 3: Polymer drag reduction in 30 mm pipe, different concentrations

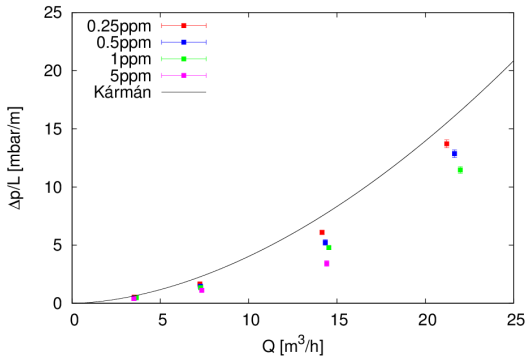

Figure 4: Polymer drag reduction in 50 mm pipe, different concentrations

Drag reduction effect, at constant concentration, is higher in the smaller pipe.
When added to the fiber laden flow, polymers increase (30 mm pipe) or establish (50 mm pipe) drag reduction effect reducing the pressure drop with respect to the pure fiber flow (figures 5 and 6).

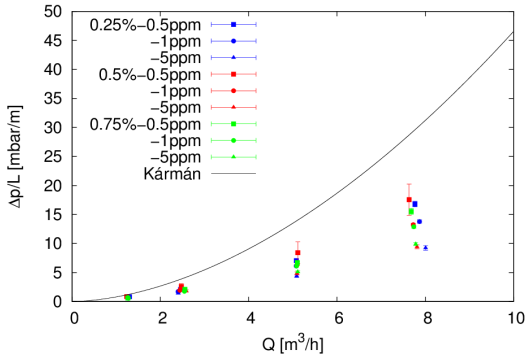

Figure 5: Effect of polymer concentration on fiber laden flow for different concentrations in 30 mm pipe.

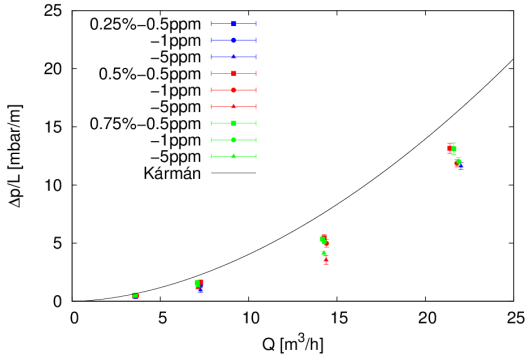

Figure 6: Effect of polymer concentration on fiber laden flow for different concentrations in 50 mm pipe.

As already mentioned, drag reduction effect increases with increasing polymer concentration and Reynolds number and the effect is perceived more in the smaller pipe.

Conclusions

Even if a small drag reduction effect has been reported in fiber laden flows, polymers have been proved to reduce friction drag even in fiber flows; efficiency increases with increasing concentration and Reynolds number. Moreover, drag reduction effect have been proved to be higher in smaller pipe diameters. Scale effects should be investigated in more detail to obtain scaling laws for drag reduction prediction.

References

[1] Vaseleski, R. C. & Metzner A. B. 1974 “Drag reduction in turbulent flow of fibre suspension”, AIChE Journal, 20/2, 301-306.

[2]White, C. M., and Mungal, M. G., 2008, “Mechanics and Prediction of Turbulent Drag Reduction With Polymer Additives,” Annu. Rev. Fluid Mech., 40, pp.235–256.

[3] Kim, K., and Sureshkumar, R., 2013, “Spatiotemporal Evolution of Hairpin Eddies, Reynolds Stress, and Polymer Torque in Polymer Drag-Reduced Turbulent Channel Flows,” Phys. Rev. E, 87(6), p. 063002.

Polymer-fiber laden flows in pipes of different diameters

Lawrence C. Edomwonyi-Otu[1] Mattia Simeoni[2], Panagiota Angeli[1], Marina Campolo[2]

[1]*Department of Chemical Engineering, University College London, London, United Kingdom*
[2]*Department of Chemistry, Physics and Environment, University of Udine, Udine, Italy*

Keywords: Drag reduction, synergy, polyamide fibers, polymers,

Abstract

An important objective of the Cost Action FP1005 is the acquisition of data for fiber and polymer induced drag reduction for setting benchmarks for future studies. In this work, drag reduction in 30mm and 50mm internal diameter acrylic pipes for single phase water flows were measured. Polyamide nylon fibers were used as drag reducing agents (DRA) and then combined with polyethylene oxide (PEO: mol. Wt 8 x 10^6g/mol) in a synergistic system in both pipe sizes. Maximum polymer and fiber concentration tested were 5ppm and 0.75wt% respectively. Results showed that for a fixed fiber concentration, drag reduction reduced with increasing Reynolds number, while it increased with increasing fiber concentration. A synergistic effect of the combination of fibers and polymers was observed at low fiber concentrations and Reynolds numbers.

Introduction

The need to optimize energy efficiency in fluid flow both in the chemical and paper industries has been highlighted since Toms, (1948) report. Since then numerous works have been reported on the effectiveness of minute concentrations of some polymeric materials in reducing the frictional drag in fluid systems both in single and multiphase flows (Abubakar et al., 2014a, 2014b; Edomwonyi-Otu et al., 2015; Virk, 1975). The use of fibers in drag reduction, though not as effective as polymers, has also been reported (Kulicke et al., 1989; Sharma et al., 1978). Delfos (Delfos et al., 2011) showed that maximum drag reduction decreases with fiber length and is not dependent on fiber diameter, and concluded that based on their findings, the application of fiber induced drag reduction for natural gas transport applications seemed unrealistic and that further work with more detailed experimental techniques were needed. Some investigators have reported the combination of polymers and fibers in drag reduction with a synergistic effect that surpasses the sum of the drag reduction if either is used alone (Doulah, 1981; Kale and Metzner, 1976; Metzner, 1977). This synergistic effect in drag reduction has not been given considerable attention as well as fibers applications when compared to polymer solutions. In this work, preliminary tests in water for the drag reducing effect of the combination of polyethylene oxide and polyamide fibers in pipes of different diameter are carried out. The aim is the acquisition of data for fiber and polymer induced drag reduction for setting benchmarks for future studies.

Nomenclature

Wt%	Weight percent
PEO	Polyethylene oxide
HPAM	Hydrolysed polyacrylamide
MDRA	Maximum drag reduction asymptote
DR	Drag reduction
Ppm	Parts per million
L/D	Length to diameter (aspect) ratio
Re	Reynolds number

Subsripts

p	polymer
P+f	Polymer + fiber

Experimental Facility

Tests were performed at the University of Udine where two new testing loops (pipes with 3 cm and 5 cm internal diameter) have been built to test the effect of drag reducing polymers in different size pipes. In particular, tests have been performed using (i) aqueous solution of PEO, (ii) aqueous solution of long Nylon fibers and (iii) aqueous solution of PEO with long Nylon fibers. The flow rate in each loop was changed to span a range of values of the Reynolds number and to evaluate changes in the friction factors. Different concentrations of the polymer, fibers and polymer + fibers were equally tested. Table 1 shows the test materials and conditions in the course of these experiments.

Table 1 Flow properties and conditions

Test fluid	Water @ 20°C
Polymer and tested concentrations	PEO; Mol. wt. 8 x10^6g/mol 0.25ppm, 0.5ppm, 1ppm, and 5ppm
Fibers and tested concentrations	Polyamide nylon fibers; L/D = 120 0.25wt%, 0.5wt%, and 0.75wt%
Pipe sizes	30mm and 50mm ID
Reynolds No.; 30mm 50mm	 15000, 30000, 60000, 90000, 120000, and 150000 25000, 50000, 100000, and 150000

Results and Discussion

Figures 1 and 2 shows the result of the drag reduction (DR) by fibers and fibers + PEO for the two pipe sizes at different concentrations. The y-axis of figures 1 and 2 b–d are shown as the difference between the drag reduction by polymers (DR_p) and those by the combination of fibers and polymers (DR_{p+f}). It can be observed from Figures 1a and 2a that the fibers produced drag reduction at the different concentrations but not in the same degree with polymers even in very small concentrations as already discussed.

Drag reduction is seen to reduce with increased Reynolds number for fixed fiber concentration, particularly in the 50mm pipe. The trend observed in the 30mm pipe was not consistent while in the 50mm pipe the DR at 0.75wt% fiber concentration was almost same for all Reynolds numbers and then reduced significantly at Re = 150000.

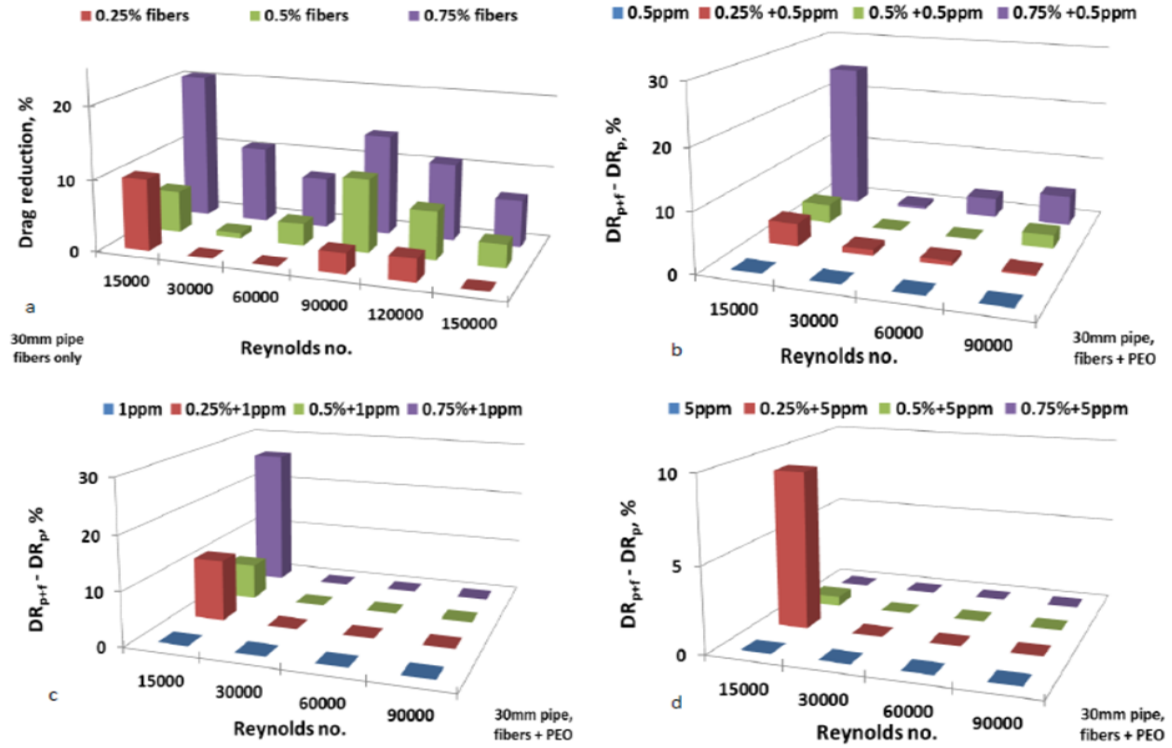

Figure 1 Drag reduction by fibers vs Reynolds no. in 30mm pipe for different polymer concentrations.

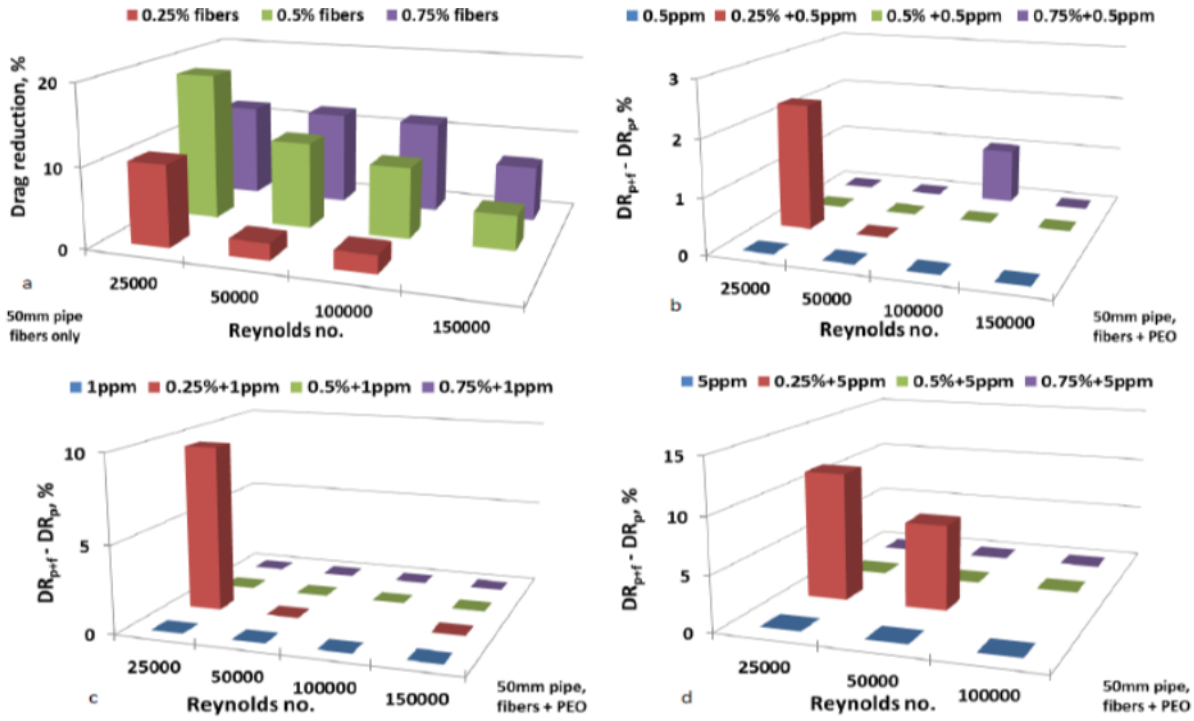

Figure 2 Drag reduction by fibers vs Reynolds no. in 50mm pipe for different polymer concentrations.

Drag reductions of over 10% are observed in some cases, although not up to the levels reported by Metzner and Kale (Kale and Metzner, 1976, 1974; Metzner, 1977) who used both asbestos as well as nylon fibers but at different

concentrations from those in this study. The fibers used in these experiments are promising for possible commercial applications. The reduction in DR with increase in Reynolds number may be due to collisions of fibers in turbulent flows leading to some energy losses (Doulah, 1981). It may also be connected with the fact that at high Reynolds numbers, the fiber entanglements straighten out under inertia effects in the axial flow direction thereby limiting fiber-fluid interactions. Figures 1(b-d) and 2(b–d) shows the comparison of the drag reduction by polymers to drag reduction by the combination of polymers and fibers, in order to see the synergistic effect (if any) of the combinations. It should be noted that in the cases (polymers + fibers) where there are no rising bars, they are in the negative, implying that the addition of fibers to polymer resulted in a reduction of the drag reduction due to the polymers alone. It can be observed that for both pipe sizes, few cases exists where the combination of fibers and polymer resulted in an increase in drag reduction particularly for fiber concentration of 0.25% and at Reynolds numbers of 15000 and 25000 for 30mm and 50mm pipes respectively, corresponding to a velocity of 0.5m/s. These results at the lower Reynolds number for the combination are corroborated by those from Figures 1a and 2a as already discussed. Clearly, the combination appears more favorable at low Reynolds numbers and low fiber concentrations particularly in the bigger 50mm pipe, while higher fiber concentrations give better drag reduction for fiber only systems. The results obtained for some of the combination systems are not as high as those reported for asbestos (L/D = 350) + polymer combinations (Kale and Metzner, 1974; Metzner, 1977). Metzner (Metzner, 1977) studied asbestos and PEO (150ppm) combinations as well as nylon fibers (L/D 100) and PEO combinations, and he reported an increase of drag reduction. He also reported drag reduction increase with increasing asbestos concentrations (200wppm to 800wppm) at fixed polymer concentration (150ppm). These conditions are however different from those in the current study.
The results shown in this brief study are promising and more work needs to be done to establish the optimum conditions for this nylon fibers and its combinations with polymer for optimum synergistic effects in drag reduction.

Conclusions

Preliminary tests on the drag reduction effects of polymers and nylon fibers have been carried out in pipes of 30mm and 50mm internal diameters. From the results the following conclusion can be reached;

- Drag reduction increases with Reynolds number, polymer concentration and with reduced pipe diameter.
- For fiber systems, drag reduction increases with concentration and reduces with increased Reynolds number
- Lower fiber concentration and Reynolds number enhances the synergy between polymer and fiber in a combined system

Acknowledgements

This work was funded by a short term scientific mission (STSM) grant from European Cooperation in Science and Technology (E-COST) Action FP1005. L.C Edomwonyi-Otu acknowledges the Petroleum Technology Development Fund (PTDF) Nigeria, for his studentship.

References

Abubakar, A., Al-Hashmi, A.., Al-Wahaibi, T., Al-Wahaibi, Y., Al-Ajmi, A., Eshrati, M., 2014a. Parameters of Drag Reducing Polymers and Drag Reduction Performance in Single-Phase Water

Abubakar, A., Al-Wahaibi, T., Al-Wahaibi, Y., Al-Hashmi, A.R., Al-Ajmi, A., 2014b. Roles of drag reducing polymers in single- and multi-phase flows. Chem. Eng. Res. Des. 92, 2153–2181.

Delfos, R., Hoving, J., Boersma, B., 2011. Experiments on drag reduction by fibres in turbulent pipe flow Background, in: Euromech Meeting 513. Udine, Italy, pp. 1–27.

Doulah, M.S., 1981. Mechanism of drag reduction in turbulent pipe flow by the addition of fibers. Ind. Eng. Chem. Fundam. 20, 101–102.

Edomwonyi-Otu, L.C., Chinaud, M., Angeli, P., 2015. Effect of drag reducing polymer on horizontal liquid-liquid flows. Exp. Therm. Fluid Sci. 64, 164–174.

Kale, D., Metzner, A., 1976. Turbulent Drag Reduction in Dilute Fiber Suspensions : Mechanistic Considerations. AIChE J. 22, 669–674.

Kale, D.D., Metzner, A.B., 1974. Turbulent Drag Reduction in Fiber-Pol ymer Systems: Specificity Considerations. AlChE J. 20, 1971–1972.

Kulicke, W., Kotter, M., Grager, H., 1989. Drag Reduction Phenomenon with Special Emphasis on Homogeneous Polymer Solutions. Adv. Polym. Sci. 89, 1–68.

Metzner, A.B., 1977. Polymer solution and fiber suspension rheology and their relationship to turbulent drag reduction. Phys. Fluids 20, S145.

Sharma, R.., Seshadri, V., Malhotra, R.C., 1978. Turbulent Drag Reduction by Injection of Fibers. J. Rheol. (N. Y. N. Y). 22, 643.

Toms, B., 1948. Some observations on the flow of linear polymer solutions through straight tubes at large Reynolds numbers., in: International Congress on Rheology. North Holland publication company, Amsterdam, pp. 135–141.

Virk, P.S., 1975. Drag Reduction Fundamentals. AlChE J. 21, 625–656.

Strategy in modelling irregular shaped particle behaviour in confined turbulent flows

M. Sommerfeld[1,2], S. Lain[2] and Z. Qadir[1]

[1]*Zentrum für Ingenieurwissenschaften, Martin-Luther-Universität Halle-Wittenberg, D-06099 Halle/Saale, Germany*
[2] *Universidad Autónoma de Occidente, Department of Mechanical Engineering, Cali, Colombia*

Keywords: non-spherical particles, irregular shape, Euler/Lagrange approach, statistical treatment of irregular structure, fluid forces, resistance coefficients, Lattice-Boltzmann method, wall collisions, experiments

Abstract

Lagrangian tracking of non-spherical particles with certain shapes is mostly performed by additionally solving for the orientation of particles in the flow and using resistance coefficients (i.e. drag, lift and torque) which depend on this orientation. For that in many cases theoretical results for Stokes flow around such particles are used. In practical situations where irregular shaped non-spherical particles such an approach cannot be adopted since the particles have mostly a statistical distribution of shape and hence it is difficult to define a major axis of the particles. The new approach developed here is based on a statistical treatment of the fluid forces and moments acting on the particles as well as the wall collision process in order to mimic their stochastic nature. The required probability distribution functions (PDF`s) for the resistance coefficients were derived by applying direct numerical simulations (DNS) based on the Lattice-Boltzmann method (LBM). The PDF`s for the wall normal and parallel restitution ratios were derived based on an experiments recording the wall impact of irregular shaped particles using high-speed imaging. Preliminary Euler/Lagrange calculations applying these statistical models were conducted for a particle-laden horizontal channel flow.

Introduction

The handling of powders though transportation by a fluid (i.e. gas or liquid) is an important process in numerous industrial and technical areas. These flows are mainly confined flows as for example in hydraulic or pneumatic conveying and in fluidized beds. Hence, particle motion is strongly governed by fluid transport, including turbulence (Sommerfeld et al. 2008) as well as wall collisions (Sommerfeld 1998, Sommerfeld 2004). In most applications the particles are non-spherical having either a regular shape (e.g. fibres, cylinders, granulates or disc-like particles) or a completely irregular structure such as quartz sand. In most numerical calculations conducted for such particle-laden flow systems by either the Euler/Euler or Euler/Lagrange approach, where particles are treated as point masses, it is assumed that they are of spherical shape. This is mainly associated with the fact that fluid forces acting on non-spherical particles, especially for larger particle Reynolds numbers, are to a large extent unknown. Only in a few studies direct numerical simulations (DNS) are being used for deriving correlations for the resistance coefficients (i.e. drag, lift and torque) of regularly shaped non-spherical particles (Hölzer and Sommerfeld 2009, Zastawny et al. 2012). However, such simulations are very time consuming due to the large parameter space which has to be considered. Having this information, Euler/Lagrange calculations may be conducted by additionally solving for the angular orientation of the particles in the flow (see e.g. van Wachem et al. 2015) and using correlations for the orientation-dependent resistance coefficients (Table 1). Knowing the particle orientation the wall collision process may be also calculated by solving the impulse equations in connection with Coulomb's law of friction (Sommerfeld 2002).

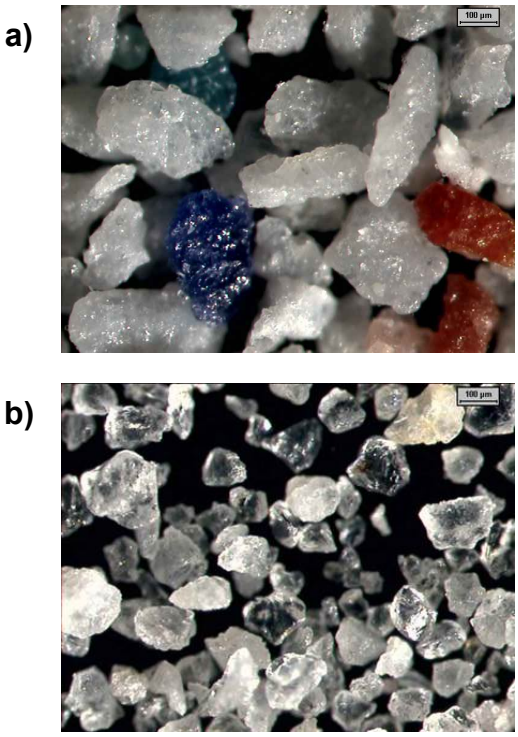

Figure 1: Photographs of irregular shaped particles; a) Duroplast particles volume equivalent mean diameter 240 μm; b) Quartz sand volume equivalent mean diameter 185 μm (Kussin 2003)

Lagrangian treatment of non-spherical particles	
Regularly shaped non-spherical particles	**Irregular non-spherical particles**
Deterministic tracking of particles, new location, linear and translational velocities	Stochastic tracking of particles, new location, linear and translational velocities
Requires additionally tracking of the particle orientation using Euler Parameters or quaternions	Determine the instantaneous values of the resistance coefficients from a-priory determined distribution functions (random process), e.g. by Lattice-Boltzmann simulations
Particle orientation-dependent resistance coefficients are required	Apply these random resistance coefficients in the equation of motion each time step
Solving the impulse equations for non-spherical particles considering particle orientation (Sommerfeld 2002)	Calculate the particle velocity change during a wall collision process from measured distribution functions of the restitution ratios

Table 1: Summary of deterministic and statistical modelling approaches for simulating non-spherical particles in the frame of a Lagrangian approach.

However, if the particles are irregular in shape, as illustrated in Fig. 1 for Duroplast particles (number mean diameter of 240 µm) and quartz sand (number mean diameter of 185 µm) they generally have a distribution of shapes and it is difficult to define any specific major axis of the particles. Hence, the tracking of particle orientation for such particles is not very meaningful.
Consequently, in this work a statistical approach is suggested (Table 1) in order to model the behaviour of irregular shaped particles in confined turbulent flows. This includes modelling of the stochastic nature of fluid dynamic forces acting on the particles and of the wall collision process.

Fluid Forces on Irregular Particles

Regarding the flow resistance coefficients first direct numerical simulation (DNS) based on the Lattice-Boltzmann method (LBM) were conducted for irregular particles immersed into a laminar plug flow. The applied in-house code uses a local grid refinement around complex particle structures. Moreover, curved wall boundary conditions are applied for the bounce-back condition and in order to obtain the momentum exchange between fluid and particles (Dietzel and Sommerfeld 2013). Prior to the flow simulations irregular particles were randomly generated by first lumping together a certain number of small spherical particles to form some kind of agglomerate. Around this structure a convex hull was wrapped (Dietzel and Sommerfeld 2013). The number and size of the core particles was selected in such a way to obtain an irregular particle with a hull volume yielding a volume equivalent diameter of about 100 µm. The sphericity of the particles was selected to be in the range of 0.86 to 0.89, which is defined as the surface of the volume equivalent sphere with the hull volume divided by the hull surface. Hence the selected sphericity is in the range of the measured value for the quartz particles (see Fig. 1 b).

For a large number of particle orientations with respect to the oncoming flow (i.e. 71) and for four particles with different shape but about the same sphericity (Fig. 2), the drag, lift and torque coefficients were calculated. From these results distributions of the resistance coefficients were derived regardless of their orientation with respect to the oncoming flow for particle Reynolds numbers between 1 and 200.

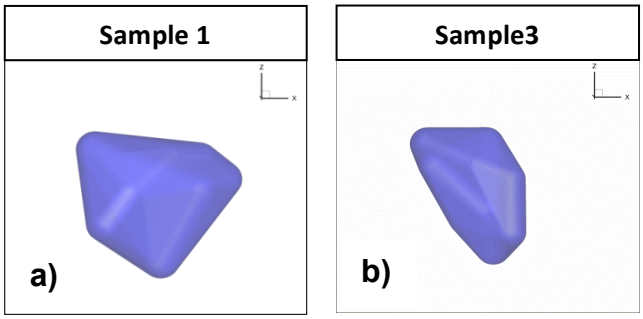

Figure 2: typical irregular shaped particles considered for the LBM simulations a) $D_{VES,hull}$ = 102 µm, ψ = 0.86; b) $D_{VES,hull}$ = 105 µm, ψ = 0.88.

These resulting distributions were reasonably well described by normal distribution functions (Qadir and Sommerfeld 2013). Hence for the use in Lagrangian calculations the mean values and the standard deviations were specified as shown in Fig. 3 and could be approximated by appropriate fitting functions (Lain et al. 2014). The drag coefficient in dependence of particle-Reynolds number was found to be slightly higher than the values obtained by the Schiller and Naumann (1933) correlation for spheres and also that for non-spherical particles with the present sphericity proposed by Haider and Levenspiel (1983).

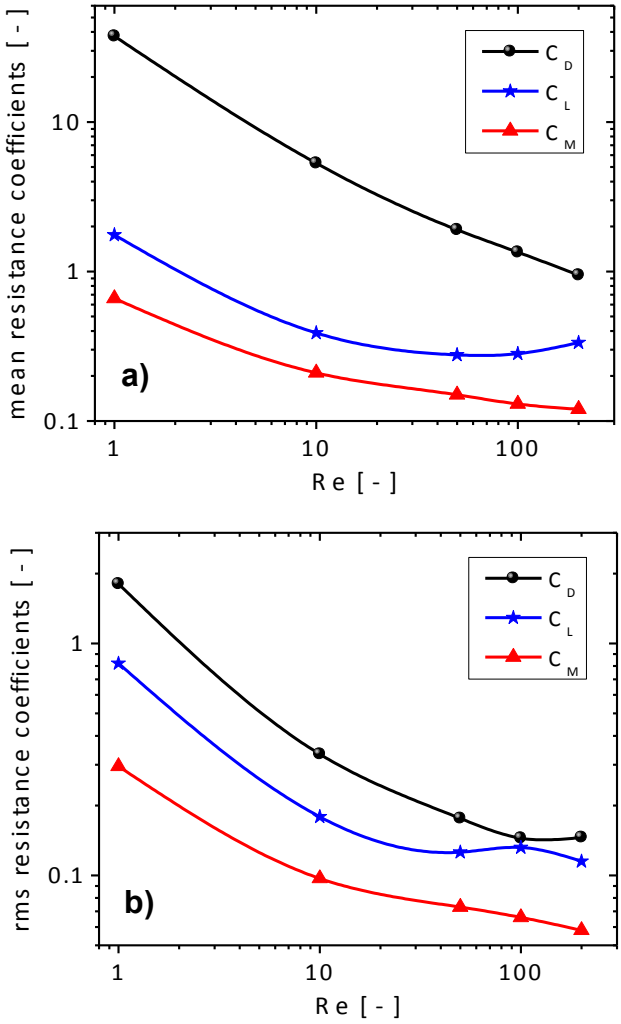

Figure 3: Simulation results for the resistance coefficients (CD drag, CL lift and CM moment) of irregular particles with sphericity $\phi \approx 0.875$; a) mean values, b) rms values.

Wall Collisions of Irregular Particles

Since confined particle-laden flows are strongly governed by wall collisions a corresponding model had to be developed to be applied in the frame of Euler/Lagrange calculations. For that purpose an experimental facility was set-up which allows analysing irregular particle wall collisions at wall collision angles between 5° and 85° (Fig. 3). The particles were shot against the target with velocities lying between 8 and 21 m/s (i.e. depending on impact angle) using pneumatic conveying through a narrow pipe. The wall collision history was recorded by two perpendicular arranged high-speed cameras applying a LED back-ground illumination. The irregular particles considered in the present study are those shown in Fig. 1, i.e. 240 µm Duroplast particles and 185 µm quartz sand). From a large number of events (typically around 100), distributions of the wall-normal and wall-parallel restitution ratios were evaluated which could be mostly approximated by normal distribution functions having a certain mean value and standard deviation. The mean value of the normal restitution ratio decreases continuously from about 1.5 at shallow impact angles towards about 0.4 at large impact angles. The standard deviation of the distributions (i.e. obtained for discrete impact angles) show large values at small impact angles which decrease towards normal impact. The tangential velocity restitution shows no strong variation up to an impact angle of 65° and may be assumed to be about 0.8, but then rapidly increases to about 2.0 at normal impact. In this latter range also the standard deviation of the tangential restitution increases remarkably. The high mean values of normal and tangential restitution and the large standard deviations in these regions are resulting from particle rotation. Unfortunately, the change of particle rotation during wall collision could not be determined for the irregular shaped particles. With these results a stochastic wall collision model was developed.

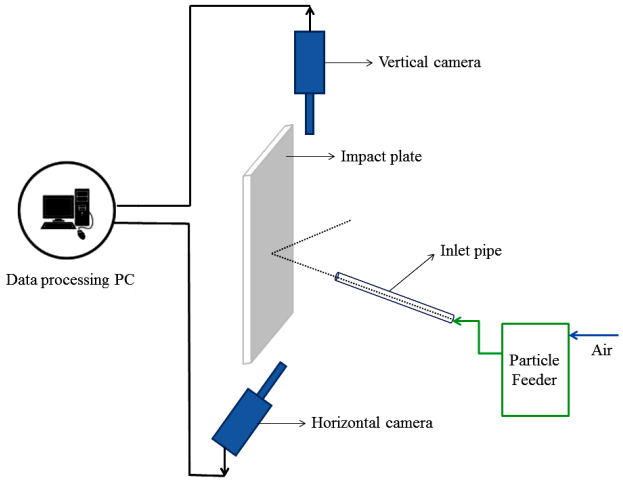

Figure 3: Facility for the experimental analysis of particle-wall collisions using two perpendicular arranged high-speed cameras (Photron High Speed Video Camera, FASTCAM SA4 RV operated at 60,000 fps).

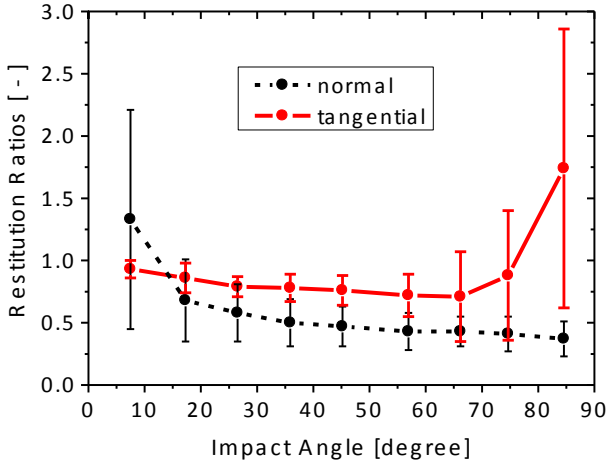

Figure 3: Measured restitution ratios normal and parallel to the wall, mean values and standard deviations for quartz particles.

Euler/Lagrange Calculations

In the next step the Euler/Lagrange approach, extended with the statistical tracking and wall collision models (see Lain et al. 2014), is validated based on the experiments of Kussin (2003) in a horizontal particle-laden channel flow of 6 m length (channel height 35 mm). In this work different kinds of regular and irregular shaped non-spherical particles were used. In the developed flow region (i.e. after about 5 m) particle concentration and velocity profiles were measured by an extended Laser-Doppler anemometer. Small tracer particle were added to measure also the air velocity in the presence of the particles. For the present simulations the quartz particles shown in Fig. 1 b) are considered and the result is compared in Fig. 4 and 5. The vertical profiles of the particle mass flux and the stream-wise particle velocity show no remarkable differences for the results obtained with the new statistical model and those assuming spherical particle as previously done (Lain and Sommerfeld 2008). Inter-particle collisions yield a slightly better dispersion of the particles which is obvious from the profiles of the particle mass flux.

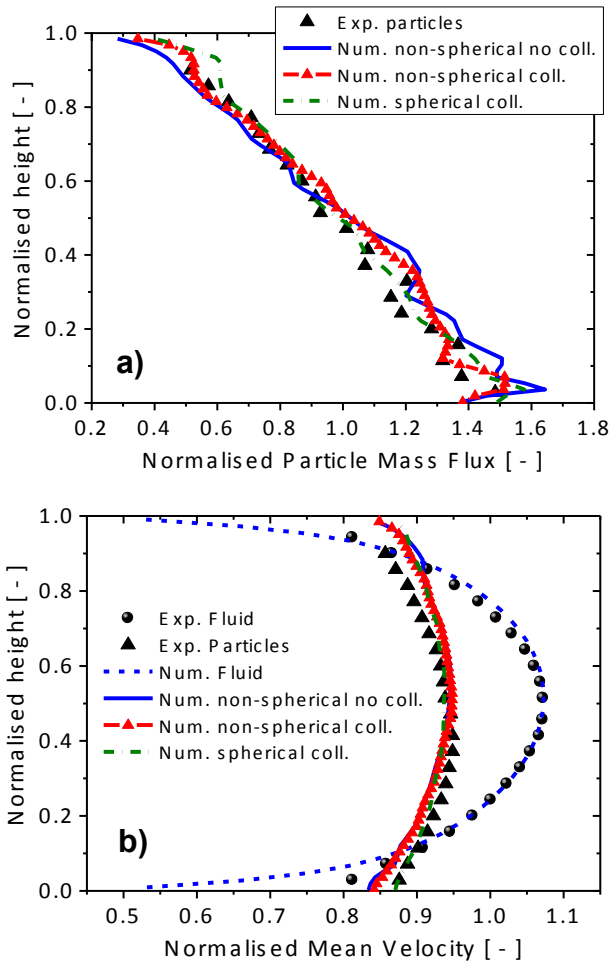

Figure 4: Comparison of Euler/Lagrange calculations with experiments using irregular quartz particles; a) particle mass flux normalised by the mean value; b) stream-wise velocities normalised by the average conveying velocity U_0 = 20 m/s (quartz particles 185 µm, mass loading ratio 0.1)

The vertical profiles of the particle velocity fluctuations (i.e. rms-values) show on the other hand considerable differences for the various calculations. The particle stream-wise rms velocity is with the statistical particle model remarkably higher than for fictitious simulations with spherical particles, especially near the lower wall. Thereby the new statistical treatment of particles yields better agreement with the measurements, although not yet perfect. Inter-particle collisions, although not very important for this low loading case, result in a bit more uniform rms profile.
The vertical component of the particle`s fluctuating velocity obtained with the statistical treatment of irregular particles in contrast shows a major reduction of the rms values compared to the sphere calculations. Consequently the agreement with the measurements becomes much better. Accounting for inter-particle collisions the particle`s fluctuating velocity becomes more isotropic, i.e. the vertical component is enhanced (Sommerfeld 1998).

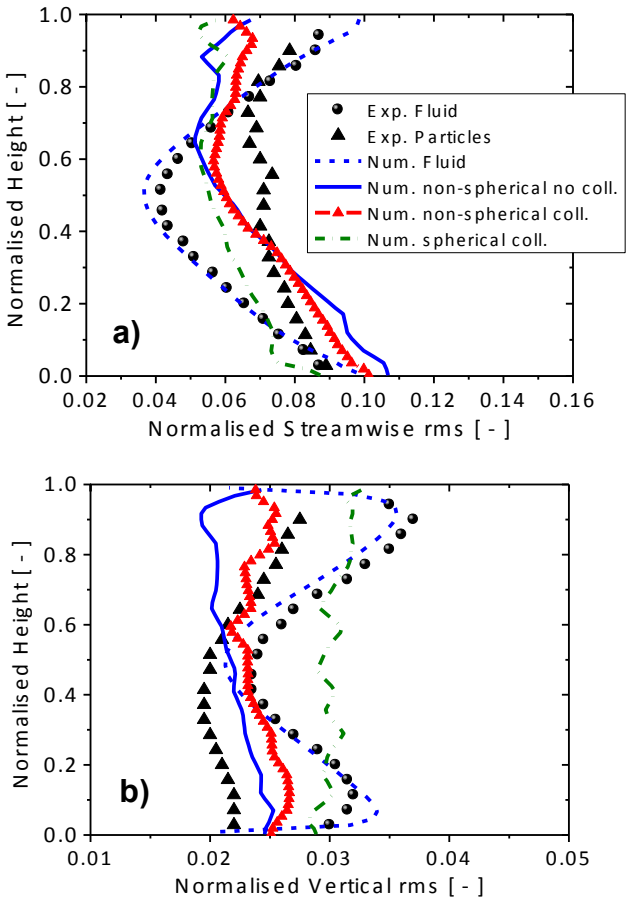

Figure 5: Comparison of Euler/Lagrange calculations with experiments using irregular quartz particles; a) stream-wise velocity fluctuation; b) vertical velocity fluctuation, both normalised by the average conveying velocity U_0 = 20 m/s (quartz particles 185 µm, mass loading ratio 0.1)

Conclusions

A statistical approach for modelling the behaviour of irregular shaped non-spherical particles in wall-bounded particle-laden turbulent flows by the Lagrangian approach is

suggested. This implies that PDF`s for the flow resistance coefficients (i.e. for drag, lift and torque) and for the change of particle velocity during wall impact were used to draw instantaneous values at each time step of particle tracking or at the instance of wall collision. The LBM as a DNS tool was used to determine the PDF`s of the resistance coefficients for irregular shaped particles in dependence of particle Reynolds number, which could be represented by normal distributions to a large extent. For obtaining the PDF`s of the restitution ratios describing the change of the velocities of irregular shaped particles during wall collisions experimental studies could be done successfully for different particle types using high-speed cameras. Eventually, a comparison of Euler/Lagrange calculations including the new statistical model with experiments in a horizontal channel showed surprisingly good agreement. In comparison with calculations assuming spherical particles it was found that mainly the fluctuating velocities are affected by the introduced statistical models for irregular particles. In further studies other types of irregular particles will be considered.

Acknowledgements

The financial support of the DFG (Deutsche Forschungsgemeinschaft, Germany) under contract SO204/39-1 and the support of DAAD (University Halle, Germany) & Colciencias (Universidad Autónoma de Occidente, Cali, Colombia) through the German-Colombian exchange mobility program are gratefully acknowledged.

References

Dietzel, M. and Sommerfeld, M.: Numerical calculation of flow resistance for agglomerates with different morphology by the Lattice-Boltzmann Method. Powder Technology, Vol. 250, 122–137 (2013)

Haider, A. and Levenspiel, O. Drag coefficient and terminal velocity of spherical and nonspherical particles. Powder Technology, Vol.58, 63-70 (1983)

Hölzer, A. and Sommerfeld, M.: Lattice Boltzmann simulations to determine drag, lift and torque acting on non-spherical particles. Computers and Fluids, 38, 572-589 (2009)

Kussin, J.: Experimentelle Studien zur Partikelbewegung und Turbulenzmodifikation in einem horizontalen Kanal bei unterschiedlichen Wandrauhigkeiten. PhD Thesis, Zentrum für Ingenieurwissenschaften, Martin-Luther Universität Halle-Wittenberg (2003)

Lain, S. and Sommerfeld, M.: Euler/Lagrange computations of pneumatic conveying in a horizontal channel with different wall roughness. Powder Technology, Vol. 184, 76-88 (2008)

Laín, S., Sommerfeld, M., Quintero, B. and Qadir, Z.: Modelling and computation of irregular non-spherical particles transport in confined turbulent flow. 13th International Conference on MULTIPHASE FLOW IN INDUSTRIAL PLANTS. Sestri Levante (Genova), Italy, September 17-19, 2014

Qadir, Z. and Sommerfeld, M.: Analysis of the fluid dynamic forces acting on irregular shaped paricles. Euromech Colloquium Small-Scale Numerical Methods for Multi-Phase Flows, 12M-ENSCBP, Pessac, France, August 28. – 30. 2013

Schiller, L. and Naumann, A.,: Über die grundlegende Berechnung bei der Schwerkraftaufbereitung. Verein Deutscher Ingenieure, Jahrg. 44, 318-320 (1933)

Sommerfeld, M.: Modelling and numerical calculation of turbulent gas-solid flows with the Euler/Lagrange approach. KONA (Powder and Particle), No. 16, 194-206 (1998)

Sommerfeld, M.: Analysis of collision effects for turbulent gas-particle flow in a horizontal channel: Part I. Particle transport. Int. J. Multiphase Flow, 29, 675-699 (2003)

Sommerfeld, M., van Wachem, B. and Oliemans, R.: Best Practice Guidelines for Computational Fluid Dynamics of Dispersed Multiphase Flows. ERCOFTAC (European Research Community on Flow, Turbulence and Combustion, ISBN 978-91-633-3564-8 (2008)

van Wachem, B., Zastawny, M., Zhao, F., Mallouppas, G.: Modelling of gas-solid turbulent channel flow with non-spherical particles with large Stokes numers. International Journal of Multiphase Flow 68, 80-92 (2015)

Zastawny, M., Mallouppas, G., Zhao, F. and van Wachem, B.: Derivation of drag and lift force and torque coefficients for non-spherical particles in flows. Int. J. Multiphase Flow, 39, 227-239 (2012)

Numerical simulations of finite-size non-spherical particles in shear flows

Mehdi Niazi[1], Pedro Costa[2], Wim-Paul Breugem[2] and Luca Brandt[1]

[1]*KTH Mechanics, Linné FLOW Centre, SE-100 44 Stockholm, Sweden*
[2]*Delft University of Technology, Laboratory for Aero and Hydrodynamics, Leeghwaterstraat 21, 2628 CA Delft, The Netherlands*

Keywords: spheroid particles, Immersed boundary method, numerical simulations

Abstract

The behavior of particles in a turbulent flow affects the global transport and rheological properties of the mixture. Suspensions of solid particles in a viscous liquid are of scientific and technological interest in a wide range of applications. In recent years much effort has been devoted to the development of an efficient method for the direct numerical simulation (DNS) of the motion of spherical rigid particles immersed in an incompressible fluid. However, the literature on non-spherical particle suspensions is quite scarce despite the fact that these are more frequent.
The overall goal of this study is to develop a numerical algorithm to simulate finite-size spheroid particles in shear flows to gain new understanding of the flow of particle suspensions in the transitional and turbulent regimes. In particular, we wish to understand the role of inertia and its effect on the flow behavior. For this purpose, DNS simulations with a direct-forcing immersed boundary method will be used with collision and lubrication models for particle-particle and particle-wall interactions.

Introduction

Many flows of industrial and geophysical interest involve the presence of a solid dispersed phase. Several efforts have therefore been devoted to develop numerical algorithms able to fully resolve the fluid-particle and particle-particle interactions in flow [1,2]. To limit ourselves to the previous studies relevant to this work, Uhlmann (2005) [3] proposed an Immersed boundary method to solve the particle-laden flows without the need of moving meshes. Breugem (2012) [4] improved the original method to a second order accuracy by adding a multi-direct forcing method and a retraction of the effective particle diameter by a fraction of the Eulerian grid spacing. Kempe et al. (2009) [5] proposed an extension of original method to ellipsoidal particles. However, a complete modeling of ellipsoidal particle with collision and lubrication is still rare in the literature. In this study the numerical improvements of Breugem (2012) [4] are used for ellipsoidal particles and an efficient method is proposed to model the collision and lubrication forces between ellipsoidal particles. The numerical scheme is validated against different test cases and the drafting-kissing-tumbling of sedimenting particle pairs is simulated for ellipsoidal particles to document the differences with the spherical particles.

Nomenclature

V_p	Volume of the particle
$\boldsymbol{U}_p$	Centre velocity of the particle
ρ_p	Mass density of the particle
$\boldsymbol{F}$	Force acting on the particle
$\boldsymbol{A}$	Rotation matrix
$\boldsymbol{I}_p$	Inertia Tensor
$\boldsymbol{\omega}$	Angular velocity of the particle
$\boldsymbol{r}$	Position vector
$\boldsymbol{T}$	Torque acting on the particle

Numerical Scheme

The same pressure-correction scheme as in Breugem (2012) [4] is employed to solve the Navier-Stokes equation with an extra term on the right hand side of the equations coming from the IBM force. This is active in the immediate vicinity of a particle surface to impose indirectly the no slip/no penetration condition; the fluid velocity is imposed to equal to the surface velocity of the particle ($\mathbf{U}p + \boldsymbol{\omega} \times \mathbf{r}$). A Lagrangian two-dimensional mesh attached to the surface of the object follows the motion of the particle. The equations of motion for the particles are also solved, where, unlike for spherical particles, the inertia tensor $\mathbf{I}_p$ is changing with orientation and therefore it is not constant in time.

$$\frac{d\,(\boldsymbol{I\omega})}{dt} = \boldsymbol{T} \qquad (\mathbf{1}\boldsymbol{a})$$

$$\rho_p V_p \frac{d\boldsymbol{U}_p}{dt} = \boldsymbol{F} \qquad (\mathbf{1}\boldsymbol{b})$$

To find the angular velocity $\boldsymbol{\omega}$ from the integrated impulse, $\mathbf{I}_p\boldsymbol{\omega}$, an iterative method similar to Kempe et al. (2009) [5] is used. This computes $\boldsymbol{\omega}^{\boldsymbol{n+1}}$ at each iteration and updates the new inertia tensor by:

$$\boldsymbol{I}_p{}^{n+1} = \boldsymbol{A}\,\boldsymbol{I}_p{}^{n}\,\boldsymbol{A}^{-1}$$

where the matrix $\mathbf{A}$ accounts for the rotation of the particle from the configuration in the previous time step to the current time step. The axis of rotation for $\mathbf{A}$ is the direction of $(\boldsymbol{\omega}^{n+1} + \boldsymbol{\omega}^{n})/2$ and the angle of rotation can be

calculated from $|(\boldsymbol{\omega}^{n+1} + \boldsymbol{\omega}^{n})/2|\Delta t$.

A soft sphere collision model and a lubrication model are considered for the particle-particle and particle-wall interactions. These are turned on as soon as the particle distance is below the grid size and when particles overlap [4]. The method proposed by Lin et al. (2006) [6] is used to compute the closest distance between two ellipsoids and the nearest points on the two objects. Spheroid particles are then approximated as spherical particles with radius of curvature corresponding to that of the closest points, with same mass as the whole particle. This implies that one needs to track of the radius of curvature at the closest points to the neighbour particles at each time step. Once the lubrication/collision occurs, the particle is treated as a sphere with the radius of curvature of the last time step before collision.

Results and Discussion

Two tests are performed to validate the code.

1) Jeffery orbit

Jeffery (1922) [7] calculated the analytical solution for the angular velocity $\boldsymbol{\omega}$ of spheroidal particles with $Re_p = 0$ in a simple shear flow. It can be found that the particle performs periodic orbits with a conserved quantity C, called the orbit constant, depending on initial conditions, and an equal rotation period for all orbits. The equations of motion for the spheroidal particles derived by Jeffery (1922) [7] have been widely used in the literature. In this study a prolate particle with aspect ratio of 2 is investigated in a plane Couette flow at $Re_p = 0.1$. The aspect ratio of a spheroid particle is defined as the ratio between the semi-major and the semi-minor axes. Fig.1 shows the results of this numerical test versus the analytical solution.

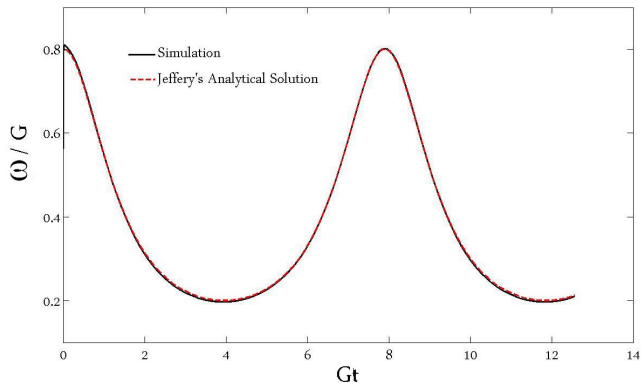

Figure 1: Numerical results compared to the analytical solution of Jeffery. G is the shear rate, used for non-dimensionalization

2) Oblate ellipsoid in cross-flow

Kempe et al. (2009) [5] investigated an oblate ellipsoid particle in a cross-flow as a test case for the fluid-solid coupling. They fixed the position of the particle center and allowed it to rotate around all three axes in a way that the particle's minor axis is in the direction of the flow. It is expected given an initial deflection, the particle oscillates around one of its major axes (depending on the plane of deflection) and reaches an equilibrium state where its minor axis is aligned with the flow direction. Indeed, it was also observed by Feng et al. (1994) [8] that prolate particles fall with their major axis perpendicular to the direction of the flow. For higher ratios of particle to fluid density the oscillating period and the magnitude of oscillation increases. Kempe et al. (2009) [5] performed several simulations at different density ratios at $Re_p = 100$ and aspect ratio of 2.5. In this study the density ratio of 8 is investigated to validate the code against the results of Kempe et al. (2009) [5]. Since in this study a multi-direct forcing method is used, it can be expected that the results are not the same as the ones in Kempe et al. (2009) [5]. Therefore, In order to have a better comparison another simulation of the same case is also performed without the use of multi-direct forcing. The results, demonstrated in fig.2, reveal the improvements due to the multi-direct forcing.

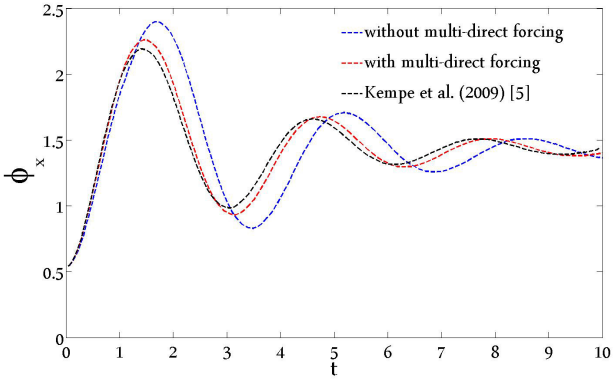

Figure 2: Rotation angle around x-axis versus time for density ratio of 8, $Re_p = 100$ and the aspect ratio of 2.5.

In addition to the validations, we study the drafting-kissing-tumbling of prolate/oblate particles and examine the differences with the spherical particles. Sedimenting particles, also in suspension [9], display pair interactions leading to large increase of the falling speed of the pair, which leads to highly intermittent behaviour in suspensions. We observe that the behavior of particles varies enormously with the initial orientation and the distance between the two particles falling in the wake of each other. Fig.3a-d reveals the most probable case, in which the major axis of the prolates is perpendicular to the direction of gravity. In this simulation, particles are falling in the y direction and the major axis of the particles is aligned with the horizontal z direction. Fig.3a indicates the initial position of the two particles. The upper particle falls at higher velocity in the wake of the leading one and the two therefore touch each other at a later time, as displayed in Fig.3b. When the particles touch each other they cannot have an angular velocity around the x-axis due to the collision forces. However, small disturbances that can be triggered by the collision give a small relative angular velocity around the y-axis to the leading particle. This creates an initial gap where high-pressure flow can penetrate and increase the particle counter rotation around the y-axis, as shown in fig3.c. The prolate particles continue their rotation until the red and the blue end of the particles, as depicted in the figure to help visualization, become almost aligned. At this point, again, the flow in the tiny gap tends to change the direction of the counter rotation of the particles shown in fig.3d. The mentioned counter rotations

change slightly the position of the centres, allowing the particles to enter the tumbling mode around their major axes faster. Interestingly, these rotations are absent for the spherical particles, delaying the tumbling motion. Numerical results of this study also confirm that the prolate particles enter the tumbling mode sooner than the spherical particles.

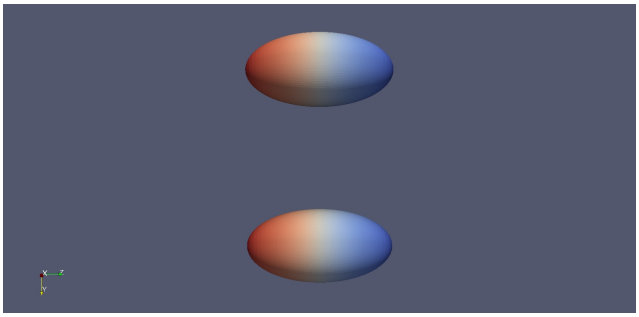

(a)

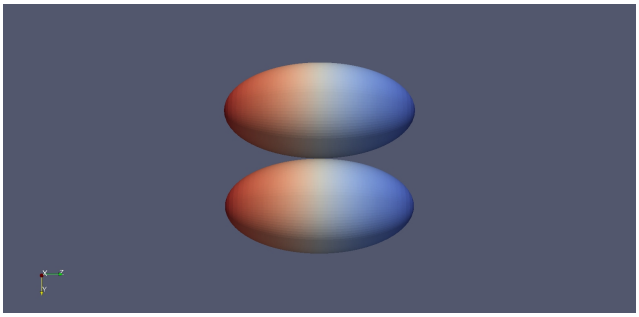

(b)

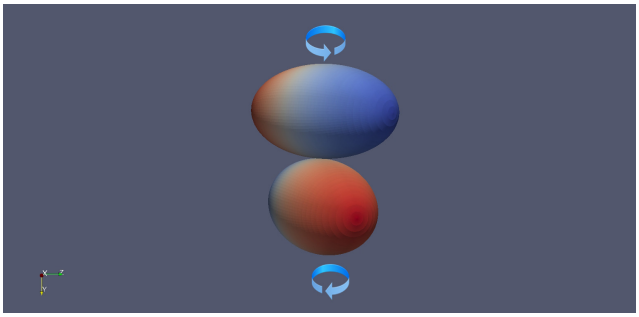

(c)

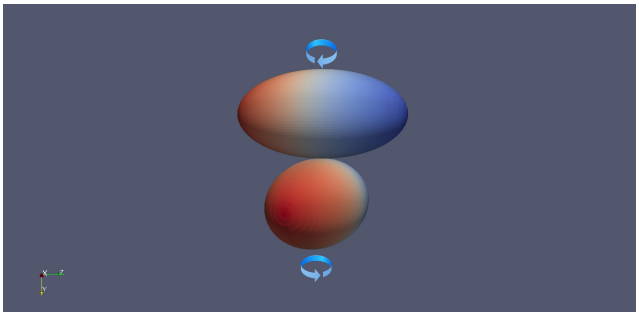

(d)

Figure 3: Time sequence of the sedimentation of prolate particles of aspect ratio 2 falling on each other wake.

Conclusions

We developed a numerical algorithm aiming to simulate suspensions of non-spherical particles in laminar and turbulent flows. The Immersed Boundary Method used in [1,2] is extended to account for spheroids particles: the Lagragian mesh attached to the particles is deformed into spheroids and collision/lubrication models based on the local radius of curvature at the contact points developed.
The code is fully parallel and tested on thousands of cores. We validated the new implementation against the analytical Jeffery orbits in the limit of creeping flow, Reynolds number going to zero, and against results of the rotation of an oblate sedimenting particle.
As a first step to understand the behaviour in suspension, we analyse pair-wise interaction between falling prolate particles, heavier than the surrounding fluid.
As final goal, we shall investigate the behavior of turbulent channel flow seeded with final size spheroid particles.

Acknowledgements

This work is supported by the European Research Council Grant No. ERC-2013-CoG-616186, TRITOS.

References

[1] Picano. F Breugem W.P. & Brandt. L. *Turbulent channel flow of dense suspensions of neutrally-buoyant spheres.* J. Fluid Mech., 764, 463-487, 2015.

[2] Lashgari. I , Picano. F , Breugem. W.P & Brandt. L. *Laminar, turbulent and inertial shear-thickening regimes in channel flow of neutrally buoyant particle suspensions.* Physical Review Letters, 113, 254502, 2014.

[3] Uhlmann. M. *An immersed boundary method with direct forcing for simulation of particulate flows.* J. Comput. Phys. 209, 448–476, 2005.

[4] Breugem. W.P. *A second-order accurate immersed boundary method for fully resolved simulations of particle-laden flows.* J. Comput. Phys. 231, 4469–4498, 2012.

[5] Kempe. T , Schwarz. S & Fröhlich. J *Modelling of spheroidal particles in viscous flows.* Proceedings of the Academy Colloquium Immersed Boundary Methods: Current Status and Future Research Directions , KNAW, Amsterdam, The Netherlands, 15–17 June 2009.

[6] Lin. A & Han. S.P. *On the Distance between Two Ellipsoids.* SIAM J. Optim., 13(1), 298–308,2006.

[7] Jeffery, G.B. *The motion of ellipsoidal particles immersed in a viscous fluid*. Proc. R. Soc. Lond. A 102, 161, 1922.

[8] Feng. J , Hu. H.H & Joseph. D.D. *Direct simulation of initial value problems for the motion of solid bodies in a Newtonian fluid. Part 1. Sedimentation.* J. Fluid Mech. 261,95–134,1994.

[9] Fornari. W , Picano. F & Brandt. L. *Sedimentation of finite-size spheres in quiescent and turbulent environments*. arXiv:1503.06148, 2015.

Cascade amplification of fluctuations

Michael Wilkinson[1], Marc Pradas[1], Robin Guichardaz[2], Alain Pumir[2]

[1]*Department of Mathematics and Statistics, The Open University, Walton Hall, Milton Keynes, MK7 6AA, England*
[2]*Laboratoire de Physique, Ecole Normale Supérieure de Lyon, CNRS, Université de Lyon, F-69007, Lyon, France*

Keywords: dynamical system, stable attractor, perturbation, instability

Abstract

We consider a dynamical system which has a stable attractor and which is perturbed by an additive noise. Under some quite typical conditions, the fluctuations from the attractor are intermittent and have a probability distribution with power-law tails. We show that this results from a cascade of amplification of fluctuations due to transient periods of instability.

Power-law fluctuations

In a one-dimensional example the equation of motion might be:

$$\dot{x} = v(x,t) + \sqrt{2D}\eta(t) \qquad (1)$$

where $\eta(t)$ is a white noise signal (defined by (2) below) and D is the diffusion coefficient of the corresponding Brownian motion. We shall be primarily concerned with the case where D is small. The underlying system (without the noise term) is taken to be stable in the sense that its Lyapunov exponent λ is negative, implying that nearby trajectories converge. When a small noise term is added to the equation of motion, the trajectories do not reach the attractor of the underlying deterministic system. The separation of two trajectories, Δx , can be characterised by its probability density $P_{\Delta x}$. (Several stochastic variables are introduced here: we use P_X to denote the probability density function for a quantity X, and $\langle X \rangle$ to denote its expectation value). It might be expected that $P_{\Delta x}$ would be well-approximated by a Gaussian distribution, and for a generic class of models this expectation is correct. An example is the case where the underlying dynamical system is $\dot{x} = \lambda x$ (with $\lambda < 0$), which approaches the attractor $x = 0$. If this equation of motion is replaced by $\dot{x} = \lambda x + \sqrt{2D}\,\eta(t)$, where $\eta(t)$ is white noise, with statistics

$$\langle \eta(t) \rangle = 0 \,, \qquad \langle \eta(t)\eta(t') \rangle = \delta(t-t') \qquad (2)$$

these equations describe an Ornstein-Uhlenbeck process [1]. The deviations from the fixed point have a Gaussian distribution in the limit as t tends to infinity:

$$P_x = \sqrt{\frac{\lambda}{2\pi D}} \exp\left[-\frac{|\lambda| x^2}{2D}\right] \,. \qquad (3)$$

provided $\lambda < 0$. The deviation Δx of two trajectories from each other is also Gaussian distributed, with double the variance. We argue, however, that there is also a generic class of models for which the distribution $P_{\Delta x}(\Delta x)$ of separations of trajectories has power-law tails:

$$P_{\Delta x} \sim |\Delta x|^{-1+\alpha} \qquad (4)$$

when Δ is large compared to $\sqrt{D/|\lambda|}$, (and we must have $\alpha > 0$ if this distribution is to be normalisable). The large excursions of $\Delta x(t)$ which are the origin of the power-law tails are a form of intermittency. The intermittency of $\Delta x(t)$ is illustrated in figure 1 for a model of colloidal particles in a turbulent flow. Figure 2 shows evidence that Δx has a power-law distribution in the same model, with an exponent which is independent of D.

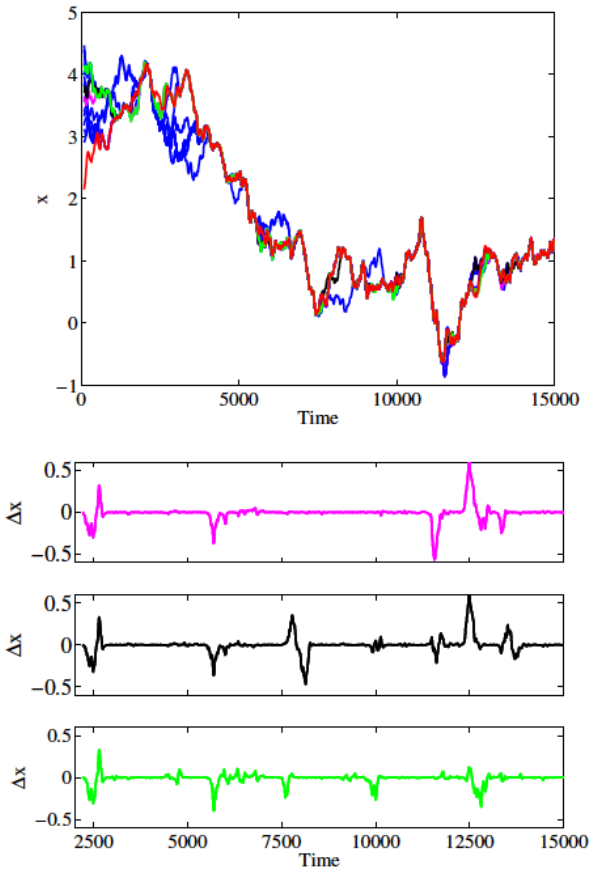

Figure 1: a) Set of trajectories of a set of colloidal particles in suspension. Different trajectories separate and recombine. **b)** Intermittent separation of pairs of trajectories $\Delta x(t)$.

The power- law distribution has both an upper and a lower cutoff scale, and the lower cutoff scale decreases as $D \to 0$.

In this talk we explain the origin of this intermittency of show how it can be quantified by making an analytical theory of the exponent α. The intermittency which is considered here is different from that which is discussed in most studies [2–5], where intermittency arises because a system is just above a threshold of instability. The systems considered in this work are driven by external noise, and we are concerned with what might be termed *sub-critical intermittency*, which is observed when the underlying system converges to an attractor. The intermittency effect discussed in this paper is only observed in non-autonomous systems, where the linearised dynamics in the vicinity of the attractor is fluctuating.

Beyond the point at which the underlying system be- comes unstable, that is, when the Lyapunov exponent λ is greater than zero. The system ceases to have a point attractor, and instead it has a strange attractor, where phase points cluster on a fractal measure [5]. We argue that as λ approaches zero from below, the exponent α in (4) approaches zero from above. When $\lambda > 0$, the two-point correlation function of the strange attractor, $g(\Delta x)$, has a power-law dependence: $g(\Delta x) \sim |\Delta x|^{D2-1}$ where D_2 is the correlation dimension of the strange attractor [6]. The analogy with (4) suggests that the exponents are related by:

$$\alpha = - D_2 \qquad (5)$$

so that normalisable distributions of fluctuations correspond to negative values of D. Equation (4) therefore gives a clear physical meaning to a negative fractal dimension.

Explanation

The talk will present an explanation of the effect, expanding upon the summary below.

Consider the linearisation of Eq. (1) to give the separation between two nearby trajectories:

$$\delta\dot{x} = Z(t)\delta x + 2\sqrt{D}\eta(t)\ , \qquad Z(t) = \frac{\partial v}{\partial x}(x(t), t). \qquad (6)$$

Note that when $D = 0$, $Z(t)$ is the logarithmic derivative of the separation $\delta x(t)$, and we can think of $Z(t)$ as being an *instantaneous Lyapunov exponent*. In the case of autonomous systems with an attractor, the attractor must be a fixed point in phase space, and $Z(t)$ approaches a constant $\lambda < 0$ as $t \to \infty$. In this case the fluctuations are described by an OU process and the distribution $P_{\Delta x}$ is Gaussian. In cases where the dynamical system is non-autonomous, $Z(t)$ need not approach a constant value. If the external driving is a stationary stochastic process, $Z(t)$ is a fluctuating quantity with stationary statistics. The origin of the power-law tails described by (4) is that the fluctuations are amplified during periods when $Z(t)>0$. This noise amplification is independent of the initial amplitude, because the fluctuating quantity Z(t) acts multiplicatively in Eq. (6). This leads to a stochastic cascade amplification process, whereby large amplitude fluctuations are built up by a succession of periods where $Z(t)>0$. The power-law tail in the fluctuation distribution arises whenever $Z(t)$ is positive for some intervals of time, however short.

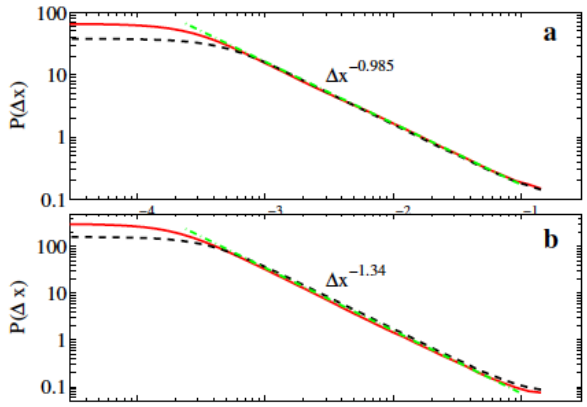

Figure 2: The probability distribution $P_{\Delta x}$ for a model system, for two values of D ($D = 3\times10^{-10}$, full curve, and $D = 10^{-9}$, dashed curves, showing fits by a power law $|\Delta x|^{-(\alpha+1)}$.

References

[1] G. E. Uhlenbeck and L. S. Ornstein, Phys. Rev., 36, 823-41, (1930).

[2] Y. Pomeau and P. Manneville, Commun. Math. Phys., 74, 189-97, (1980).

[3] E.Ott and J.C. Sommerer, Physics Letters A, 188, 39-47, (1994).

[4] S. C. Venkataramani, T. M. Antonsen Jr., E. Ott and J. C. Sommerer, Physica D, 96, 66-99, (1996).

[5] E. Ott, Chaos in Dynamical Systems, 2nd edition, University Press, Cambridbe, (2002).

[6] P. Grassberger and I. Procaccia, Physica D, 13, 34-54 (1984).

[7] M. Wilkinson, K. Gustavsson and B. Mehlig, Europhys. Lett. 89, 5002 (2010).

Multiscale Modelling of Concentrated Suspensions of Spherical Particles

Robert Powell[1], Ronald Phillips[1], Jonathan Stickel[2]

[1]*Department of Chemical Engineering and Materials Science, University of California, Davis, USA*
[2]*National Renewal Energy Laboratory, Golden, Colorado, USA*

Keywords: Microstructure, Structure Tensor, Suspension

Abstract

A continuum model of suspension behaviour has been developed which uses information obtained by microstructural modelling to predict phenomenological continuum-level parameters. Stockesian dynamics is used to model the microstructural dynamics of concentrated suspensions of spheres. The continuum model uses a second order tensor to describe the microstructure. By coupling these models it is possible to fit all of the parameters in the continuum model using steady simple shearing results. The continuum model is then shown to predict experimental results in unsteady linear shearing and in channel flow.

Introduction

The goal of this work is to develop a continuum model that can be used to solve macroscopic problems in suspension mechanics that include a description of the microstructure. We focus on suspensions of spherical particles of uniform size. In developing this model, it is crucial that not just macroscopic, averaged stresses and deformations be accurately described but also that microscopic information be modeled in order, for example, to predict particle migration. We use the model proposed by Hand (1962) to describe the suspension microstructure in terms of a second order structure tensor. A rate equation governing the dynamics of this tensor is proposed. The constitutive equation for the stress includes a Newtonian part and a part governed by the structure tensor. The structure tensor is used to describe the directionally dependent, mean-free path length. At a conceptual level, this is the distance a sphere may move in a particular direction before coming into contact with another particle. The free-path description accounts for all particles in the nearest layer of particles that confine the possible pathways in which the test sphere may move. We have found the mean-free path approach to be straightforward to use and accessible from simulation results.

The ultimate goal of this work is to extend this methodology to particles of various sizes and shapes. The use of free path description is applicable in those cases. We will present results that demonstrate that Stokesian dynamics, which models the microstructure of suspensions of monodisperse spheres in steady simple shearing flow, can be used to predict the parameters of the continuum model. These results will be used to make predictions in unsteady shearing and compared with experimental results. This can be extended to non-uniform shearing in order to predict particle migration.

Nomenclature

$\boldsymbol{F}$	Phenomenological tensor
$\boldsymbol{I}$	Identity tensor
p_s	Suspending fluid pressure (Nm^{-2})
$\boldsymbol{Y}$	Structure tensor

Greek letters

α, β	Phenomological parameters
$\dot{\gamma}$	Shear rate (1/s)
$\dot{\boldsymbol{\gamma}}$	Rate of strain tensor (1/s)
η_s	Viscosity of suspending fluid (Pas)
$\boldsymbol{\Sigma}_p$	Particle stress tensor
$\boldsymbol{\omega}$	Vorticity tensor

Subsripts

max	maximum
turb	turbulent

Model

The continuum model uses a second order structure tensor, $\boldsymbol{Y}$, to describe the suspension microstructure. It is governed by an evolution equation of the form

$$\frac{D\boldsymbol{Y}}{Dt} + \boldsymbol{\omega Y} - \boldsymbol{Y\omega} = \dot{\gamma}\boldsymbol{F}(\dot{\gamma}, \dot{\boldsymbol{Y}})$$

where $\boldsymbol{\omega}$ is the vorticity tensor and $\dot{\gamma}$ is the magnitude of the rate of strain tensor, $\dot{\boldsymbol{\gamma}}$ and $\frac{D}{Dt}$ is the material derivative. The stress tensor, T, is calculated using

$$\boldsymbol{T} = p_s\boldsymbol{I} + \eta_s\dot{\boldsymbol{\gamma}} + \dot{\eta}_s\boldsymbol{\Sigma}_p(\dot{\gamma}, \dot{\boldsymbol{Y}})$$

where p_s is the pressure, η_s is the viscosity of the suspending fluid and $\boldsymbol{\Sigma_p}$ is the particle contribution to the stress.

The unknown second order tensor functions $\boldsymbol{F}$ and $\boldsymbol{\Sigma_p}$ are represented using the following expansions (Stickel, Phillips and Powell 2006)

$$\boldsymbol{F}(\dot{\boldsymbol{\gamma}}, \boldsymbol{Y}) = \alpha_0 \boldsymbol{I} + \alpha_1 \boldsymbol{Y} + \alpha_2 \dot{\boldsymbol{\gamma}} + \alpha_3 (\boldsymbol{Y}\dot{\boldsymbol{\gamma}} + \dot{\boldsymbol{\gamma}}\boldsymbol{Y})$$

$$\boldsymbol{\Sigma_p}(\dot{\boldsymbol{\gamma}}, \boldsymbol{Y}) = \beta_0 \boldsymbol{I} + \beta_2 \dot{\boldsymbol{\gamma}} + \beta_3 (\boldsymbol{Y}\dot{\boldsymbol{\gamma}} + \dot{\boldsymbol{\gamma}}\boldsymbol{Y})$$

where the α_i and β_i are phenomenological parameters that can be determine from experiments or by microstructural simulation. These are functions of the invariants of the strain rate and structure tensors as well as, ultimately, the volume fraction and particle Peclét number.

Results and Discussion

Stickel, Powell and Phillips (2006) showed that the phenomenological parameters in the model could be determined using Stokesian dynamics. Overall, these parameters could then be used to show that the model also fit experimental data. The sole exception was the normal stress differences which did not fit over the six orders of magnitude of flow strength that was considered.
A challenging test of this model is to make calculations for either unsteady flows or non-uniform shearing. In Stickel, Phillips and Powell (2007), the transient problem was solved.

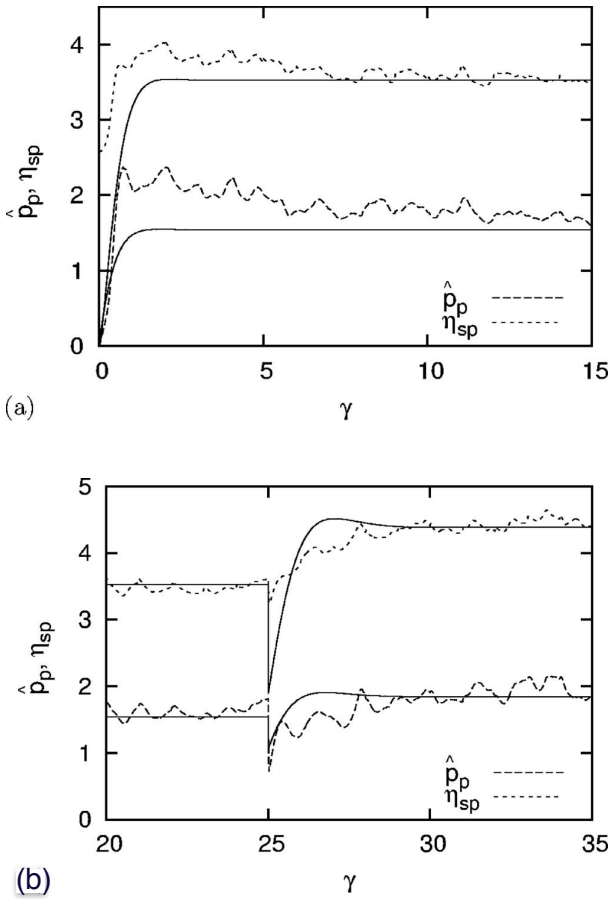

Figure 1: Examples of comparisons of the continuum model (solid lines) to simulations (dashed lines) under transient flows. The top figure shows the response to suddenly imposed shearing. The bottom figure shows the response to a step change in the shear rate.

Figure 1 shows comparisons between the continuum model and Stokesian dynamics results under transient flows. The results are presented in terms of the isotropic particle stress, p_p and the shear viscosity due to the presence of the particles, η_{sp} versus total strain, γ. The model parameters used for these simulations were obtained using steady shear data. In both cases, the continuum calculation captures the transient behaviour. The overshoot seen in the simulation in Figure 1a, which is consistent with experimental data, is not as apparent in the results using the continuum model. However, the transient response to a step change in shear rate shows good agreement between the two approaches to modelling.

Additional transient results show that the continuum model fits experimental data qualitatively over a wide range of conditions. It also provides a basis to study particle migration in non-uniform shear flow (Yapici, Powell and Phillips 2009).

Conclusions

We describe a framework for developing a multiscale model of suspensions of monodisperse spherical particles. This approach can be used to model suspensions of multi-sized spherical particles by coupling the Hand (1964) model and Stokesian dynamics simulations of multisized suspensions (Chang and Powell 1993). It is also possible to examine suspensions of particles of different shapes using the appropriate microscale models and further developing a framework for describing particle microstructure.

Acknowledgements

Supported in part by U.S. D.O.E. DE-FG07-96R14727 and in part by Grant No. ACS 36065-AC9 from the donors of the Petroleum Research Fund.

References

Hand, G. L., "A theory of anistropic fluids," J. Fluid Mech. **13**, 33–46 (1962)

Chang, C. & **R. L. Powell, R. L.**m Dynamic Simulation of Bimodal Suspensions of Hydrodynamically Interacting Spherical Particles. Journal of Fluid Mechanics 253: 1-25 (1993).

Stickel, J. J., Powell, R. L. & R. J. Phillips, R.J.. Predictions of Time Dependent Behavior of Particle Suspensions. Journal of Rheology, **51**, 1271-1302 (2006)

Stickel, J.J., Phillips, R. J. & Powell, R. L. Constitutive Modeling of Microstructure and Total Stress for Fluid Suspensions. Journal of Rheology, **50**, 379-414 (2006).

Yapici, K., R. L. Powell, R. L. & Phillips, R.J. Particle Migration and Suspension Structure in Steady and Oscillatory Plane Poiseuille Flow. Physics of Fluids, **21**, 053302 (2009).

A stochastic approach for multilayer deposition and resuspension in turbulent flows

Christophe Henry[1], Jean-Pierre Minier[2]

[1]*Institute of Fluid-Flow Machinery, Polish Academy of Science, Fiszera 14 st., Gdansk 80-231, Poland*
[2]*EDF R&D, Fluid Dynamics, Power Generation and Environment, 6 quai Watier, Chatou 78400, France*

Keywords: fouling, stochastic approach, multilayer, deposition, resuspension

Abstract

This study aims at presenting a new stochastic Lagrangian approach for the simulation of particulate fouling with a specific emphasis on the model for multilayer deposition and resuspension. For that purpose, specific models have been developed to account for the effects of particle-fluid, particle-surface and particle-particle interactions on both multilayer deposition and resuspension. With these refinements, the present approach is able to capture the formation and resuspension of complex structures on initially clean surfaces. The present work also stresses some of the current limitations in our understanding of particulate fouling and outlines areas where further experimental and numerical analyses are required.

Introduction

Colloidal fouling corresponds to the accumulation of solid colloidal particles (i.e. particles with sizes ranging from a few nanometres up to a few micrometres (Elimelech et al., 1995)) on initially clean surfaces. This continuous deposition of colloids can lead to the formation of complex multi-layered structures on the surface and even to the complete blocking of the fluid cross-section (Bacchin et al., 2011).
The present study being initially motivated by the comprehension of fouling in heat exchangers (see for instance Schwarz, 2001), the stochastic Lagrangian approach developed here includes simplified models that allow to perform tractable simulations of colloidal fouling even in complex industrial situations.

Nomenclature

g	gravitational constant (m.s^{-1})
K_{Br}	Diffusion coefficient for Brownian motion
t	Time (s)
up	Particle velocity (m.s^{-1})
us	Velocity of the fluid seend by particles (m.s^{-1})
xp	Particle position (m)

Greek letters

τ	Particle relaxation time (s)

Subscripts

p	Related to the particle

Numerical Scheme

The modelling approach for particulate fouling has been developed in a step-by-step manner considering the four elementary phenomena depicted in Figure 1: deposition, resuspension, agglomeration and clogging (Henry et al., 2012a, Henry & Minier, 2014a). Each of those phenomena is governed by the coupling between two mechanisms: particle transport (due to particle-fluid interactions) and particle attachment (due to particle-surface and particle-particle interactions).

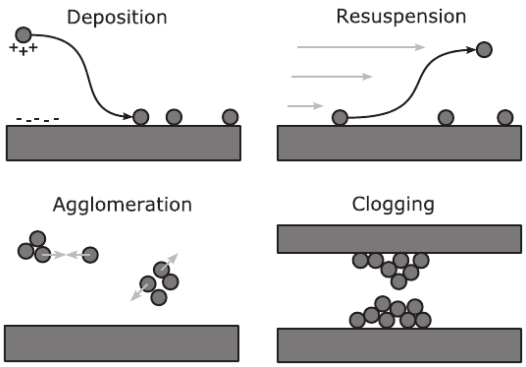

Figure 1: Sketch of the elementary phenomena of fouling. Reprinted from (Henry et al., 2012a). Copyright 2012 with permission from Elsevier.

Particle deposition. Here, particle transport is described using a Lagrangian one-point pdf approach where the particle position $\mathbf{x}_p$, its velocity $\mathbf{u}_p$ and the velocity of the fluid seen by the particle $\mathbf{u}_s$ are described by (Henry et al., 2012a):

$$d\boldsymbol{x}_p = \boldsymbol{u}_p dt$$
$$d\boldsymbol{u}_p = \frac{\boldsymbol{u}_s - \boldsymbol{u}_p}{\tau_p} dt + \boldsymbol{g} dt + K_{Br} d\boldsymbol{W}$$
$$d\boldsymbol{u}_s = \boldsymbol{A}(t, u_s) dt + B(t, u_s) d\boldsymbol{W}'$$

where τ_p is the particle relaxation time (related to

hydrodynamic drag forces), d**W** is the increment of a Wiener process, K_{Br} is the diffusion coefficient for Brownian motion and **A** and B are models for the drift and diffusion terms (respectively). Meanwhile, particle attachment to the surface is described using the DLVO theory (with refinements to account for surface roughness). The coupling between the transport step and the attachment step follows an energy-balance approach: deposition occurs only if the particle kinetic energy E_{kin} is larger than the energy barrier encountered E_{barr}.

Multilayer deposition. Similarly to the previous model for particle deposition on clean surfaces, a simple model for the formation of multilayer deposits has been developed considering that a depositing particle interacts either with a clean part of the surface or with already deposited particles (as depicted in Figure 2).

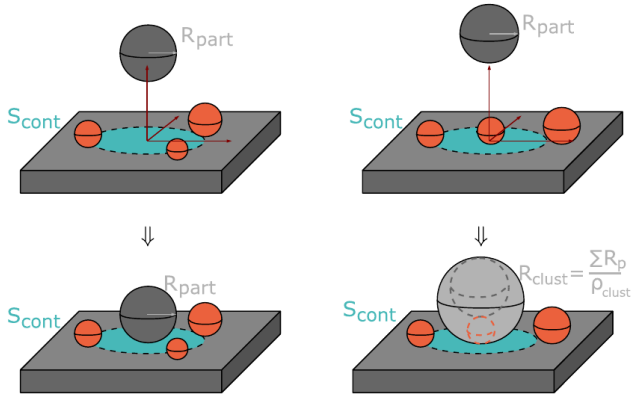

Figure 2: Drawing showing that incoming particles stick either to the clean surface (single particle deposition) or to existing particles/clusters. Reprinted from (Henry et al., 2012a). Copyright 2012 with permission from Elsevier.

The distinction between these two cases is based on geometrical considerations and on physical parameters (surface covered by already deposited particles, size of deposited particles), in a similar way to the treatment of surface roughness.
The growth of clusters on the surface is then modelled by cylinders whose height increases with further deposits.

Monolayer resuspension. Since this study is focussed on colloidal particles, only rolling motion due to hydrodynamic drag forces have been considered. The model for monolayer particle resuspension is based on a three-stage scenario (as depicted in Figure 3): particles are first set into motion when the balance between hydrodynamic forces and cohesion forces is ruptured; clusters then roll (or slide) on the rough surfaces; upon rocking on a large-scale asperity, particles

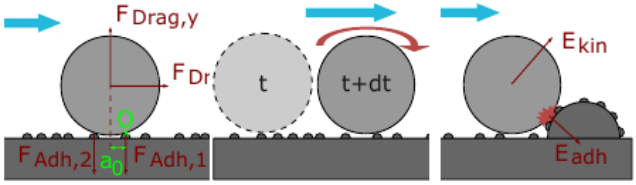

Figure 3: 2D sketch of the three-stage scenario for the monolayer resuspension model. Reprinted from (Henry et al., 2012b). Copyright 2012 with permission from American Chemical Society.

detach from the surface if their kinetic energy is higher than the adhesion potential energy.

Multilayer resuspension. The model for multilayer resuspension is an extension of the previous model for monolayer resuspension. Instead of considering particles rolling on rough surfaces, multilayer resuspension is modelled in a three-stage scenario assuming that large clusters exposed to the flow can roll on deposited particles and are resuspended upon hitting other protruding clusters (see Figure 4). To that extent, we consider the balance between hydrodynamic drag forces and intra-cluster cohesion forces only.

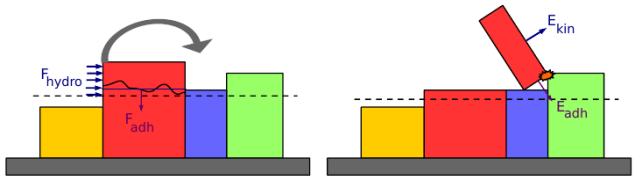

Figure 4: 2D sketch of the scenario retained for the multilayer resuspension model (three-stage scenario as in Figure 3).

Results and Discussion

Particle deposition. The present model for particle deposition has been validated with various experimental data. In particular, it has been shown that tractable simulations can be performed in complex geometries under various physical and chemical conditions (since the model accounts for both particle-fluid and particle-surface interactions).

Multilayer deposition. The model for multilayer deposition has been shown to provide qualitative agreement with available experimental data (Henry et al., 2012a) and thus properly captures the formation of either single monolayers or complex multilayered structures. Furthermore, the model is able to capture the continuous deposition of particles until complete blockage of the fluid cross-section (see Figure 5).

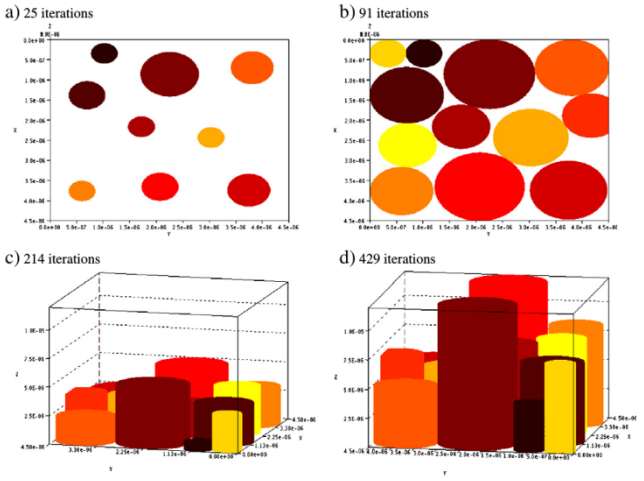

Figure 5: Clogging of a microchannel through sequential deposition of small particles (a,b,c) until the flow passage becomes blocked by a larger particle (d). Reprinted from (Henry et al., 2012a). Copyright 2012 with permission from Elsevier.

Monolayer resuspension. The model for adhesion forces and monolayer resuspension has been compared with various experimental data (Henry et al., 2012b). Figure 5 shows that the resuspension of colloidal particles from rough surfaces in turbulent flows is well-captured by the approach (Henry & Minier, 2014b).

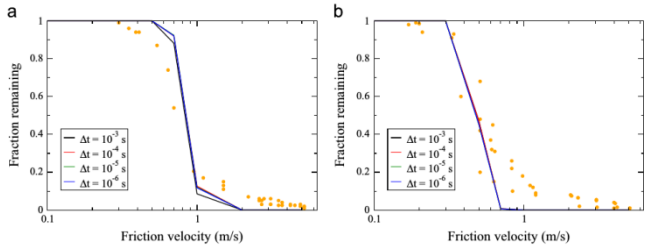

Figure 5: Fraction of particle remaining on the surface after a 1 s exposure to an airflow with varying friction velocity: numerical predictions (lines) compared to experimental data for (a) 10 µm alumina and (b) 20 µm alumina. Reprinted from (Henry & Minier., 2014b). Copyright 2014 with permission from Elsevier.

Multilayer resuspension. Due to the novelty of the multilayer resuspension model, numerical results are still being analysed. Yet, it is believed that the present model naturally captures the fact that multilayer resuspension occurs either through single particle resuspension or cluster being detached (or a combination of both) since the balance between cohesion forces and hydrodynamic forces is properly accounted for. Nevertheless, further works are still needed to extent the present model for larger particles, where burst-type resuspension is predominant (Henry & Minier, 2014a).

Conclusions

The present study thus illustrates that a single modelling approach (here in the framework of stochastic Lagrangian approaches) can be developed to model the whole fouling process provided that the coupling between particle-fluid, particle-surface and particle-particle interactions is properly accounted for. In that case, numerical results were shown to be in good agreement with experimental data. However, the current understanding of the later stages of particulate fouling is still limited and further experimental/numerical analyses are needed.

Acknowledgements

The authors would like to express special thanks to Pr. Jacek Pozorski for useful advice.

References

Bacchin, P. & Marty, A. & Duru, P. & Meireles, M. & Aimar, P. Colloidal surface interactions and membrane fouling: investigations at pore scale. Advances in Colloid and Interface Science, Vol. 164, 2-11 (2011)

Elimelech, M. & Gregory, J. & Jia, X. & Williams, R. A. Particle Deposition and Aggregation: Measurement, Modelling and Simulation. Butterworth Heinemann (1995)

Henry, C. & Minier, J.-P. & Lefèvre, G. Towards a description of particulate fouling: from single particle deposition to clogging. Advances in Colloid and Interface Science, Vol. 185-186, 34-76 (2012a)

Henry, C. & Minier, J.-P. & Lefèvre, G. Numerical study on the adhesion and reentrainment of nondeformable particles on surfaces: the role of surface roughness and electrostatic forces. Langmuir, Vol. 28, 438-452 (2012b)

Henry, C. & Minier, J.-P. Progress in particle resuspension from rough surfaces by turbulent flows. Progress in Energy and Combustion Science, Vol. 45, 1-53 (2014a)

Henry, C. & Minier, J.-P. A stochastic approach for the simulation of particle resuspension from rough substrates: Model and numerical implementation. Journal of Aerosol Science, Vol. 77, 168-192 (2014b)

Schwarz, T. Heat transfer and fouling behaviour of siemens PWR steam generators – long-term operating experience. Experimental Thermal and Fluid Science, Vol. 25, 319-327 (2001)

Orientational dynamics of a single neutrally buoyant spheroid in simple shear flow

Tomas Rosén[1,2], Jonas Einarsson[3], Arne Nordmark[1], Bernhard Mehlig[3], Fredrik Lundell[1,2]

[1]*KTH Mechanics, Royal Institute of Technology, SE-100 44 Stockholm, Sweden*
[2]*Wallenberg Wood Science Center, Royal Institute of Technology, SE-100 44 Stockholm, Sweden*
[3]*Department of Physics, Gothenburg University, SE-41296 Gothenburg, Sweden*

Keywords: non-spherical particles, dispersed particle flows, non-linear dynamics.

Abstract

We consider the orientational dynamics of a single neutrally buoyant spheroidal particle in simple shear flow. In absence of particle and fluid inertia, the particle rotates reversibly in a periodic orbit determined by its initial orientation (Jeffery, 1922). However, when inertia matters then the particle tends to rotate in a stable orbit, determined by the strength of the inertia and the particle aspect ratio. For neutrally buoyant particles the effects of fluid and particle inertia are characterized by the particle Reynolds number $Re_p=Gl^2/\nu$, where G is the shear rate, l is the length of the particle major axis and ν is the kinematic viscosity of the suspending fluid. Direct numerical simulations (DNS) by Rosén *et al*. (2014, 2015a,b,c) have shown that some bifurcations between rotational states can be analysed by considering the linear stability of the orbit descring a particle spinning around its symmetry axis that is aligned with the vorticity direction ('log-rolling'). In the present work we present a numerical method to analyse the linear stability of this state. Firstly, it is shown that the method confirms the transitions seen in the DNS for moderate Re_p. Secondly, the method accurately reproduces recent analytical results by Einarsson *et al*. (2015a,b,c) at infinitesimally small values of Re_p. This numerical tool thus allows us analyse the orientational dynamics at both small Re_p, where DNS becomes computationally expensive, and at moderate Re_p, where analytical solutions may lack validity.

Introduction

The orientational dynamics of non-spherical particles in shear flow is a question of substantial interest since it raises fundamental questions concerning the behaviour of particle suspensions in many industrial, biological and geophysical applications. For a dilute suspension where particle interactions can be neglected it is sufficient to consider the behaviour of a single particle in simple shear flow.

The orientational dynamics of a spheroid in a simple shear flow is governed by three dimensionless numbers: the particle Reynolds number $Re_p = Gl^2/\nu$ for fluid inertia (G is the shear rate, l is the length of the particle major axis and ν is the kinematic viscosity), the Stokes number $St = \alpha \cdot Re_p$ for particle inertia (α is the solid-to-fluid density ratio), and the particle aspect ratio r_p. For neutrally buoyant particles $\alpha = 1$ and therefore $Re_p = St$.

In absence of inertia, when $Re_p = St = 0$, there is an infinite family of periodic solutions in a simple shear flow, the Jeffery orbits (Jeffery 1922)

The influence of inertia on Jeffery orbits has been studied for nearly spherical particles (Saffman 1956, Subramanian and Koch 2006) and slender fibres (Subramanian and Koch 2005) for infinitesimal Re_p. It was found that the effect of fluid and particle inertia breaks the degeneracy of Jeffery's solutions and caused an orbit drift either towards 'log-rolling' (particle rotating around its symmetry axis, perpendicular to the flow-gradient plane) or 'tumbling' (particle is rotating with its symmetry axis in the flow-gradient plane).

Recently, Einarsson *et al.* (2015a,b,c) derived analytical solutions for the rotation of a neutrally buoyant spheroid in an unconfined shear flow at infinitesimal Re_p for arbitrary aspect ratios r_p. These results provide the asymptotically exact expressions for the stability exponents of the Jeffery orbits subject to inertial corrections. However, it is not known up to which values of Re_p the theory is valid.

To capture the behaviour at moderate Re_p ($Re_p > 1$) direct numerical simulations (DNS) have been used to study this flow problem (e.g. Qi and Luo 2003, Huang *et al.* 2012). Such simulations show that different stable rotational states can appear as shown in Fig. 1. Extensive numerical simulations by Rosén *et al.* (2014, 2015a,b,c) have furthermore made it possible to map out all stable rotational states varying Re_p, St and r_p. Some transitions between rotational states were shown to be captured by considering the stability of the log-rolling spheroid.

The shear flow in most DNS methods is generated in a confined domain with two parallel walls moving with same speed in opposite direction separated by distance N. This is combined with periodic boundary conditions in flow- and vorticity-directions. Because it is computationally expensive, small values of Re_p ($Re_p < 0.1$) are not normally considered. But this is required for a quantitative comparison with the analytical results of Einarsson *et al*. (2015a,b,c). An additional complication is that the analytical results were derived for an unbounded shear, whereas the simulations are for a finite system, as pointed out above.

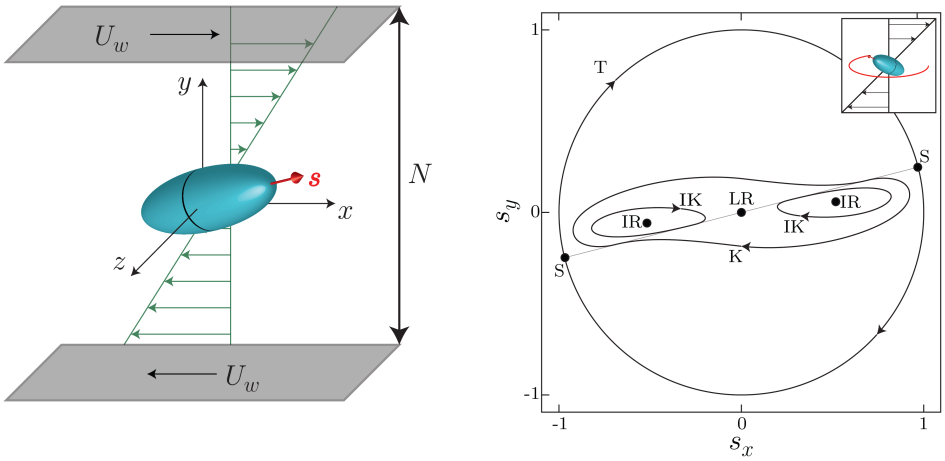

Figure 1: (top) The flow problem of a single spheroidal particle in a simple shear flow adapted from fig. 1 in Rosén *et al.* (2015c); the orientational dynamics is described by the evolution of a unit vector ***s*** along the particle symmetry axis; (bottom) stable rotational states of the spheroid; T=tumbling; LR=log-rolling; IR=inclined rolling; IK=inclined kayaking; K=kayaking; S=steady state.

In the present work, we analyse the linear stability of the log-rolling orbit numerically by discretizing the coupled particle-flow problem directly assuming that the particle starts out in the log-rolling orbit. This allows us not only to study the range of validity of the analytical results of Einarsson *et al.* (2015a,b,c), but also to predict quantitatively some of the dynamical transitions found by Rosén *et al.* (2014, 2015a,b,c).

Nomenclature

G	Shear rate (s^{-1}).
N	Distance between walls for a confined shear flow (m).
a	Length of particle symmetry semi-axis (m).
b	Particle equatorial radius (m).
l	Length of particle major axis (m); Prolate: $l=2a$; Oblate: $l=2b$.
r_p	Particle aspect ratio (-); a/b.
Re_p	Particle Reynolds number (-); Gl^2/ν.
Re_N	Channel Reynolds number (-); GN^2/ν.
St	Stokes number (-); $\alpha \cdot Re_p$.

Greek letters

ν	Kinematic viscosity (m^2s^{-1}).
ρ_f	Density of fluid (kg m^3).
ρ_p	Density of particle (kg m^3).
α	Solid-to-fluid density ratio (-); ρ_p/ρ_f.
κ	Channel confinement (-); l/N.
γ_{LR}	Real part of most unstable eigenvalue of log-rolling state.
γ_{LR}^*	The analytical constant value of γ_{LR}/Re_p as Re_p, $\kappa \to 0$ (Einarsson *et al.* 2015a,b,c).

Methods

The flow problem is set up in a cubical domain with side lengths N. This confinement is described by the dimensionless parameter $\kappa = l/N$ (see **Nomenclature** for the definition of l). The numerical linear stability analysis (N-LS) of the log-rolling state was performed using the commercial finite-element software package Comsol Multiphysics™. Instead of letting the numerical grid rotate with the particle, velocity boundary conditions are applied on the particle surface to match the log-rolling angular velocity. This angular velocity is found by numerically solving the steady-state version of the governing equations with no-slip on the particle surface. The linear stability of the log-rolling orbit is then determined through the coupled equations of motion for the fluid and the particle with only small deformations of the numerical grid. Using a fixed (although slightly deformable) grid, makes it possible to locally refine the grid resolution close to the particle surface, necessary to obtain accurate results. The N-LS method yields the most unstable eigenvalue of the log-rolling orbit, which determines the stability of the solution. At low Re_p, the most unstable eigenvalue is complex with real part γ_{LR}. This is the stability exponent calculated in Einarsson *et al.* (2015a,b,c) and quantifies the rate of orbit drift towards ($\gamma_{LR} < 0$) or away ($\gamma_{LR} > 0$) from the log-rolling state.

The eigenvalues from the N-LS method are compared both with analytical solutions (A-LS) given by Einarsson *et al.* (2015a,b,c) and with transient direct numerical simulations (DNS). The transient DNS model uses the lattice Boltzmann method with external boundary force (LB-EBF; Wu & Aidun 2010). In this method, a Lagrangian grid for the particle is immersed inside an Eulerian fluid grid. Although long term dynamical behaviour can be studied without any constraint of the particle rotation, the grid resolution close to the particle surface is not sufficient to provide quantitatively accurate results without very high computational effort.

Results and Discussion

Fig. 2 shows that the N-LS results for γ_{LR}/Re_p approaches the A-LS solution, γ_{LR}^*, as Re_p, $\kappa \to 0$. We obtain practically identical results if the domain boundaries in the flow- and vorticity-directions are taken to be periodic or velocity boundary conditions (with an undisturbed linear shear profile). We conclude that the main parameters determining the asymptotic behaviour of the log-rolling eigenvalue are the channel Reynolds number $Re_N = \kappa^{-2} \cdot Re_p$ and the degree of confinement κ.

At low channel Reynolds numbers Re_N ($Re_N < 25$) and small values of Re_p and κ, the stability exponent depends linearly upon Re_p and κ: $\gamma_{LR} \approx \gamma_{LR}^*(1 - 2.6\kappa)Re_p$.

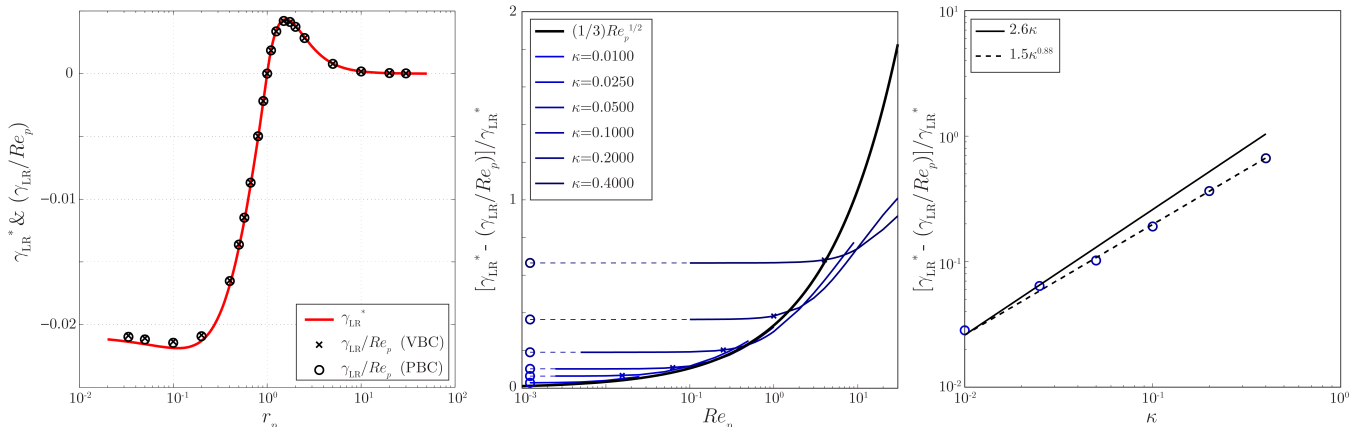

Figure 2: The real part of the most unstable eigenvalue γ_{LR} of the log-rolling state for a neutrally buoyant prolate spheroid; (left) comparison of the analytical γ_{LR}^* and numerical solutions at $Re_p = 0.00125$ and $\kappa = 0.01$ using both velocity boundary conditions (VBC) and periodic boundary conditions (PBC); (middle) results of a spheroid with aspect ratio $r_p = 4$ as function of Re_p for different channel confinement κ; the crosses mark where $Re_N = 25$;(right) results as function of κ as $Re_p \to 0$.

At high values of Re_N ($Re_N > 25$) and $Re_p < 1$ by contrast, γ_{LR} is independent of κ and follows a relationship of $\gamma_{LR} \approx \gamma_{LR}^*[Re_p - (1/3)Re_p^{3/2}]$. This scaling ceases to be valid when $Re_p > 1$ ($Re_N > 25$), and around $Re_p > 30$, other fluid modes must be considered in this dynamical system. For a prolate spheroid with aspect ratio $r_p = 4$ we find that the log-rolling state stabilizes at $Re_p \approx 27.5$, but becomes an unstable saddle at $Re_p \approx 67.5$. By comparing this with the transient DNS simulations, we find that those bifurcations are consistent with previous results by Rosén *et al.* (2014, 2015a,c).

Conclusions

The present work has considered the rotational motion of a single neutrally buoyant spheroidal particle in a simple shear flow. By numerical linear stability analysis we computed the effect of inertia upon the log-rolling orbit.. This allowed us to investigate the range of validity of the analytical results given by Einarsson *et al.* (2015a,b,c) both in terms of particle Reynolds number Re_p and channel confinement κ. We found excellent convergence in the limit of Re_p, $\kappa \to 0$ and that the corrections to the theory of Einarsson *et al.* (2015a,b,c) are of order $Re_p^{3/2}$. The model also allowed us to quantitatively predict bifurcations between the rotational states found by Rosén *et al.* (2014, 2015a,b,c).

Acknowledgements

T.R and F.L acknowledge financial support from Wallenberg Wood Science Center (WWSC). The simulations were performed on resources provided by the Swedish National Infrastructure for Computing (SNIC) at the High Performance Computing Center North (HPC2N) and the National Supercomputer Center (NSC) in Linköping, Sweden. BM acknowledges financial support from Vetenskapsrådet and the Göran Gustafsson Foundation for research in Medicine and Natural Sciences.

References

Candelier, F., Einarsson, J., Lundell, F., Mehlig, B., Angilella, J.R.The role of inertia for the rotation of a nearly spherical particle in a general linear flow. Phys. Rev. E, accepted (2015c).

Einarsson, J., Candelier, F., Lundell, F., Angilella, J.R., & Mehlig, B. Rotation of a spheroid in a simple shear at small Reynolds number. Phys. Fluids, accepted (2015a).

Einarsson, J., Candelier, F., Lundell, F., Angilella, J.R., & Mehlig, B. Effect of weak fluid inertia upon Jeffery orbits. Phys. Rev. E, Vol. 91, 041002(R) (2015b).

Jeffery, G.B. The motion of ellipsoidal particles immersed in a viscous fluid. Proc. R. Soc. Lond. A, Vol. 102, 161-179 (1922).

Rosén, T., Lundell, F. & Aidun, C.K. Effect of fluid inertia on the dynamics and scaling of neutrally buoyant particles in shear flow. J. Fluid Mech., Vol. 738, 563-590 (2014).

Rosén, T., Do-Quang, M., Aidun, C.K. & Lundell, F. The dynamical states of a prolate spheroidal particle suspended in shear flow as a consequence of particle and fluid inertia. J. Fluid Mech., Vol. 771, 115-158 (2015a).

Rosén, T., Do-Quang, M., Aidun, C.K. & Lundell, F. Effect of fluid and particle inertia on the rotation of an oblate spheroidal particle suspended in linear shear flow. Phys. Rev. E, accepted (2015b).

Rosén, T., Nordmark, A., Aidun, C.K. & Lundell, F. Evidence and consequences of a double zero eigenvalue for the rotational motion of a prolate spheroid in shear flow. Submitted (2015c).

Saffman P. G., On the motion of small spheroidal particles in a viscous liquid, J. Fluid Mech. 1, 540 (1956).

Subramanian, G. & Koch, D.L., On the motion of small spheroidal particles in a viscous liquid, J. Fluid Mech. 535, 383 (2005).

Subramanian, G. & Koch, D.L., Inertial effects on the orientation of nearly spherical particles in simple shear flow, J. Fluid Mech. 557, 257 (2006).

Wu, J. & Aidun C.K. Simulating 3D deformable particle suspensions using lattice Boltzmann method with discrete external boundary force. Int. J. Numer. Meth. Fl., Vol. 62, 765-783 (2010)

EUROMECH 566 ABSTRACTS

Clustering of chiral particles in flows with broken parity invariance

Kristian Gustafsson (University of Tor Vergata, Rome)

We study the motion of particles which break parity invariance (chiral particles). It is expected that helicoidal-like structures in the flow may affect such particles differently depending on the parity of the helicoid as well as on the chirality of the particle. In flows where one of the two parities of the helicoidal-like structures is more common, suspended chiral particles experience different levels of clustering depending on their chirality. Using analytical methods and direct numerical simulations we investigate the mechanisms of preferential sampling and clustering of chiral particles in flows with local or global breaking of parity invariance.

An accurate cut-cell method for interface-resolved simulations of particles with complex shapes

Lennart Schneiders, Matthias Meinke, Wolfgang Schröder (Institute of Aerodynamics, RWTH Aachen University, Germany)

Turbulent flows laden with complex-shaped particles are encountered in many technical and natural en- vironments such as in pulverized coal and biomass combustors or during ice-crystal formation in atmospheric clouds. The anisotropy of the particles can have a strong impact on the behavior of the fluid phase and therefore requires careful modeling of the dispersed phase. For large-scale simulations of these systems often Lagrangian particle-tracking models are used, in which the particles are traced assuming a point-mass behavior. To validate and improve these models and to enhance the understanding of the multiphase characteristics of these flows so- called interface-resolved simulations are applicable. In these simulations, the discrete solution is resolved up to the particle boundary layers such that an accurate formulation of the fluid-particle momentum exchange driving the particle motion is obtained and turbulence modulation effects are inherently captured. For particle sizes comparable to or smaller than the Kolmogorov microscale, this results in a vast increase of the computational costs that are beyond those of a regular direct numerical simulation. To this end, flexible solution schemes are required to efficiently resolve the particles along their trajectories. Numerical methods based on hierarchical Cartesian meshes provide an ideal framework by facilitating dynamic mesh adaptation near the particle surfaces and dynamic load-balancing routines.
In this contribution, an accurate finite-volume method for interface-resolved simulations of particles with complex shapes is presented. The fluid phase is discretized by a finite-volume scheme with cut-cells at the boundaries [1]. This yields a fully conservative description of the fluid-particle momentum and heat exchange which is essential to obtain accurate and stable results [1]. The particle surfaces are sharply resolved using a level-set formulation by which multiple independently moving boundaries are tracked. Complex and intersecting particle geometries are described using a multiple level-set approach [2]. During the simulation, the solution- adaptive mesh refinement strategy described in [1] is used to dynamically resolve the particle boundary layers and wakes, see Fig. 1a. This technique enables high-resolution simulations of particulate turbulent flows with particles sizes on the order of the Kolmogorov scale, see Fig. 1b.

References

[1] L. Schneiders, D. Hartmann, M. Meinke, W. Schröder, An accurate moving boundary formulation in cut-cell methods, J. Comput. Phys. 235 (2013), 786–809.
[2] C. Günther, M. Meinke, W. Schröder, A flexible level-set approach for tracking multiple interacting interfaces in embedded boundary methods, Comput. Fluids. 102 (2014), 182–202.

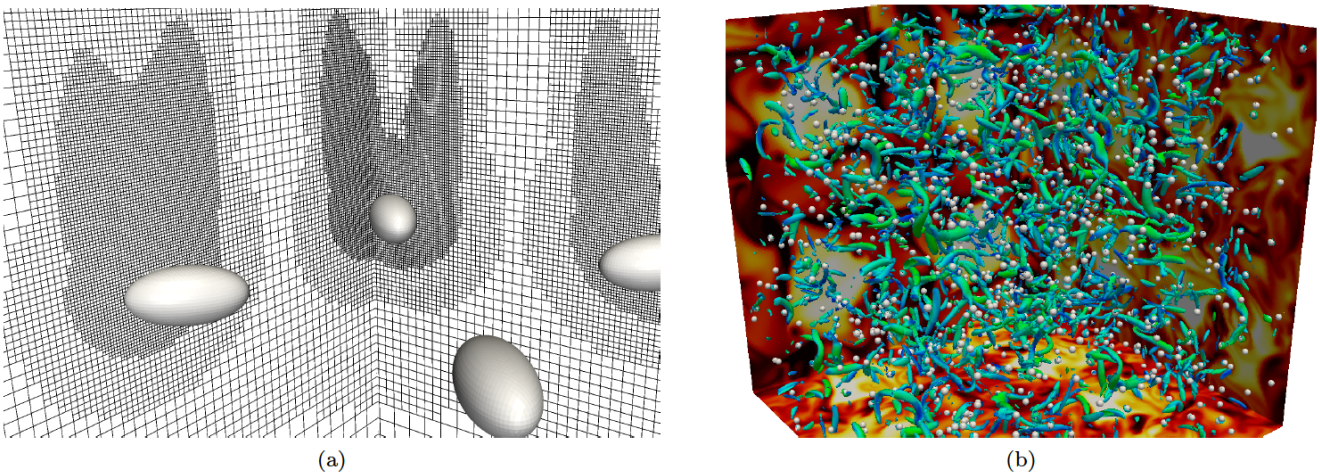

(a) (b)

Figure 1: Interface-resolved particle simulations: a) Solution-adaptive mesh for sedimenting ellipsoidal particles; b) Resolution of 1000 particles and vortical structures in a Taylor-Green vortex flow.

EUROMECH 566 ABSTRACTS

Numerical study on the stochastic features of drag and lift forces on a spheroid: contribution of self-induced vortex shedding

Jungwoo Kim (*Department of Mechanical System Design Engineering, Seoul National University of Science and Technology, Korea)*

We perform direct numerical simulations of flow around a spheroid at Re=1000 to investigate the characteristics of the drag and lift. Particular attention is paid to the stochastic contribution of the vortex shedding, which is regarded as one of the main issues to be resolved for more accurate prediction of turbulent dispersed flows (Balachandar and Eaton, 2010). To perform a three-dimensional numerical simulation of flow over a spheroid with prolate shape, we use an immersed boundary method in a cylindrical coordinate where the momentum forcing and mass source/sink are provided to satisfy the no-slip condition on the spheroid surface that does not coincide with the mesh points. For comparison, the flow over a sphere is simulated. The numerical method and boundary conditions used in this study are similar to those taken by Kim and Choi (2002).
Figure 1 shows the phase diagram of (C_d ,C_l). The stochastic contribution of the vortex shedding appears in two senses: amplitude and direction. Generally, the direction of the lift force is arbitrarily determined by the vortex shedding. As shown in figure 1, the drag has small fluctuations compared to the lift, which indicates that the stochastic model for the vortex shedding would be more important for the estimation of the lift than the drag. Also, the PDF from most cases are shown to be similar to the normal distribution with the same mean and RMS values. This result may indicate that the stochastic contribution of the vortex shedding to the drag and lift forces are Gaussian. The detailed shape of the PDF is dependent on the shape of the spheroid. On the other hand, the time correlations of the drag and lift force are different from each other, showing that the vortex shedding gives different influence on the drag and lift. For the cases considered in this study, the temporal correlation of the lift is more closely associated to the vortex shedding than that of the drag.

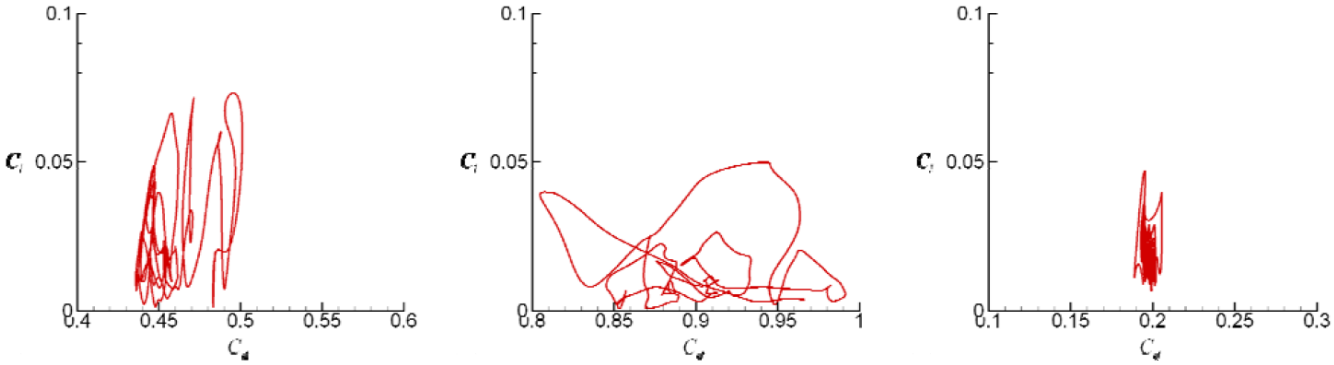

Figure 1: Phase diagram of drag and lift forces (C_d , C_l): (a) e=1, s=0; (b) e=0.2, s=0; (c) e=1.5, s=0.

Influence of thermal stratification on plankton surfacing in turbulent open channel flow

Salvatore Lovecchio* and Alfredo Soldati (Dipartimento di Ingegneria Elettrica, Gestionale e Meccanica, Università di Udine & Dipartimento di Fluidodinamica, CISM, Udine,Italy)
* currently at Institut de Mécanique des Fluides, Université de Toulouse, INPT–UPS–CNRS, F-31400 Toulouse, France

Keywords: thermal stratification, phytoplankton

Abstract
Thermal stratification induced by solar heating at the surface of turbulent flow influences the transfer fluxes of heat, momentum and chemical species at the ocean-atmosphere interface. In this paper we focus on the dynamics of gyrotactic self-propelled cells, which model the behaviour of phytoplankton, in turbulent stratified open channel flow. To activate the process of photosynthesis these microswimmers need to stay in the upper layer of the flow to receive the light. We will discuss how modulation of turbulent fluctuations due to thermal stratification can affect their dynamics in stratified turbulent open channel flow.

Introduction
In recent years a whole class of biological and physical systems which may be referred to as ac- tive particles, has been studied theoretically and experimentally. Examples of such systems are the self-propelled particles as phytoplankton cells, whose interaction with the leading fluid is non trivial. A wide variety of external factors including nutrient concentration, gravity, and the rate of strain of the fluid affect the orientation of the swimming velocity of the cells [1, 2]. The resulting

distribution is far from uniform. Gradients in concentration of plankton span a wide range of length scales, ranging from thousands of kilometres to microscale patchiness that occurs at the scale of centimetres. To deal with aquatic flows, motile micro-organisms have developed many ways of adaptation [1]. One of those tends to orient the cell swimming direction upward against gravity. The resulting balance between gravitational torque due to the asymmetric distribution of density and the hydrodynamic torque is known as gyrotaxis [6] and will be examined in this paper.
Recent experimental observation shows that gyrotactic algae cells could be trapped in horizontal layers in laminar vertical shear. The phenomenon called 'gyrotactic trapping' [1, 2] occurs when vertically migrating cells accumulate where vertical gradients in horizontal velocity exceeds a critical shear threshold, causing cells to tumble end over end. Only recently it was demonstrated that phytoplankton clustering could occur also in turbulence [3, 7]. Shear, in the form of vertical gradients in horizontal fluid velocity, can be generated by tidal currents, wind stress, and internal waves and is often enhanced within thin layers. Moreover it is interesting to investigate how modulation of turbulent fluctuations controlled by stratification, could affect the dynamics of phytoplankton cells.

Numerical Scheme
We perform Direct Numerical Simulation of stably stratified turbulence coupled with Lagrangian parti- cle tracking. The reference geometry consists of two horizontal (infinite) flat parallel walls; the x-, y- and z- axis of the coordinate system point in the stream- wise, spanwise and wall-normal directions. A stable stratification is obtained by imposing a constant heat flux at the surface and an adiabatic condition at the wall. For the fluid velocity, no-slip (resp. no-stress) boundary conditions are enforced at the bottom (resp. top) boundary. The dimensionless Reynolds, Grashof and Prandtl number are defined as:

$$Re_\tau = \frac{u_\tau h}{\nu}, \qquad Gr = \frac{g\beta h^3}{\nu^2}\frac{\partial\theta}{\partial z}\Big|_s, \qquad Pr = \frac{\mu c_p}{\lambda}. \tag{1}$$

where μ and ν are the dynamic and the kinematic viscosity, β is the thermal expansion coefficient, c_p is the specific heat and λ is the thermal conductivity. In the definition of Re_τ and Gr, $u_\tau=(h|\boldsymbol{\delta}_p|/\rho)^{1/2}$ is the shear velocity (ρ being the fluid density) whereas $\partial\theta/\partial z|_s$ is the imposed free-surface heating. All the simulations are run at reference Prandtl number $Pr = 5$, Reynolds number $Re_\tau=171$ and at three different values of the shear Richardson number $Ri_\tau=Gr/Re_\tau^2$, which measures the importance of buoyancy compared to inertia: $Ri_\tau=0$, $Ri_\tau=165$ and $Ri_\tau=500$. Further details on the numerical method can be found in Refs [4]. The dynamics of a population of $N = 10^5$ swimming micro-organisms is simulated. Each micro-swimmmer is modelled as a spheroidal particle whose position x evolves according to:

$$\frac{d\mathbf{x}}{dt} = \mathbf{u}(\mathbf{X}) + v_s\mathbf{p}, \tag{2}$$

where v_s is the mean cell swimming speed, **u** the velocity of fluid in the position of swimmer and **p** the particle orientation. The orientation **p** of each swimmer evolves in response to the biasing torques acting upon it. Under the assumptions that the microswimmers cells have a spheroidal geometry, the reorientation rate of the organisms is defined by the following balance of forces:

$$\frac{d\mathbf{p}}{dt} = \frac{1}{2B}\left[\mathbf{k} - (\mathbf{k}\cdot\mathbf{p})\mathbf{p}\right] + \frac{1}{2}\omega\wedge\mathbf{p} \tag{3}$$

where **k** = [0,0,1] is a unit vector in the vertical upwards direction, $\omega = \nabla\wedge\boldsymbol{u}$ is the fluid vorticity and $B = \mu\alpha_\perp/(2h\rho g)$ is the gyrotactic reorientation time (h denotes the centre-of-mass offset relative to the centre-of-buoyancy, $\alpha_\perp$ is the dimensionless resistance coefficient for rotation about an axis perpendicular to **p**, ρ and μ are the fluid density and viscosity, respectively). B is a key parameter for the dynamic of the cells since it represents the characteristic time a perturbed cell takes to return to vertical if $\omega = 0$. The first term on the right hand side of equation (3) describes the tendency of a cell to remain aligned along the vertical direction due to bottom-heaviness while the second term captures the tendency of vorticity to overturn a cell by imposing a viscous torque on it. Cell positions and swimming direction were integrated using the non-dimensional form of equations (2) and (3):

$$\frac{d\mathbf{x}^*}{dt^*} = \mathbf{u}^*(\mathbf{X}^*) + \Phi\mathbf{p}, \tag{4}$$

$$\frac{d\mathbf{p}}{dt^*} = \Psi\left[\mathbf{k} - (\mathbf{k}\cdot\mathbf{p})\mathbf{p}\right] + \frac{1}{2}\omega^*\wedge\mathbf{p} \tag{5}$$

where time, lenghts and velocity were non-dimensionalized by using the friction velocity u_τ and fluid viscosity ν. Dimensionless parameters are $\Phi = v_s/u_\tau$ and $\Psi = \frac{1}{2B}\frac{\nu}{u_\tau^2}$. At each time step of the simulation, the local fluid velocity and vorticity at the particle positions, were calculated using lagrangian interpolation.
The reorientation timescale, while known only for handful species, generally spans the range $B \simeq 0.1 - 10$ s and phytoplankton swimming velocities are often in the range $V_s \simeq 10 - 1000$ μm/s. In the present simulations a fixed value of the swimming velocity equals to 100 μm/s is used (the corresponding dimensionless value is $\Phi = 0.048$) which is a parameter based on Chlamydomonas augustae [3, 7]. While this species has a value of the gyrotactic time scale equals to 3.4 s, simulations were performed by investigating the range $B \simeq 0.1 - 10$ s in particular $B = 0.1, 1, 10$ s which correspond to $\Psi_H = 1.13$, $\Psi_I = 0.113$, $\Psi_L = 0.0113$.

Results and discussion
Thermal stratification induces at the surface an increase of the mean streamwise velocity [4] which, in turn, causes an

increase in the mean strain rate. This happens in the region of thermocline where rapid variation of temperature profile arises and in which internal gravity waves could form. It is interesting to investigate if the increase of the mean strain rate close to surface can influence the vertical migration of phytoplankton cells.
Results are shown in figure 1(a) in which the profile of concentration for the case of Ψ_1 is presented for the different values of stratification (the case of neutrally buoyant flow is reported here as reference). The concentrations are shown against the wall distance: the regions closed to the surface ($z^+ = 0$) are depleted at higher values of stratification. Particles will be driven away from vertical upward. This will deeply affect the dynamics of the cells with lower values of Ψ (not shown).
In figure 1(b) the trends of p_z for Ψ_1 and for the different values of shear Richardson number are shown. There is a significant difference with respect to the neutrally buoyant case: For Ψ_1 and $Ri_\tau = 500$ swimmers lose their ability to be perfectly aligned with the vertical direction just under the maximum value of strain rate. On the other hand the small amount of particles that are able to overpass this maximum value tend to orient again with the vertical direction.

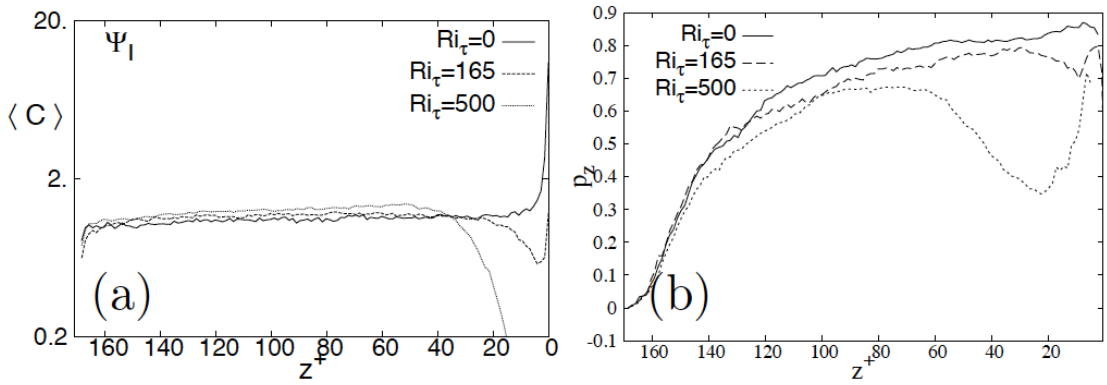

Figure 1: Concentration in log-linear scale (a) and mean vertical orientation (b) for Ψ_1. $Ri_\tau = 0$ is shown in solid curve, $Ri_\tau = 165$ is shown in dashed lines, and $Ri_\tau = 500$ in dots.

Conclusions

The dynamic of self-propelled particles in turbulent open channel flow was introduced. Preliminary results linked to the dynamics of active particles and their interaction with the stratification demonstrated that the presence of stratification is able to significantly modify the surfacing of phytoplankton. Further analysis will be done to deeply understand the formation of gyrotactic trapping in correspondence of thermal stratification. Future developments could incorporate the strict physical interaction between surface waves (which effect in this study was neglected) and active particles.

Acknowledgements

We acknowledge CINECA supercomputing center (Bologna, Italy), ISCRA Computing Initiative for generous allowance of computer resources, and COST Action FP1005.

References

[1] Durham W. M., Stocker R., 2012. Annual review of marine science 4.
[2] Durham W. M., Kessler J. O., Stocker R., 2009. Science 323.
[3] Durham W. M., Climent E., Barry M., De Lillo F., Boffetta G., Cencini M., Stocker R., 2013. Nature communications 4.
[4] Lovecchio S., Zonta F., Soldati A., 2014. Advances in Water Resources 72.
[5] Pedley TJ., Kessler JO., 1992. Annual Review of Fluid Mechanics 24.
[6] Pedley TJ., Kessler JO., 1990. Journal of Fluid Mechanics 212.
[7] Zhan C., Sardina G., Lushi E., Brandt L., 2014. Journal of Fluid Mechanics 739.

Breakage of ductile aggregates in turbulent channel flow

Cristian Marchioli and Alfredo Soldati (University of Udine, Udine, Italy)

In this paper we study breakage rate statistics of small colloidal aggregates in non-homogeneous anisotropic turbulence. To this aim, we use pseudo-spectral direct numerical simulation of turbulent channel flow and Lagrangian tracking to follow the motion of the aggregates, modelled as sub- Kolmogorov massless particles. We focus specifically on the effects produced on a given type of aggregate by ductile rupture: This rupture is initially activated when the fluctuating hydrodynamic stress generated by the surrounding fluid exceeds a critical value, $\sigma > \sigma_{cr}$, and is brought to completion when the energy absorbed by the aggregate meets the critical breakage value. We demonstrate that ductile rupture is associated to significant reductions of the breakage rate with respect to the case of instantaneous brittle rupture, which produces breakage as soon as the condition $\sigma > \sigma_{cr}$ is met. The mechanism of ductile breakage thus acts as a low-pass filter for stress-induced events that occur at time scales shorter than the characteristic time with which the aggregate responds to deformation. The reduction in the

breakage rates is evident especially for weak aggregates characterized by small critical stress value and no universal scaling can be observed. For strong aggregates characterized by large critical stress value the breakage rate is less affected by the specific mechanism leading to rupture because such aggregates can only be disrupted by extremely intense stresses and thus store the amount of deformation energy required to break almost impulsively. The observed discrepancies are linked to the different energy values at play as well as to the statisti- cal features of energy distribution in the anisotropic turbulence case examined.

References

[1] Marchioli,C.,Soldati,A.,"Turbulent breakage of ductile aggregates" *Phys. Rev. E*, 91, 003000 (2015).

[2] Babler, M.U., Biferale, L., Brandt, L., Feudel, U., Guseva, K., Lanotte, A.S., Marchioli C., Picano F., Sardina G., Soldati A. and Toschi, F., "Numerical simulations of aggregate breakup in bounded and unbounded turbulent flows" *J. Fluid Mech.*, 766, 104-128 (2015).

Notes _____

Notes _____

Notes _____

Notes _____